FACULTY OF SCIENCE AND TECHNOLOGY

MASTER'S THESIS

Study programme / specialization:	The *spring* semester, *2024*
MSc. Biological Chemistry, Specialization in Molecular Biology	Open

Author:

Camilla Halvorsen

Supervisor at UiS:

Associate Professor, Hanne Røland Hagland

Thesis title:

Effects of Short Chain Fatty Acids Butyrate and Propionate on Colorectal Cancer Cell Lines in Combination with 5-FU Treatment and Glucose Starvation

Credits (ECTS): 60 ECTs

Keywords:	Pages: 108
Colorectal Cancer, Cancer Metabolism, Gut Microbiota, Short Chain Fatty Acids, Butyrate, Propionate, 5-fluorouracil, 2D Cell Culture, 3D Cell Culture, Chemotherapy, Chemotherapy Pretreatment	+ appendix: 68 Stavanger, *06.2024*

“What we do see depends mainly on what we look for. ... In the same field the farmer will notice the crop, the geologists the fossils, botanists the flowers, artists the colouring, sportmen the cover for the game.

Though we may all look at the same things, it does not all follow that we should see them.”

- John Lubbock, The Beauties of Nature and the Wonders of the World We Live in

Abstract

Colorectal cancer (CRC) is an increasing global health concern, ranking as the third most common cancer worldwide and the second leading cause of cancer related mortality. One of the main risk factors for the development of this disease is gut microbiome dysbiosis. Butyrate (BA) and propionate (PA) are two short chain fatty acids (SCFAs) produced by gut microbiota as a product of bacterial fermentation of dietary fibers. BA and PA have demonstrated promising anti-carcinogenic effects, including inhibition of cell proliferation, induction of apoptosis, and modulation of gene expression in CRC cells. Glucose, a primary energy source for cells, plays an important role in cancer cell metabolism and survival, and altered glucose metabolism is considered as being one of the many hallmarks of cancer. This study aimed to explore the effects of BA and PA, both singularly and combinatorically, as well as a pretreatment to the common chemotherapeutic agent 5-fluorouracil (5-FU), on the three CRC cell lines HCT116, SW948, and Caco-2, under different glucose conditions to stimulate metabolic stress.

Singular treatments decreased cell viability in a dose dependent manner across all cell lines, consistent with their known mechanisms. Under glucose starvation, however, the CRC cells showed increased viability, suggesting utilization of BA and PA as alternative energy sources. The metabolic profiling revealed a biphasic response, where lower BA and PA concentrations enhanced mitochondrial function, while higher concentrations induced mitochondrial stress. Combinatorial treatments of BA and PA showed synergistic effects in cell growth inhibition, especially at lower PA concentrations. Higher PA concentrations reduced the sensitivity to BA. Under glucose starved conditions, the combination treatments increased cytotoxicity compared to the standard physiological concentration of glucose.
Pretreatment of BA and PA to 5-FU gave variable results across different concentrations and cell lines, indicating the need for further investigation.

Overall, BA and PA demonstrated interesting potential as therapeutic agents in CRC treatment, warranting further research to optimize protocols and using 3D culture models to more accurately simulate the tumor microenvironment. Exploring the regulation of BA and PA as supplements and/or pre/probiotics could provide insights into implementing their use in clinical settings to improve therapeutic outcomes.

Acknowledgements

I would like to express my gratitude towards my supervisor, Professor Hanne Røland Hagland, for her exceptional expertise, her pedagogical approach to teaching, and for being a genuinely down to earth person. Her guidance and support have been invaluable throughout the journey of both my bachelor´s and master's studies. I also extend my heartfelt thank you to Professors Federico and Mark for their contributions and encouragement. Their dedication to their fields has been truly inspiring. A special thank you goes to my fellow students Emily, Nicolay, and Kristine, for their support during the challenging times of higher academia. Their companionship has made the lab environment less stressful and provided much needed social breaks during an otherwise hectic period. I am particularly grateful to Julie for being my go-to person in the lab and for offering me the opportunity to participate in tutoring. I would also like to acknowledge Marcus, Marina, and Martin for being inspirational academics and for their timely assistance whenever I needed it.

I want to thank my son, Sebastian, for being a living proof of my dedication, and my pride and glory. When I first became a mom, I never imagined reaching where I am today, but the person he is becoming and the degree I am so close to obtaining are things I will forever be proud of. To my partner, Phillip, thank you for being my cheerleader and for making me feel like the smartest person alive. I also want to acknowledge my best friend Tea whom I met the very first day of my bachelor´s. Thank you for always having a listening ear and being a safe place to let out my every frustration. Thank you to my parents for always supporting my aspirations and helping me out whenever I needed it. I genuinely could not have finished this chapter without you. Lastly, I want to acknowledge myself for pushing through the obstacles and continuing to aim toward my goals. Juggling the roles of being a mom, a full-time master´s student, and having two jobs has not been easy, but moments like this make it all worthwhile.

Table of Contents

List of Figures

List of Tables

List of Equations

List of Abbreviations

5-FU	5-fluorouracil
ATP	Adenosine triphosphate
BA	Butyric Acid
BCA	Bicinchoninic Acid
BSA	Bovine Serum Albumin
BSL-2	Biosafety level-2
CCK-8	Cell Counting Kit-8
CRC	Colorectal cancer
DMEM	Dulbecco's Modified Eagle's Medium
ETC	Electron transport chain
FCCP	carbonyl cyanide-4 (trifluoromethoxy) phenylhydrazone
FDA	Food and Drug Administration
GDH	Glutamate dehydrogenase
GLS1	Glutaminase 1
GLUT	Glucose Transporter
HAT	Histone Acetylace

HDAC	Histone Deacetylase
IARC	International Agency for Research on Cancer
MCTs	monocarboxylate transporters
MPC	Mitochondrial pyruvate carrier
MPC	Mitochondrial Pyruvate Carrier
NADPH	Nicotinamide adenine dinucleotide phosphate
OXPHOS	Oxidative phosphorylation
PA	Propionic Acid
PEP	Phosphoenolpyruvate
PI	Propidium Iodide
PKM2	Pyruvate Kinase M2
PPE	Personal Protective Equipment
PPP	Pentose Phosphate Pathway
ROS	Reactive oxygen species
SCFA	Short-chain fatty acid
SMCTs	Sodium-coupled monocarboxylate transporters
TCA cycle	Tricarboxylic acid cycle
WR	Working reagent
AA	Antimycin A
αKG	α-ketoglutarate

1. Literature Review

1.1 Colorectal Cancer Overview

1.1.1 Cancer

Cancer is a broad term for a disease that results when cellular changes cause uncontrolled growth of cells that may lead to visible growth of tumors (1). The global landscape of cancer in 2022 underscores the impact of this disease, as highlighted by the International Agency for Research on Cancer (IARC) - the cancer agency of the World Health Organization (2). Their latest estimates show an estimation of 20 million new cancer cases and 9.7 million deaths worldwide in recent years. The global impact of cancer emphasizes the need for continued research and better understanding of specific cancers, such as colorectal cancer, to improve diagnosis, prevention, and treatment.

1.1.2 Colorectal Cancer

Colorectal cancer (CRC) is a widespread global health concern, ranking as the third most common cancer worldwide and the second leading cause of cancer related mortality. More than 1.9 million new cases of CRC, where approximately half resulted in death, were estimated to have occurred globally in 2020 (3). Although historically more common in western nations, CRC is exhibiting changing trends in correlation to rapid economic development in certain Eastern European countries (4). The prevalence of CRC highlights its substantial impact on global health. This disease not only affects millions of individuals worldwide, but also poses significant challenges in terms of diagnosis and treatment. Efforts to address CRC must therefore be prioritized to reduce the burden of this disease and improve outcomes for affected individuals.

CRC develops slowly and following symptoms may not occur until the size have reached several centimeters (5). CRC originates as benign, localized growths of abnormal cells within the colonic mucosa, called polyps, that protrude into the intestinal lumen (6). Very few polyps become malignant, and this progression can take years or even decades (**figure 1.1**) (7). Most malignant polyps develop from adenomas. Up to 40% of all people over 60 years of age develop adenomatous polyps, where the size of the adenoma increases the risk of cancer development (8). As the cells proliferate, dysplasia caused by damage to cellular DNA may occur, leading to a high risk of invasive carcinoma (9).

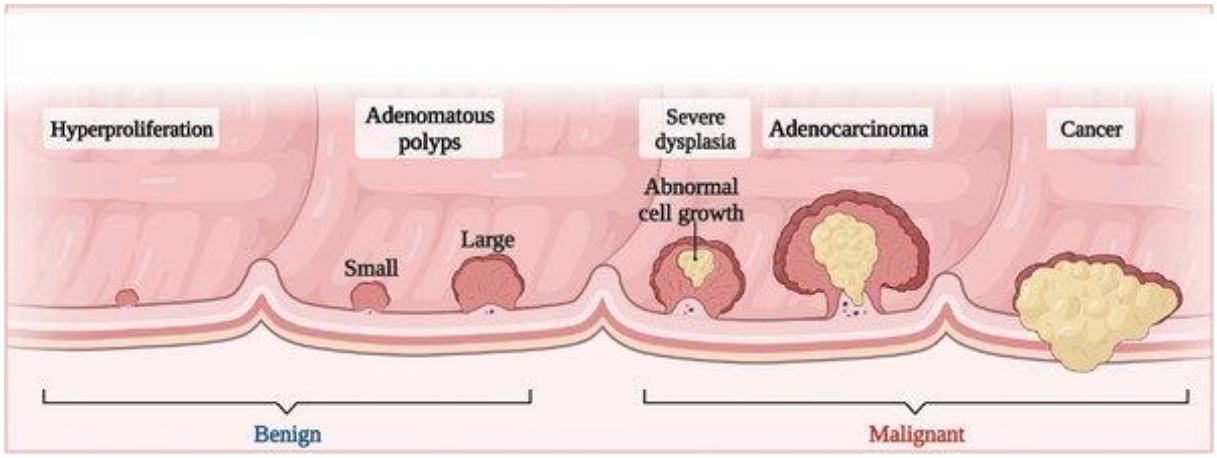

Figure 1.1 The process of CRC development

CRC starts as benign polyps within the colonic mucosa. Malignant polyps develop from adenomas, with a high risk of dysplasia and invasive carcinoma (10).

The conventional therapies for CRC are surgery, chemotherapy, and radiotherapy (11), and the therapeutic strategy for the individual in question depends on the staging of the cancer. Where surgery is more applicable in the earlier stages of CRC, later stages, with the addition of metastasis, require more comprehensive treatments (12).

Age represents the highest risk factor for CRC, with individuals over fifty years old facing significantly heightened susceptibility (13). Other inherent risk factors include a personal- or family history of CRC, lifestyle factors such as physical activity, smoking, alcohol intake, and diet (3). Unhealthy nutritional choices could increase the likelihood of developing CRC by as much as 70% (14). Malnutrition has been linked to accelerated CRC progression and poor prognosis (15). Nutrition, environmental factors, and lifestyle can influence the gut microbiota. The role of the gut microbiome in CRC development and treatment is an emerging area of interest.

1.2 Gut Microbiome and Its Role in Colorectal Cancer

1.2.1 Gut Microbiome Overview

The gut microbiome plays an important role in maintaining overall health and influencing physiological processes. The microbial population in the gut consists of more than 100 trillion bacteria, distributed into 2000 microbial species, that interacts symbiotically with the host through metabolism, host protection, and facilitating communication through the gut-brain axis (16–18). It is estimated that the colon is the most heavily populated section of the gut, containing approximately 70% of the total microbiome (19). Given the important role of the gut microbiome in maintaining host health, alterations in its composition can have a large impact on various diseases, including CRC.

1.2.2 Gut Microbiome and Colorectal Cancer

In the context of CRC, the gut microbiome has a profound impact on the carcinogenic development as a consequence of dysbiosis (18,20). Not only does it play a role in the development and progression of CRC, but it has also been linked to the efficacy of the response to cancer treatments, especially chemo- and immunotherapy (21).

As mentioned earlier, diet plays an important role in CRC progression. The diet an individual follows directly impacts the diversity of the microbiome, and certain bacterial species have been found to be either increased or decreased in association with CRC (20). A diet rich in red meat and high fat have been shown to increase CRC diagnosis (22). On the other hand, a fiber rich diet was found to reduce CRC development (23). In addition, microbial metabolites have recently emerged as an important factor for the connection between the gut microbiome and CRC (24).

1.2.3 Short Chain Fatty Acids

Short-chain fatty acids (SCFAs) represent a crucial link between gut microbiota and host health, influencing gut and immune homeostasis. SCFAs are bacterial metabolites produced primarily through the fermentation of dietary fiber and resistant starches by specific colonic anaerobic bacteria (25). The most commonly produced SCFAs in the gut are acetate, propionate (PA), and butyrate (BA). Acetate is the most abundant SCFA, however BA and PA are arguably the most important. The concentration of SCFAs fluctuates throughout life and is heavily influenced by the composition of the gut microbiome and dietary habits. The primary bacteria responsible for the production of BA belong to the Firmicutes phylum, particularly within the *Lachnospiraceae* and *Ruminococcaceae* families. PA producing bacteria mostly belong to the Bacteroidetes phylum, the Negativicutes class, and the *Lachnospiraceae* family (26). The fibers that are best for the production of SCFAs are inulin, fructooligosaccharides, resistant starch, pectin, arabinoxylan, and guar gum (27).
Among the broad spectrum of functions of these SCFAs, their potential as energy sources for colonocytes, their support in the gut barrier integrity, and their role in gene regulation and immune functions makes these metabolites important players in the gut (**figure 1.2**) (28).

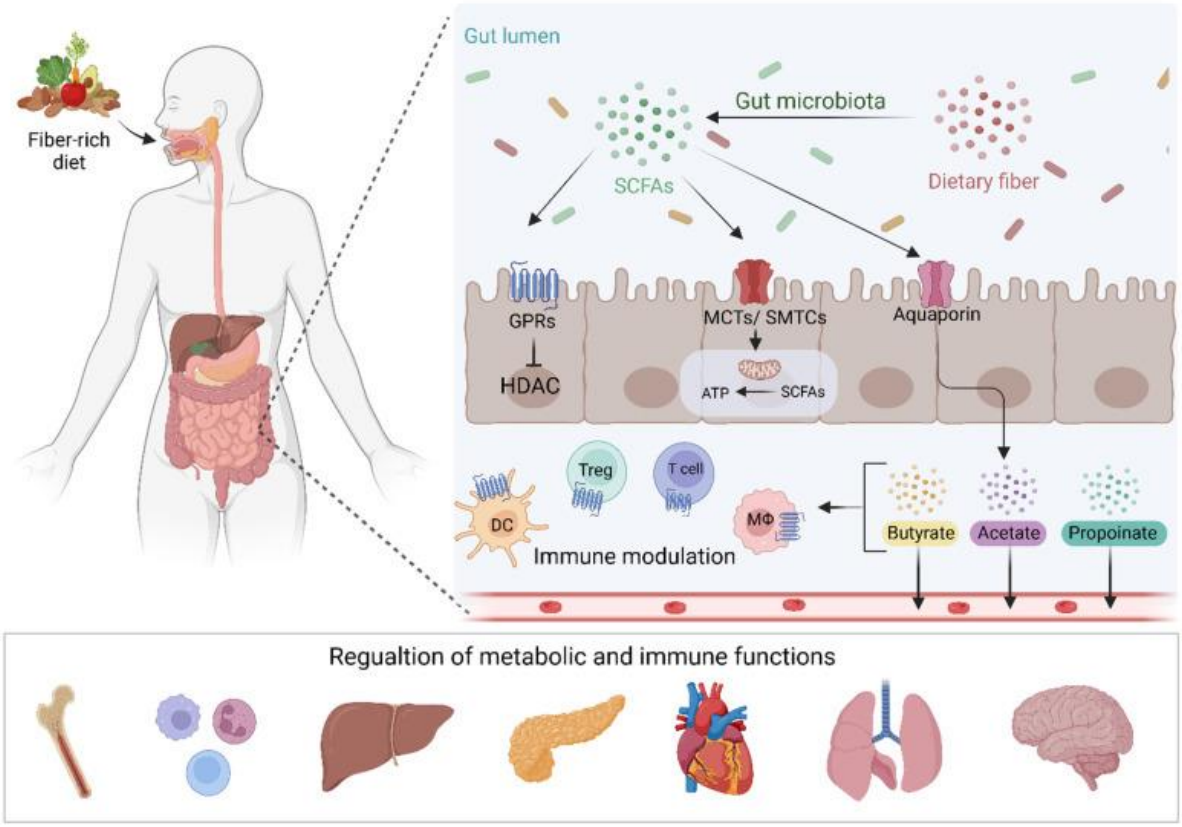

Figure 1.2 Production of SCFAs happen through the fermentation of dietary fibers.

SCFAs can be used in gene regulation, energy production, and immune functions through the interactions with G-protein coupled receptors (GPCRs), monocarboxylate transporters (MCTs) and sodium-coupled monocarboxylate transporter (SMCTs). DC; dendritic cell, Treg; T regulatory cell, Mϕ; macrophage (28)

1.2.4 Fatty Acid Oxidation

Fatty acids can be oxidized in order to provide the cell with energy. First, they are transported through the cell via fatty acid transporters such as monocarboxylate transporters (MCTs) and sodium-coupled monocarboxylate transporter (SMCTs).

Once inside the cell, fatty acids are converted to acyl-CoA. CoA is replaced by carnitine to allow for the transportation from the cytosol across the inner mitochondrial membrane. Acyl carnitine is converted back to acyl-CoA before entering the beta-oxidation pathway (**figure 1.3**) (29).

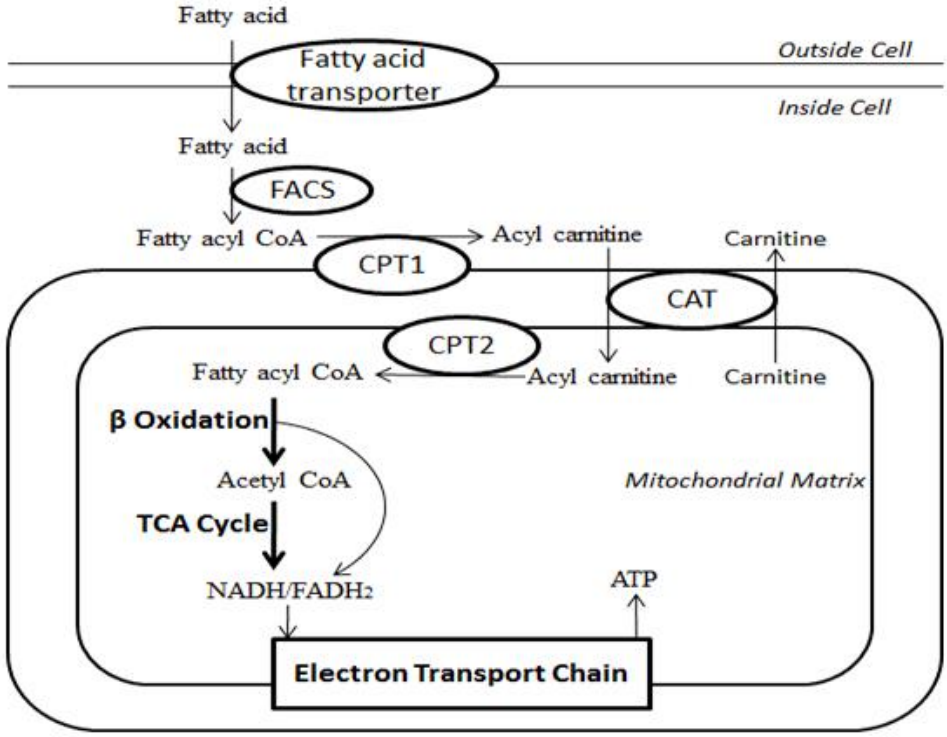

Figure 1.3 Schematic of fatty acid oxidation.

Fatty acids are transported into the cell via fatty acid transporters, converted to acyl-CoA and transported through the mitochondrial membrane where it undergoes beta oxidation to produce acetyl CoA, which can actively participate in the TCA cycle (30). FACS; fatty acid-CoA synthase, CPT1; Carnitine palmitoyl transferase 1, CAT; Carnitine-acylcarnitine translocase, CPT2: Carnitine palmitoyl transferase 2.

Beta oxidation involves the production of acetyl-CoA, $FADH_2$ and NADH which can participate in the TCA cycle and ETC to produce ATP. Most fatty acids have an even number

of carbons. Fatty acids of odd carbon numbers go through fatty acid oxidation in a different manner. Butyrate, or butyric acid (BA) is a four-carbon SCFA, and metabolized through beta oxidation. Propionate, or propionic acid (PA) is a three-carbon SCFA. PA can be metabolized through the propionic acid pathway, first to propionyl-CoA, then methylmalonyl-CoA, and lastly succinyl-CoA. Succinyl-CoA, a part of the TCA cycle, can be utilized to produce ATP or glucose by gluconeogenesis (31,32).

1.2.5 Effects of Butyrate and Propionate on Cancer Cells

BA and PA have context dependent effects. In colonocytes, these SCFAs supply energy. In contrast, both of these metabolites have shown to act destructive towards cancer cells. Current research indicates that BA and PA can suppress cancer cell proliferation, migration, and invasion in CRC (33).

Hu et al. found BA to inhibit pro-proliferative miR-92a in CRC, a micro RNA significant in the gene regulation of various cellular processes that takes part in proliferation, apoptosis, differentiation, and growth (34). This led to an increase in p57 levels, which in turn inhibited CRC proliferation and induced apoptosis.

BA can also act as a histone deacetylase (HDAC) inhibitor. HDAC is an enzyme that restores a relaxed chromatin into a closed and compact form by catalyzing the removal of acetyl functional groups from the lysine residues on the histone (35). If inhibited, uncontrolled gene expression might occur. It is also found that the inhibition of HDAC by BA hyperactivates the Wnt signaling, which leads to induced apoptosis in CRC (36).

Furthermore, BA activates Pyruvate Kinase M2 (PKM2) (37). PKM2 is an isoform of the highly important pyruvate kinase that catalyzes the last conversion in the glycolysis to pyruvate. Dephosphorylation and tetramerization of PKM2 leads to more OXPHOS, an inhibition of the Warburg effect, and increased apoptosis.

PA is a far less recognized SCFA compared to BA in the context of CRC efficacy, but still has shown anti-cancer properties. PA has also shown to possess anti-cancer properties such as modulating inflammation and oxidative stress as well as inducing apoptosis in various cancers (38,39). In addition, PA has also shown evidence of HDAC inhibition (40). PA has been found to enhance the cytotoxic effect of the chemotherapeutic agent cisplatin (41).

Other studies have found that BA and PA can modulate the metabolism in cancer cells. Both of these SCFAs partially inhibit acetyl-CoA synthase activity, which decreases the uptake of

acetate by the mitochondria (42). Decreased acetate means less substrate for the TCA cycle and thus reduced energy production.
Given the evidence of anticarcinogenic effects of BA and PA, it is important to explore how BA and PA combined might work alongside conventional treatments, such as 5-fluorouracil, to improve outcomes for CRC patients.

1.2.6 Butyrate and Propionate as a Pretreatment to 5-Fluorouracil

5-fluorouracil, also named fluorouracil or 5-FU, is a common US Food and Drug Administration (FDA) approved chemotherapy drug used for the treatment of various cancers, including gastric-, pancreatic-, breast-, and colorectal carcinoma (43). 5-FU is the first-line therapy used for metastatic CRC (44). Due to its structure as a heterocyclic aromatic organic compound (**figure 1.4**), which functions as an analogue of uracil, 5-FU disrupts nucleoside metabolism, leading to cytotoxicity and apoptosis (45).

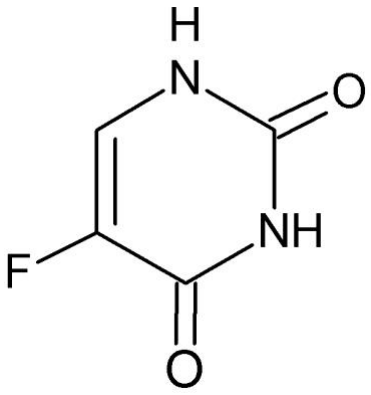

Figure 1.4 Chemical structure of 5-FU (46).

Despite 5-FU showing the highest treatment impact on CRC, the response rate to 5-FU alone in advanced CRC is only 10-15%. When combined with other anti-tumor drugs, the response improves to 40-50% (47). Thus, novel therapeutic strategies in terms of combinatorial treatments are of high importance to improve drug response rates. In fact, BA has already shown to inhibit glucose transport and glycolysis of CRC cells by reducing GLUT1 concentration which enhanced the chemotherapeutical efficacy of 5-FU (48).
Given the anticarcinogenic effect of both BA and PA. It is of high interest to test if these SCFAs combined can improve the efficacy of the conventional chemotherapeutic CRC agent 5-FU.

1.3 Normal Cell Metabolism

Normal cell growth, maintenance, and proliferation depends on a functioning cellular metabolism also called cellular respiration. For a cell to have the fuel to complete its tasks and maintain metabolic homeostasis, energy in the form of adenosine triphosphate (ATP) is required. Cellular energy is produced through a series of fundamental energetic pathways. These pathways are strictly controlled and depend on extra- and intracellular signaling as well as nutrient availability in the cell growth medium.

1.3.1 Glycolysis

Glycolysis is a fundamental metabolic pathway, and the first step in cellular respiration. It can occur in both aerobic and anaerobic conditions. Glycolysis is located in the cytosol of cells and the whole pathway can be divided into two phases: the investment- and the payoff phase (**figure 1.5**).

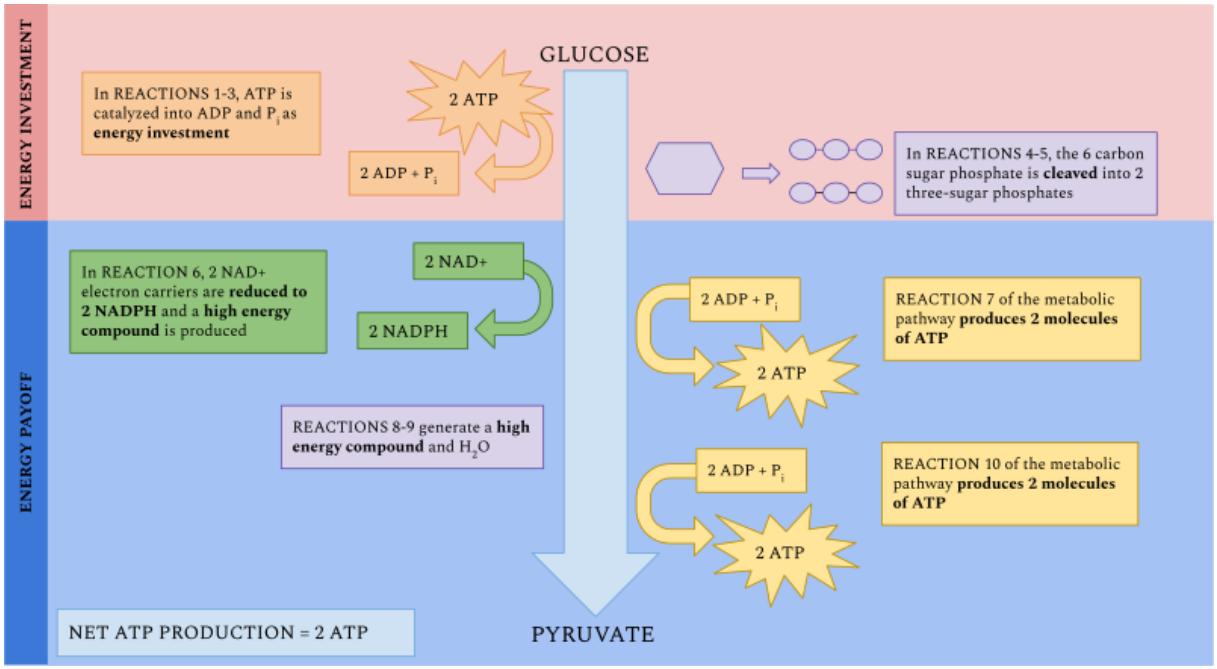

Figure 1.5 Glycolytic pathway

Simplified steps of the glycolytic pathway from glucose to pyruvate, divided into the investment phase and payoff phase. A net total of two ATP and two NADH molecules are produces for every glucose molecule (49).

In the investment phase, glucose is converted into a more reactive form, named glucose-6-phosphate, by using energy from ATP, hence investment. Another ATP is invested into

rearranging glucose-6-phosphate into fructose-6-phosphate and then into fructose-1,6-biphosphate. Fructose-1,6-biphosphate is further split into two glyceraldehyde-3-phosphate. The next step is the payoff phase, where the glyceraldehyde-3-phosphate molecules are converted through a series of steps into pyruvate. A total of four ATP molecules and two NADH molecules are produced in this phase, giving a net energy production of two ATP and two NADH per glucose molecule.

In anaerobic conditions, NADH produced in glycolysis cannot continue through oxidation, and the regeneration of NAD+ must occur in an alternative method to maintain energy levels. In such conditions, pyruvate is converted to lactate by lactate dehydrogenase, using NADH thus converting NADH to NAD+. In aerobic conditions, pyruvate is converted through the tricarboxylic acid cycle.

1.3.2 Tricarboxylic Acid Cycle

The tricarboxylic acid cycle (TCA cycle), also known as Krebs cycle or citric acid cycle, is a key part of the aerobic respiration and the second stage of normal cellular respiration in aerobic conditions and involves a repeating cycle of steps, starting with the end product from the glycolysis (**figure 1.6**). Pyruvate from the glycolysis is transferred from the cytosol into the mitochondria, where most of the glycolytic metabolism happens. Pyruvate is oxidized into acetyl CoA, the first molecule of the cycle.

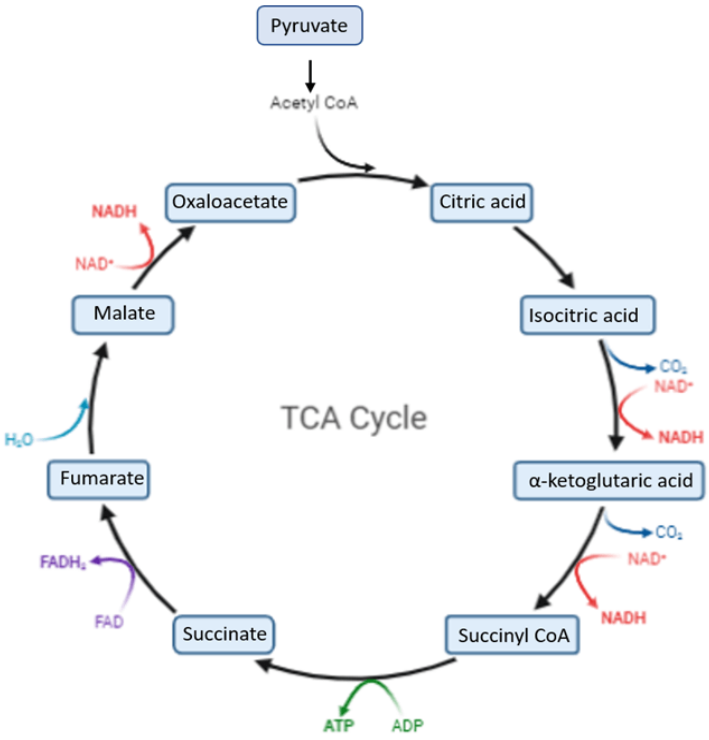

Figure 1.6 Overview of the steps of the TCA cycle.

Pyruvate is oxidized to acetyl CoA that proceeds through a series of enzymatic processes in a closed circle. The net total energy production in the TCA cycle is two ATP, three NADH, and one FADH2. These molecules are further used in the electron transport chain (50).

The TCA cycle begins with the condensation of acetyl-CoA, with oxaloacetate to form citrate. Through a series of enzymatic reactions, citrate is converted into isocitrate, α-ketoglutarate, succinyl-CoA, succinate, fumarate, malate, and finally back to oxaloacetate. During these reactions, carbon dioxide is released and reduced coenzymes such as NADH and $FADH_2$ are generated. Only one ATP molecule are produced in the TCA cycle, but a total of three NADH and one $FADH_2$ molecules are generated per cycle. These molecules play an important role in transferring electrons to the electron transport chain, where most of the ATP in cellular respiration is produced.

1.3.3 Oxidative Phosphorylation

The oxidative phosphorylation (OXPHOS) occurs in the inner mitochondrial membrane and stands as the final stage of aerobic cellular respiration. Electrons from the produced NADH and $FADH_2$ combine with oxygen to synthesize ATP from ADP. The energy required for this synthesis must be gradually produced by the passage of electrons in a process called the electron transport chain (ETC).

The ETC consists of four membrane embedded carrier complexes, named I-IV (**figure 1.7**).

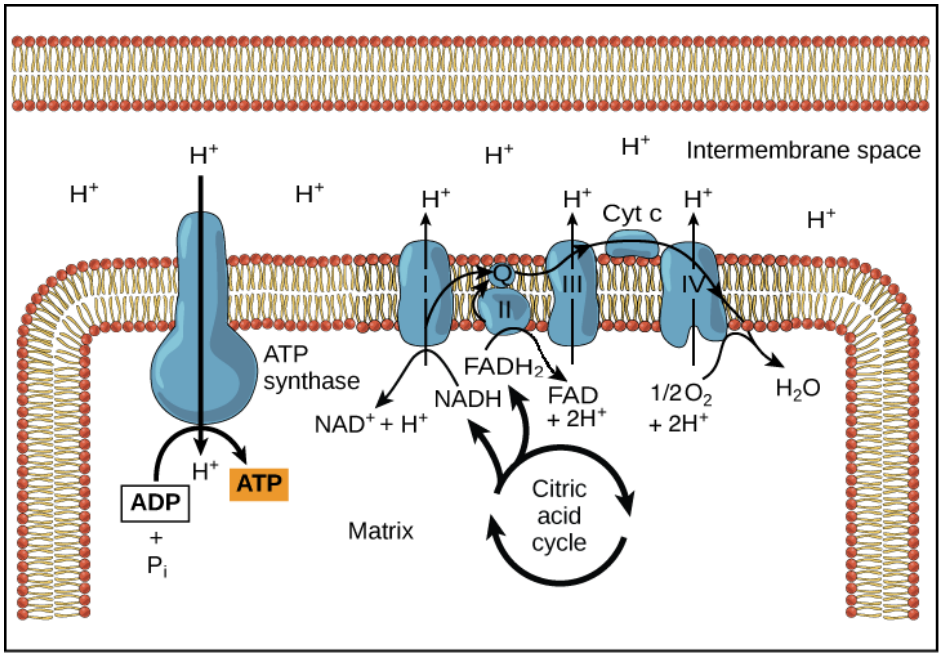

Figure 1.7 The four complexes of the electron transport chain and ATP synthase.

Electrons of NADH and FADH2 are passed through the complexes to create a proton gradient in the intermembrane space that flows through ATP synthase to produce ATP (51).

In complex I, the flavin mononucleotide accepts electrons from NADH and passes these electrons to an iron-sulfur protein, and finally to coenzyme Q, also called ubiquinone. Electrons from $FADH_2$ are also deposited in the ETC but is processed initially through complex II before ubiquinone.

From there, ubiquinone delivers electrons from complex I and II to complex III, where they are transferred from cytochrome b to cytochrome C. Cytochrome C carries the electrons to complex IV where they are transferred to O_2 to form water. The important function of the ETC consists of regenerating NADH and $FADH_2$ to their oxidized forms. This is important because NAD+ and FAD can be reused in the glycolysis and TCA. The oxidation also generates a proton gradient in the intermembrane space which continues to the last step.

The last step of the OXPHOS is called chemiosmosis and involves a membrane-spanning protein named ATP synthase. As the protons move down their concentration gradient through ATP synthase, ADP is transformed into ATP. Approximately 32 ATP molecules are generated in the OXPHOS, making the net energy production of the total cellular respiration 38 ATP.

While the glycolysis, TCA cycle, and OXPHOS efficiently produces ATP, cells also require other biological building blocks such as reducing power and precursors for growth and maintenance. This is where interplay between the different metabolic pathways becomes important for the metabolic homeostasis. One of these pathways is the pentose phosphate pathway.

1.3.4 Pentose Phosphate Pathway

The Pentose Phosphate Pathway (PPP) is essential for the production of nucleotide- and amino acid precursors, to maintain carbon homeostasis, to produce reducing molecules for anabolism, and to reduce oxidative stress (52). PPP branches off the glycolysis from glucose 6-phosphate in the cytosol and is further processed through the oxidative- and non-oxidative phase of the PPP (**figure 1.8**)

In the oxidative phase, glucose 6-phosphate is oxidized to 6-phosphogluconolactone with the reduction of $NADP^+$ to NADPH. Next, 6-phosphogluconolactone is transformed into 6-phosphogluconate. From here, a carbon is cleaved, and CO_2 is released as well as another reduction of $NADP^+$ to NADPH to form ribulose-5-phosphate. The two NADPH produced provides reducing power to the synthesis of lipids and cholesterol, as well as the production of reduced glutathione, which regulates reactive oxygen species (ROS) (53). Each step in the oxidative phase of the PPP is irreversible.

In the non-oxidative phase, the reaction stands as reversible, allowing for molecules to enter the PPP in different stages of the reactions. The non-oxidative phase continues from ribulose-5-phosphate into either xylulose 5-phosphate or ribose-5-phosphate. Ribose-5-phosphate is the precursor to the sugar of DNA and RNA. The remainder of the non-oxidative cycle is dependent on the cell´s need and can either end up as erythrose-4-phosphate, a contributor to the formation of amino acids, or as glyceraldehyde-3-phosphate that returns to the glycolysis (53).

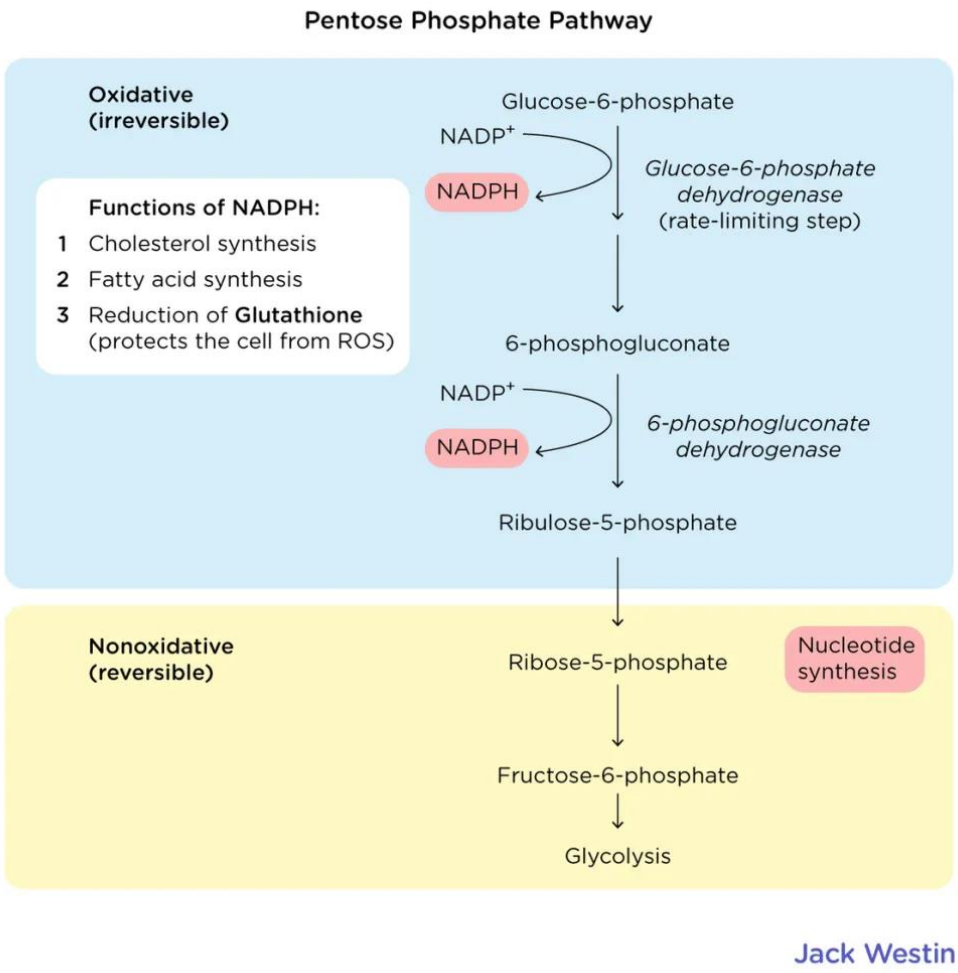

Figure 1.8 Schematic of the pentose phosphate pathway.

In the oxidative section, glucose-6-phosphate is converted to ribulose-5-phosphate to produce NADPH. The nonoxidative section creates sugars for nucleotide synthesis. The end product can enter as an intermediate in the glycolysis (54).

Under normal physiological conditions, these metabolic pathways are finely tuned to respond to the cell´s needs and requirements. However, alterations in metabolic regulation is often observed in pathological states, such as cancer.

1.4 Hallmarks of Cancer

The eight hallmarks of cancer describe the unique capabilities acquired by cancer cells as a way of organizing and rationalizing the complexity of the disease (**figure 1.9**). These hallmarks include sustaining proliferate signaling, evading growth suppressors, resisting cell death, enabling replicative immortality, inducing angiogenesis, activating invasion and metastasis, deregulating cellular energetics and metabolism, and avoiding immune destruction (55).

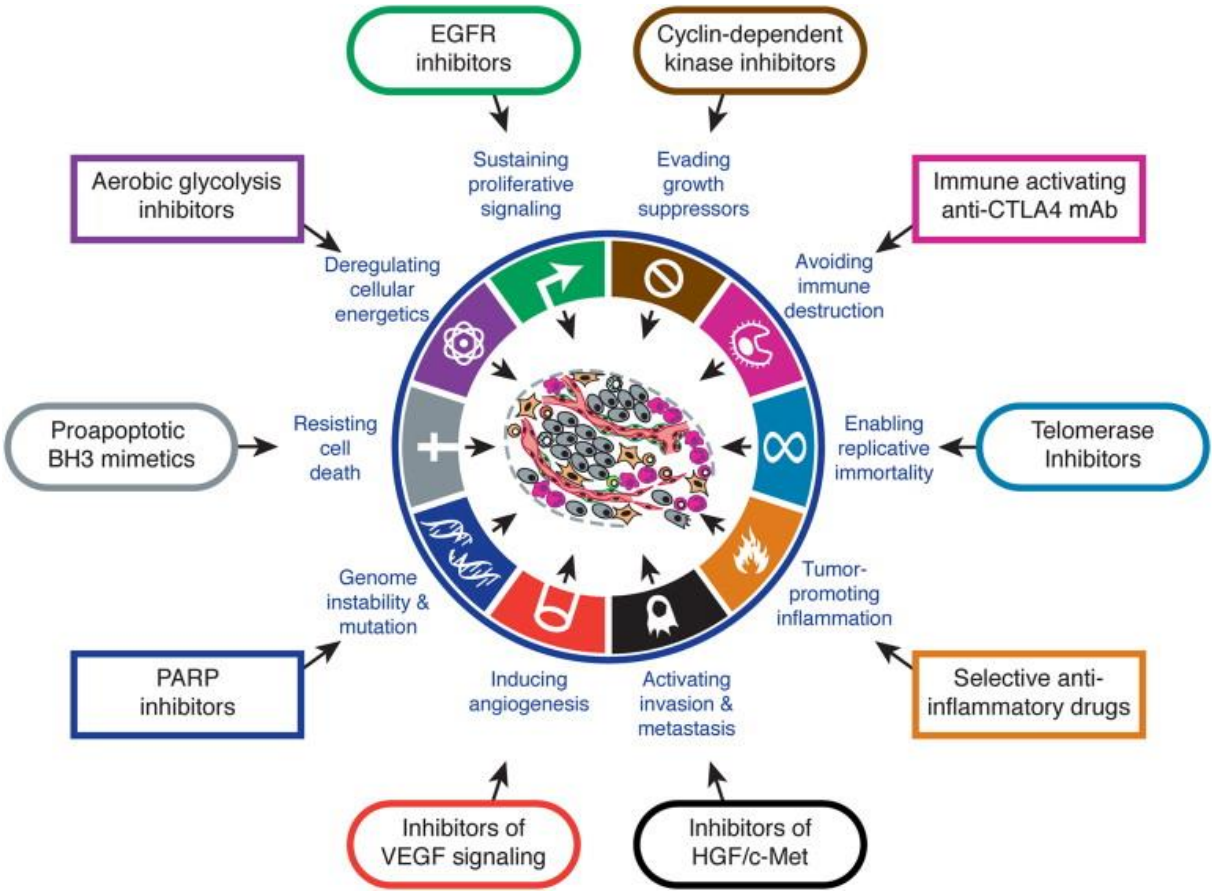

Figure 1.9 The Hallmarks of Cancer and their therapeutic targeting (56).

The emerging hallmark of reprogrammed energy metabolism is described as a deregulated control of cell proliferation and adjustments of energy metabolism. This deregulation is caused by cancer cells´ ability to limit their metabolism to glycolysis, even in the presence of oxygen, rather than the normal mitochondrial OXPHOS, otherwise referred to as “the Warburg effect” by its discoverer Otto Warburg in the end of 1920s (57).

1.5 Cancer Cell Metabolism

Cancer cell metabolism is characterized by a high degree of adaptability to support uncontrolled proliferation. Metabolic alterations provide cancer cells with the necessary energy, building blocks, and redox balance for sustained growth and resisted cell death. Reprogrammed metabolism is shown to be a typical hallmark of CRC (52).
Mitochondria are key organelles in cellular physiology. They regulate essential functions such as biosynthesis, metabolism, ATP production, redox balance, and apoptotic signaling pathways (58). These bioenergetic functions also provide cancer cells with building blocks to support tumor growth and survival as well as contribute to metastasis (59). A dysfunctional mitochondria in cancer cells can be caused by mutations in mitochondrial DNA (mtDNA), mitochondrial enzyme defects, and dynamic changes (60).

1.5.1 The Warburg Effect

The paradox of a metabolic phenotype was first observed by Otto Warburg in 1924 (57). Despite aerobic conditions, cancer cells will preferably utilize glycolysis followed by lactic acid fermentation rather than the OXPHOS metabolism. OXPHOS yields more ATP per glucose molecule, however glycolysis generates ATP more rapidly (61). Moreover, increased glycolysis also facilitates the conversion of glycolytic intermediates into essential macromolecules required to sustain rapid cell proliferation, an example being the PPP, where intermediates are converted for the synthesis of nucleotides. The decline in OXPHOS is also believed to function as a defense mechanism from reactive oxygen species (ROS) which can arise during rapid cell proliferation (62).

ROS are defined as radicals, ions or molecules with a single unpaired electron, which makes them highly reactive. ROS are produced as a byproduct of OXPHOS in the mitochondria, and can contribute to enhanced apoptosis by mitochondrial dysfunction, activation of apoptotic pathways, and oxidative damage to DNA (63). In cancer cells, increased ROS can result from increased metabolic activity, and mitochondrial dysfunction, oncogene activity.

The Warburg effect of cancer cells does not necessarily indicate a dysfunctional OXPHOS. CRC typically has a downregulation of the mitochondrial pyruvate carrier (MPC) that causes increased aerobic glycolysis (61). Cancer cells, including CRC cells, continue to use the TCA

cycle and OXPHOS to generate ATP, but more fueled by other intermediate metabolites such as glutamine and/or FAs through beta oxidation (**figure 1.10**).

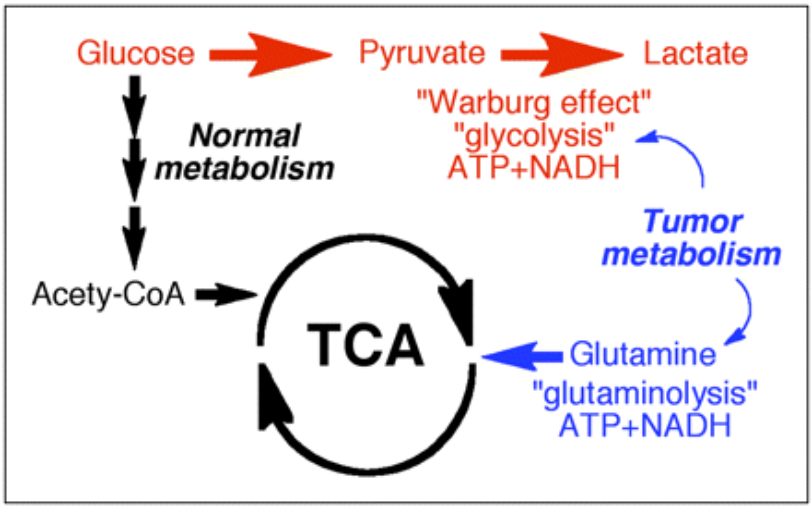

Figure 1.10 Warburg effect

Metabolic shift in cancer cells, also known as the Warburg effect. Pyruvate from the glycolysis is continued to lactate instead of the TCA cycle, even in aerobic conditions (64).

1.5.2 Glutaminolysis

Glutamine is the most abundant amino acid in the blood and muscles, and is used as a source of nitrogen and carbon (65). In cancer, glutamine supports fundamental cell functions and many cancer cells have shown to have higher glutamine consumption rates (66). As previously mentioned, glutamine dependency in cancer cells is closely correlated with the Warburg metabolism because glutamine is utilized to replenish the TCA cycle (**figure 1.11**). Glutamine is deaminated to glutamate by glutaminase 1 (GLS1) and then further converted to α-ketoglutarate (αKG) by glutamate dehydrogenase (GDH). α-KG can be utilized to synthesize both lipids, amino acids, and ATP via the TCA and OXPHOS metabolism. NADPH is also produced during these reactions, which can be used to regenerate glutathione (GSH), an electron acceptor that neutralizes ROS (61). Both GLS1 and GHD are upregulated enzymes in CRC and maintains the viability of cancer cells by ATP production and the synthesis of proteins, lipids, and nucleotides (67,68).

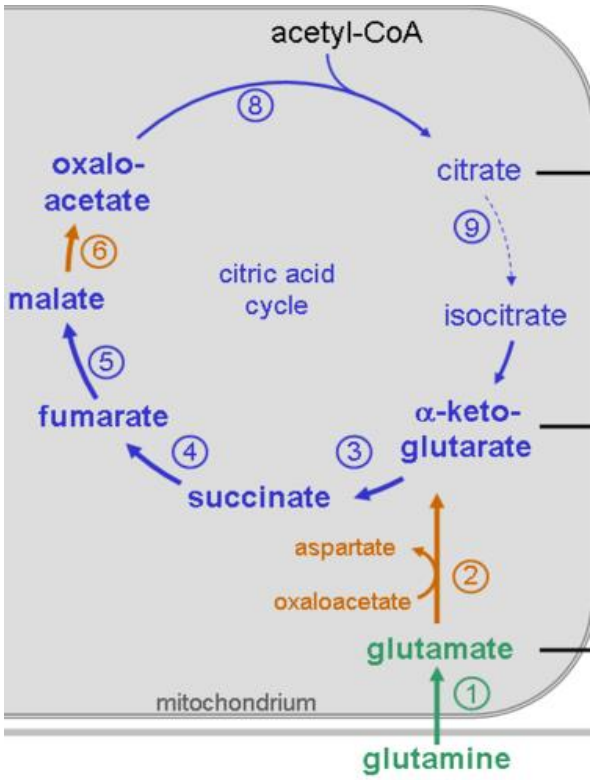

Figure 1.11 The glutaminolytic pathway.

Glutamine is ultimately converted into α-ketoglutarate which can enter the TCA cycle as an intermediate (69).

1.6 2D and 3D Cell Cultures

Cell culture systems are a widely used *in vitro* tool, often used in preclinical research, to better the understanding of cell biology, tissue morphology, mechanisms of diseases, drug action, protein production, and tissue engineering (70). One can either use primary cells isolated directly from a donor's material or use established cell cultures available from cell banks. A primary cell culture offers closer *in vivo* features but has a short life span. Established cell cultures, on the other hand, are more homogeneous compared to primary cells and many can proliferate indefinitely, allowing for long term studies.

Cells in a 2D model is the most commonly used method. Cells grow as a monolayer on a flat surface, often in a culture flask or in a petri dish (71). A 2D culture has low maintenance and cost, making them easy to manage and observe, but also offers several disadvantages. 2D cultured cells do not properly represent the tumor microenvironment as they lack cell-cell and cell-matrix interactions. They have a reduced differentiation which can limit the study of cell functions, as well as a uniform nutrient and waste distribution (70).

A more emerging method of cell culture is the 3D model where cells grow in a spheroid structure, forming various layers. This model better mimics the physiological and biochemical features of an actual tumor. 3D cell cultures can be grown with or without a supporting scaffold. In a scaffold free 3D cell culture, the cells self-assemble into clusters or spheroids. Methods includes low adhesion plates, preventing cells from adhering to the surface, or the hanging drop method where cells aggregate and form spheroids at the bottom of a medium droplet (72).

In this study, we will utilize the established CRC cell lines HCT116, SW948, and Caco-2 as 2D models in a cell culture flask, as well as scaffold-free 3D spheroids formed in low adhesion plates to examine the effects of BA and PA.

2. Rationale and Aims

2.1 Rationale

CRC remains a significant public health challenge due to its high prevalence and mortality rates (3). The current therapeutic strategies towards CRC, including chemotherapy with agents such as 5-FU, are limited by issues such as chemotherapy resistance and toxicity (47). Therefore, the critical need for novel approaches that enhance the efficacy of existing treatments arises. Especially treatments that target cancer cell metabolism, a hallmark which is often altered in CRC (73).

SCFAs, such as BA and PA, are naturally occurring compounds produced by the fermentation of dietary fibers in the gut, and have previously shown potential in modulating cancer cell viability and metabolism as well as being associated with anti-cancer properties, including the ability to induce apoptosis and the inhibition of proliferation (38,74–76).

Given the emerging hallmark of metabolic reprogramming observed in cancer cells, which often involves increased glucose uptake and altered mitochondrial function, it is of interest to understand how CRC cells respond to these SCFAs under different metabolic conditions. The influence of glucose availability on the efficacy of BA and PA treatments is another point to investigate more closely. Ultimately, the combination of these SCFAs might offer synergistic effects that could enhance their anti-cancer properties and increase chemotherapy efficacy.

2.2 Aims

1. Investigate the viability of CRC cell lines under different glucose conditions with singular treatments of BA and PA.
2. Analyze the metabolic response of CRC cell lines to singular treatments of BA and PA.
3. Evaluate the combined effect of BA and PA on the viability of CRC cell lines under different glucose conditions.
4. Examine the impact of BA/PA pretreatment on the sensitivity of CRC 3D spheroids to 5-FU chemotherapy.

3. Materials and Methods

3.1 Materials

Materials used in this research have been listed in Appendix A.

3.2 Cell Lines

All cell lines used in this study originate from colorectal cancer with distinct molecular profiles (**table 3.1**). Employing multiple cell lines allow us to capture the diverse responses of colorectal tumors to experimental interventions, enhances the generalizability of our findings, validates results across different models, and provides insights into tumor heterogeneity, aiding in the development of targeted therapies.

Table 3.1 Cell Lines

General information regarding cell lines Caco-2, HCT116, and SW948 provided by ECACC and ATCC.

Cell Line Name	Citation Guidance	Keywords
Caco-2	ECACC 86010202	Human Caucasian colon adenocarcinoma
HCT116	ECACC 91091005	Human colon carcinoma
SW948	ATCC CCL-237	Dukes´type C, grade III, colorectal adenocarcinoma

3.1 Introduction to Methods

3.2.1 Cell Density Optimization

Optimizing cell density is a critical aspect of experimental design in cell-based assays, directly influencing the reliability and robustness of subsequent analyses. The rationale behind cell density optimization lies in achieving a balance, where the cellular response is both measurable and reflective of the physiological conditions of interest. An insufficient cell density may result in weak signal intensity, which may compromise the sensitivity of the assays. Conversely, excessive cell density can lead to nutrient depletion and altered cellular metabolism, potentially skewing the assay results. Therefore, establishing an optimal cell density is pivotal for obtaining accurate and meaningful results in both the CCK-8 and Seahorse assays.

3.2.2 Cell Counting Kit-8 Viability Assay

The CCK-8 cell viability assay, short for Cell Counting Kit-8, is a widely used laboratory technique designed to measure the quantitative viability of cells in a culture. It's a simple and efficient method that provides valuable information about how well cells are thriving and dividing by utilizing the highly water-soluble tetrazolium salt WST-8 [2-(2-methoxy-4-nitrophenyl)-3-(4-nitrophenyl)-5-(2,4-disulfophenyl)-2H- tetrazolium, monosodium salt], which produces a water-soluble formazan dye when reduced by dehydrogenases as shown in **figure 3.1**.

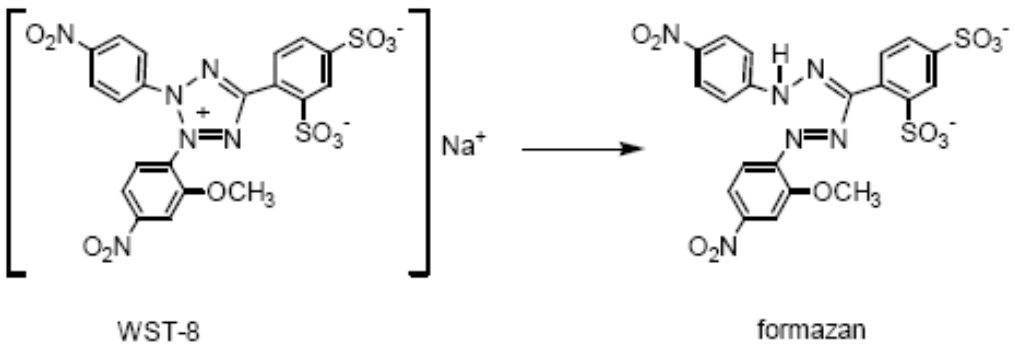

Figure 3.1 Formation of formazan from the reduction of WST-8 (77).

The amount of the formazan dye generated is directly proportional to the amount of living cells.

3.2.3 Agilent Seahorse XF FCCP Titration and Cell Mito Stress Test

ATP in mammalian cells is generated through either OXPHOS or glycolysis. As previously mentioned, cancer cells shift their metabolism based on their energetic and anabolic needs and they possess unique metabolic features which makes mitochondria a potential target for anticancer therapy.

A Seahorse XF Cell Mito Stress Test will be used in order to measure the real time oxygen consumption rate (OCR) as a parameter of mitochondrial function.
Modulators of respiration are added through built-in injection ports on the XF sensor cartridges during the assay. These modulators include oligomycin, carbonyl cyanide-4 (trifluoromethoxy) phenylhydrazone (FCCP), rotenone, and antimycin A. The injection sequence and parameters of the given modulators are depicted in **figure 3.2**.

FCCP stands as a robust uncoupling agent, inducing the disturbance of ATP synthesis by transporting protons across mitochondria cell membranes. This action prompts an increase in respiration or OCR. FCCP aids in gauging the maximum respiratory capacity of a cell. However, it is crucial to fine-tune the concentration of FCCP used in estimating maximal respiration through titration experiments, as elevated concentrations of FCCP can disrupt OCR. Optimization experiments should be tailored to each cell type since the ideal FCCP concentration is dependent on the specific characteristics of the cell line.

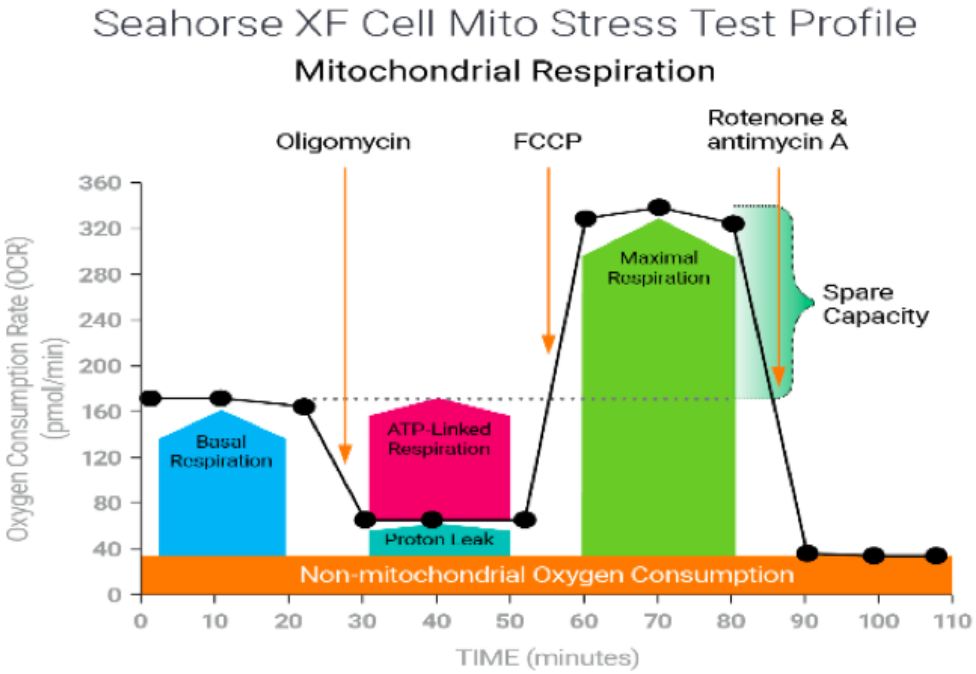

Figure 3.2 : Agilent Seahorse XF Cell Mito Stress Test profile with key parameters of mitochondrial function (78).

Each of these modulators target different complexes in the ETC shown in **figure 3.3**.

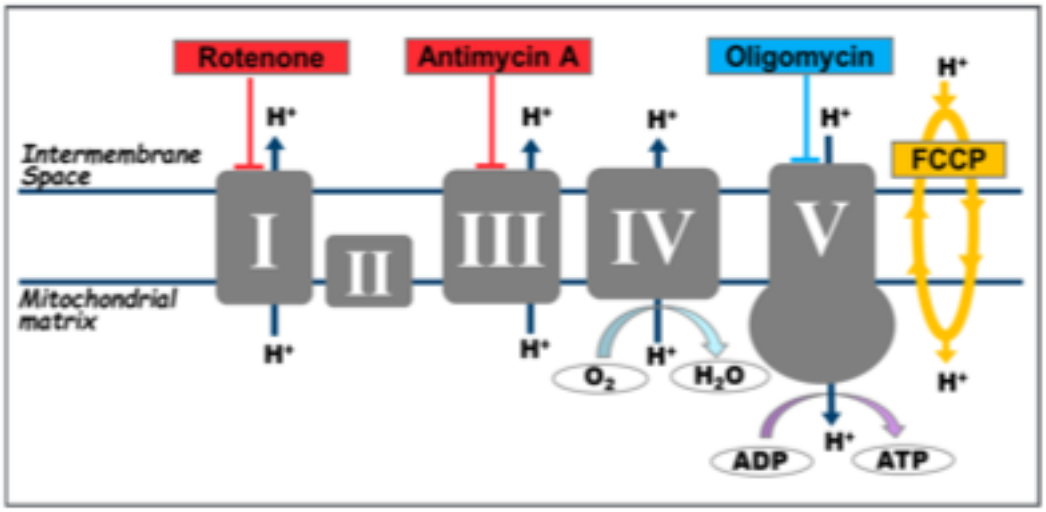

Figure 3.3 Agilent Seahorse XF Cell Mito Stress Test modulators of the ETC (78).

The first injection, following basal respiration measurements, is oligomycin which inhibits complex V, aka ATP synthase. Electron flow through the ETC is compromised, leading to a

decrease in mitochondrial respiration and OCR. Next, FCCP targets the inner mitochondrial membrane potential and collapses the proton gradient thus creating a free flow of electrons through the ETC, leading to an increase in OCR. The last injection is a mixture of rotenone and antimycin A, which inhibits complex I and III, respectively. Consequently, mitochondrial respiration completely shuts down, enabling the calculation of nonmitochondrial respiration.

3.3 Methods

3.3.1 Sterile Techniques

All sterile procedures were conducted within a biosafety level-2 (BSL-2) cell laboratory. Personnel wore appropriate personal protective equipment (PPE), including lab coats and gloves, to minimize the risk of contamination.
Prior to each session, biosafety cabinets and all equipment were meticulously cleaned and disinfected using 70% ethanol solution. Sterile disposable items such as pipette tips were autoclaved before use and handled exclusively within the confines of the biosafety cabinets.

Following completion of procedures, the biosafety cabinet was subjected to thorough decontamination using 70% ethanol, followed by exposure to UV-light for 30 minutes to ensure elimination of any potential contaminants. These measures were implemented to maintain the sterility of experimental materials and avoid contamination of cell cultures to secure reproductible experimental settings.

3.3.2 Complete Cell Media

The cell culture media utilized in this study was based on Dulbecco's Modified Eagle's Medium (DMEM). The following supplements were added to the DMEM: Fetal Bovine Serum (FBS), Penicillin-Streptomycin (PenStrep), L-glutamine, and glucose (**table 3.2**).

Two glucose concentrations, 0.5 mM and 5.0 mM were employed to investigate the effects of physiological glucose concentration versus glucose deprivation. This approach allows for the examination of cellular responses under varying metabolic conditions, providing insights into the role of glucose availability in cancer cell behavior.

Table 3.2 Components of the Complete DMEM.

Component	Volume (mL)
DMEM without glucose, L-glutamine, and sodium pyruvate	500
FBS, heat inactivated	50
PenStrep solution	5
L-glutamine 200 mM	5
Glucose 1M	2.5 (5 mM)/0.25 (0.5 mM)

3.3.3 Cell Cryo-Preservation

The cell lines utilized in this study were cryopreserved in liquid nitrogen (-196°C) for long-term storage. Upon retrieval, cryotubes containing the cells were gently thawed at room temperature to prevent thermal shock. The culture flasks were supplemented with 10 mL of prewarmed complete cell growth media maintained at 37°C. Each culture flask was labeled with the cell line name, passage number, and date of initiation. Each cell line was transferred into separate 75 cm^2 culture flasks, ensuring one flask per cell line. The labeled flasks were then placed in a standard cell culture incubator set to 37°C with 5% CO_2 to provide optimal growth conditions for the cultured cells.

3.3.4 Cell Culturing and Passaging

Adherent cell lines grew as a monolayer on the surface of 75 cm^2 tissue flasks containing 10 mL of complete DMEM. To ensure optimal growth conditions, the cell growth media was refreshed every other day, replenishing nutrients essential for cellular proliferation.
Upon reaching approximately 80% confluency, observed under an Olympus CKX41 Light Microscope, cells were passaged using the following procedure:

All cell growth media was aspirated, and the flask was rinsed with 5 mL of phosphate-buffered saline (PBS) to remove residual media and cellular debris. Subsequently, 2 mL of Trypsin-EDTA solution was added to the flask and placed in the incubator for an appropriate duration until the cells detached from the flask surface. The trypsin activity was neutralized by adding and dispersing 3 mL of complete growth media, halting further enzymatic digestion.

The resulting cell suspension was either utilized immediately for experimental purposes or split, typically at a ratio of 1:5 or 1:10, and seeded into new tissue flasks for continued culture. The splitting procedure was performed approximately every 7 days.

3.3.5 Muse Cell Count and Viability Assay

The Muse Cell Count and Viability Assay served as a tool for determining the accurate volume of cell suspension required to achieve desired cell density in the assays conducted in this study.

To perform the assay, a specified volume of Muse Count and Viability reagent was combined with the cell suspension (**table 3.3**) in a microcentrifuge tube. The mixture was thoroughly vortexed to ensure homogeneous distribution and then incubated for 5 minutes in darkness.

Table 3.3 Muse Cell Count and Viability Assay Dilutions

Number of cells in suspension (cells/mL)	Dilution Factor	Cell Suspension Volume (uL)	Count and Viability Reagent Volume (uL)
$1x10^5$ to $1x\ 10^6$	10	50	450
$1x10^6$ to $1x\ 10^7$	20	20	380

After incubation, the solution was vortexed and loaded into the Muse instrument for analysis. The first step involved eliminating any debris or dead cells in the solution by adjusting the viability plot, as depicted in **figure 3.4**.

The number of viable cells per mL, along with the viability percentages and the total number of cells per mL, were determined during the analysis. These quantitative measurements provided essential parameters for downstream assays, ensuring accurate and consistent cell densities in subsequent experimental procedures.

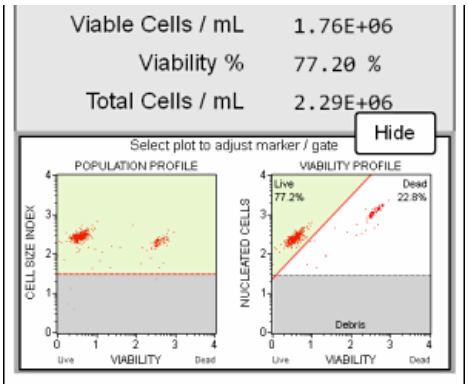

Figure 3.4 Data output and viability plot for the Muse Count and Viability Assay (79).

3.3.6 BA and PA Solutions

The BA- and PA solutions utilized in the experiments were prepared from their solid sodium salts using **equation 3.1**:

Equation 3.1

$$g = c_{stock} * V_{target} * Mw_{BA/PA}$$

This equation provided guidance on the amount of sodium butyrate or sodium propionate required, and the volume was adjusted accordingly to achieve the exact concentration. Sodium butyrate or sodium propionate was then diluted in autoclaved water to prepare a 100 mM stock solution for use in the experiments. To further ensure the purity of the solutions, they were filtered through a 40 µm filter to remove any impurities that may interfere with the experimental results. After preparation, the solutions were stored in the refrigerator until use. For the specific BA and PA treatments, the 100 µM stock solution was diluted with complete DMEM in 1.5 mL Eppendorf tubes. The concentration ranges used for the following experiments (**table 3.4**) are based on preliminary studies. Zhang et al. used BA in a concentration range of 0.5-5 mM on HCT116 and HT-29 cell lines (80), while Pham et al. used a PA concentration range of 0-50 mM on cervical cancer cell lines (75).

Table 3.4 Concentrations of BA and PA utilized in the singular and combinatorial treatment experiments.

Butyrate (mM)	Propionate (mM)	Butyrate + Propionate (mM)
1-5	5-10	Combination of all the singular treatments

The concentrations were to be added in a 100 µL volume into each well. However, to compensate for the 100 µL of media already present in each well before the addition of the treatment, the target concentration of each treatment was doubled. By doubling the target concentration, the final concentration achieved in each well accounted for the residual media volume, resulting in the desired concentration for treatment.

3.3.7 Cell Counting Kit-8 Viability Assay

To achieve the desired cell density for experimentation, a cell suspension was prepared using **equation 3.2**:

Equation 3.2

$$V_{cell\ suspension}\ (mL) = \frac{Target\ cell\ density * number\ of\ wells}{viable\ cells/\ mL}$$

$$V_{media}\ (mL) = (number\ of\ wells * 0{,}2\ mL) - V_{cell\ suspension}$$

Once the cell suspension and media were mixed, 200 µL of the cell solution was added to each well of the 96-well plates. After settling, the cells were exposed to the desired treatment. Following the treatment period, a 10% concentration of the WST-8 reagent was added to each individual well. The plates were then incubated for 4 hours to allow for the conversion of WST-8 to formazan by viable cells.

After the incubation period, the absorbance of the formazan product was measured at 450 nm using a SpectraMax Paradigm microplate reader, equipped with SoftMax Pro 6 Software. The absorbance readings provided quantitative data on cell viability and metabolic activity, which were further analyzed to assess the effects of the treatment on the cells.

3.3.8 CCK-8 Viability Assay Cell Density Optimization

The three colorectal cancer cell lines were seeded in 96-well plates in increasing cell densities, ranging from 5000 to 30000 cells, in 4 biological replicates. The cells were further incubated for a standardized period of 48 hours. In the final 4 hours of the incubation period,

the CCK-8 reagent was introduced to each well and measured at 450 nm before being analyzed.

3.3.9 CCK-8 BA and PA 48H Singular and Combinatorial Treatments

Following the determination of optimal cell density, each cell line was seeded into a 96-well plate at the established density. To ensure robustness and reliability, three replicates were performed for each individual treatment, in addition to a negative control (media only) and an untreated control. The experimental setup is illustrated in **figure 3.5**. Two independent experiments were conducted, resulting in a total of six biological replicates per treatment condition.

To minimize the potential effects of evaporation and maintain consistent experimental conditions throughout the assay period, wells surrounding the wells containing the cells were loaded with PBS for insulation. This measure helped to stabilize the microenvironment within the wells and minimize variability in the experimental outcomes.

It's important to note that this experimental procedure was executed for both glucose concentrations tested, namely 0.5 mM and 5.0 mM. This approach allowed for the comprehensive evaluation of the effects of CCK-8 BA and PA singular and combinatorial treatments across different glucose conditions, providing valuable insights into the metabolic responses of the cells under varying nutrient availability.

plate 1	1	2	3	4	5	6	7	8	9	10	11	12
A	PBS	PBS	PBS	PBS	PBS	PBS	PBS	PBS	PBS	PBS	PBS	PBS
B	PBS	neg. ctrl	5 mM PA	15 mM PA	35 mM PA	1 mM BA	2 mM BA	4 mM BA	PBS	PBS	PBS	PBS
C	PBS	neg. ctrl	5 mM PA	15 mM PA	35 mM PA	1 mM BA	2 mM BA	4 mM BA	PBS	PBS	PBS	PBS
D	PBS	neg. ctrl	5 mM PA	15 mM PA	35 mM PA	1 mM BA	2 mM BA	4 mM BA	PBS	PBS	PBS	PBS
E	PBS	0 mM	10 mM PA	25 mM PA	50 mM PA	1.5 mM BA	3 mM BA	5 mM BA	PBS	PBS	PBS	PBS
F	PBS	0 mM	10 mM PA	25 mM PA	50 mM PA	1.5 mM BA	3 mM BA	5 mM BA	PBS	PBS	PBS	PBS
G	PBS	0 mM	10 mM PA	25 mM PA	50 mM PA	1.5 mM BA	3 mM BA	5 mM BA	PBS	PBS	PBS	PBS
H	PBS	PBS	PBS	PBS	PBS	PBS	PBS	PBS	PBS	PBS	PBS	PBS

plate 2	1	2	3	4	5	6	7	8	9	10	11	12
A	PBS	PBS	PBS	PBS	PBS	PBS	PBS	PBS	PBS	PBS	PBS	PBS
B	PBS	5 PA+1 BA	5 PA+2 BA	5 PA+4 BA	10 PA+1 BA	10 PA+2 BA	10 PA+4 BA	15 PA+1 BA	15 PA+2 BA	15 PA+4 BA	PBS	PBS
C	PBS	5 PA+1 BA	5 PA+2 BA	5 PA+4 BA	10 PA+1 BA	10 PA+2 BA	10 PA+4 BA	15 PA+1 BA	15 PA+2 BA	15 PA+4 BA	PBS	PBS
D	PBS	5 PA+1 BA	5 PA+2 BA	5 PA+4 BA	10 PA+1 BA	10 PA+2 BA	10 PA+4 BA	15 PA+1 BA	15 PA+2 BA	15 PA+4 BA	PBS	PBS
E	PBS	5 PA+1.5 BA	5 PA+3 BA	5 PA+5 BA	10 PA+1.5 BA	10 PA+3 BA	10 PA+5 BA	15 PA+1.5 BA	15 PA+3 BA	15 PA+5 BA	PBS	PBS
F	PBS	5 PA+1.5 BA	5 PA+3 BA	5 PA+5 BA	10 PA+1.5 BA	10 PA+3 BA	10 PA+5 BA	15 PA+1.5 BA	15 PA+3 BA	15 PA+5 BA	PBS	PBS
G	PBS	5 PA+1.5 BA	5 PA+3 BA	5 PA+5 BA	10 PA+1.5 BA	10 PA+3 BA	10 PA+5 BA	15 PA+1.5 BA	15 PA+3 BA	15 PA+5 BA	PBS	PBS
H	PBS	PBS	PBS	PBS	PBS	PBS	PBS	PBS	PBS	PBS	PBS	PBS

plate 3	1	2	3	4	5	6	7	8	9	10	11	12
A	PBS	PBS	PBS	PBS	PBS	PBS	PBS	PBS	PBS	PBS	PBS	PBS
B	PBS	25 PA+1 BA	25 PA+2 BA	25 PA+4 BA	35 PA+1 BA	35 PA+2 BA	35 PA+4 BA	50 PA+1 BA	50 PA+2 BA	50 PA+4 BA	PBS	PBS
C	PBS	25 PA+1 BA	25 PA+2 BA	25 PA+4 BA	35 PA+1 BA	35 PA+2 BA	35 PA+4 BA	50 PA+1 BA	50 PA+2 BA	50 PA+4 BA	PBS	PBS
D	PBS	25 PA+1 BA	25 PA+2 BA	25 PA+4 BA	35 PA+1 BA	35 PA+2 BA	35 PA+4 BA	50 PA+1 BA	50 PA+2 BA	50 PA+4 BA	PBS	PBS
E	PBS	25 PA+1.5 BA	25 PA+3 BA	25 PA+5 BA	35 PA+1.5 BA	35 PA+3 BA	35 PA+5 BA	50 PA+1.5 BA	50 PA+3 BA	50 PA+5 BA	PBS	PBS
F	PBS	25 PA+1.5 BA	25 PA+3 BA	25 PA+5 BA	35 PA+1.5 BA	35 PA+3 BA	35 PA+5 BA	50 PA+1.5 BA	50 PA+3 BA	50 PA+5 BA	PBS	PBS
G	PBS	25 PA+1.5 BA	25 PA+3 BA	25 PA+5 BA	35 PA+1.5 BA	35 PA+3 BA	35 PA+5 BA	50 PA+1.5 BA	50 PA+3 BA	50 PA+5 BA	PBS	PBS
H	PBS	PBS	PBS	PBS	PBS	PBS	PBS	PBS	PBS	PBS	PBS	PBS

Figure 3.5 96-well plate layout for the butyric Acid (BA) and propionic acid (PA)

Singular and combinatorial treatment with numbers representing the final compound concentration in mM and phosphate buffered saline (PBS) in surrounding wells to avoid medium evaporation. N=3 for each condition.

Subsequently, the plates were placed in the incubator to allow the cells to settle for 24 hours before the addition of treatments. Upon reaching the appropriate time point, 100 µL of media was removed from each well, and treatments were added in a volume of 100 µL to each corresponding well. Treatment concentrations were doubled to compensate for the 1:1 dilution in the well. The untreated cells received 100 µL of growth media only. Following treatment administration, the plates were returned to the incubator for an additional 44 hours to allow for the cellular response to the treatments.

After the incubation period, the cellular viability was assessed using the CCK-8 reagent. A 10% concentration of the CCK-8 reagent was added to each well, and the plates were further incubated for 4 hours to allow for the conversion of the reagent by viable cells. The absorbance of the solution was then measured at 450 nm using a microplate reader, and the resulting data were subjected to further analysis.

3.3.10 Agilent Seahorse XF Cell Mito Stress Test

The XF Cell Mito Stress Test was conducted over a two-day period. The day prior to the assay was dedicated to preparing the cell culture plate and hydrating the sensor cartridge. The assay workflow is illustrated in **figure 3.6**.

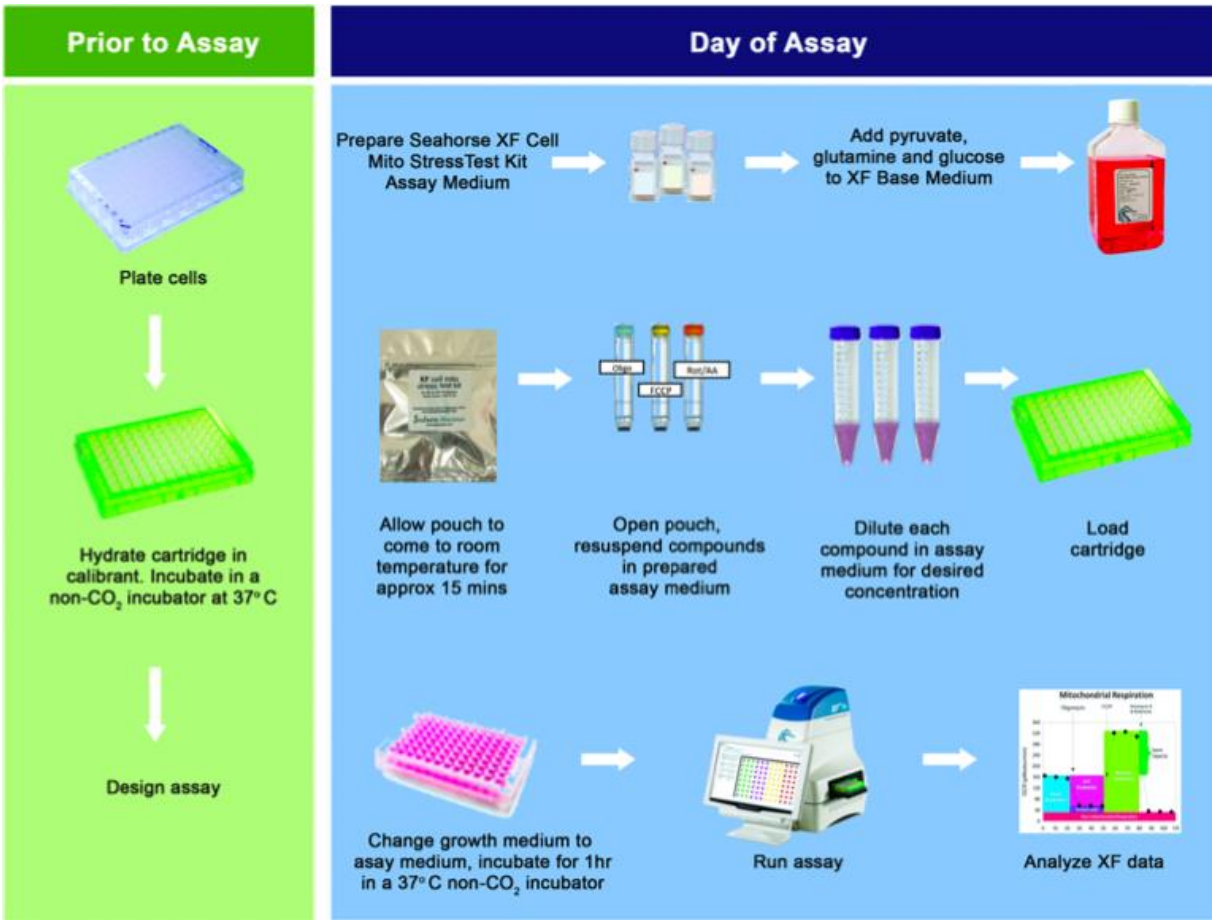

Figure 3.6 Workflow of the Seahorse Cell Mito Stress Test (78)

3.3.10.1 Day Prior to Assay

Cell density was determined using the Muse count and viability assay, ensuring consistent seeding densities across all wells. The cells were then seeded in Seahorse XF Cell Culture Microplates. To minimize edge effects and ensure uniform conditions during the assay, the corner wells of the microplate were left unseeded. Additionally, the sensor cartridge was hydrated by adding 200 µL of Seahorse XF Calibrant to each well of the calibration plate. The hydrated cartridge was then incubated overnight in a 37°C, non-CO_2 incubator to ensure proper equilibration and conditioning.

3.3.10.2 Day of the Assay

On the day of the assay, the assay medium was prepared by supplementing Seahorse XF DMEM medium with 1 mM pyruvate, 2 mM glutamine, and 10 mM glucose. This specific composition brought the medium to a pH of 7.4. However, adjustments to the medium

composition can be made to suit the requirements of different cell types or experimental conditions. The complete XF medium was warmed to 37°C in a water bath.
Next, the compound stock solutions and working solutions needed to be prepared. Each Seahorse XF Cell Mito Stress Test kit box came with one foil pouch containing three tubes with oligomycin, FCCP, and rotenone/antimycin A (AA). The stock solutions were prepared according to **table 3.5**.

Table 3.5 Stock solutions for the Seahorse XF Cell Mito Stress Test

Compound	Volume of Assay Medium (uL)	Stock Concentration (uM)
Oligomycin	630	100
FCCP	720	100
Rotenone/AA	540	50

The stock solutions were used to make the working solutions for the injection port on the sensor cartridges. The final concentration for the FCCP varied for each cell line, and was established by a titration experiment. For oligomycin and rotenone/AA, 1.5 uM and 0.5 uM was recommended, respectively, by the Agilent Seahorse XF Mito Stress Test protocol. Starting assay medium volume for the cell plate was 180 uL per well. The loading concentrations and volumes are described in **table 3.6**.

Table 3.6 Compound preparation for loading of the sensor cartridges.

	Final Well Concentration (uM)	Stock Solution Volume (uL)	Media Volume (uL)	Volume Added to Port (uL)
Port A, oligomycin	1.5	450	2550	20
Port B, FCCP	0.125	37.5	2962.5	22
	0.25	75	2925	22
	0.5	150	2850	22
	2.0	300	2700	22
	2.0	600	2400	22
Port C, rotenone/AA	0.5	300	2700	25

The solutions were loaded into the ports on the hydrated sensor cartridge. Loading volume and port designation are described in **table 3.7**.

Table 3.7 Seahorse XF Cell Mito Stress Test injection port and port volume

Port	Compound	Port Concentration	Loading Volume (uL)
A	Oligomycin	10X	20
B	FCCP	10X	22
C	Rotenone/AA	10X	25

Finally, the assay design was created on the XF96 controller, and the cartridge calibration was initiated and completed before being replaced with the cell culture plate to commence the assay.

3.3.11 Seahorse Cell Density Optimalisation and FCCP Titration

The FCCP titration experiment was conducted to determine the optimal concentration of FCCP for subsequent XF assays. This involved running six different FCCP concentrations to assess their effects on cellular respiration and determine the most appropriate concentration for further experiments. In addition to the FCCP titration, a cell density optimization was performed concurrently for unestablished cell lines. This optimization aimed to identify the optimal cell density for each cell line used in the following Seahorse XF assays.

Cells were seeded in Seahorse XF Cell Culture Microplates at 10k and 15k densities per well. The remaining protocol followed a standard Seahorse XF Cell Mito Stress Test, as described in “3.4.12 Agilent Seahorse XF Cell Mito Stress Test”, with the addition of increasing concentrations of FCCP as shown in **figure 3.7.**

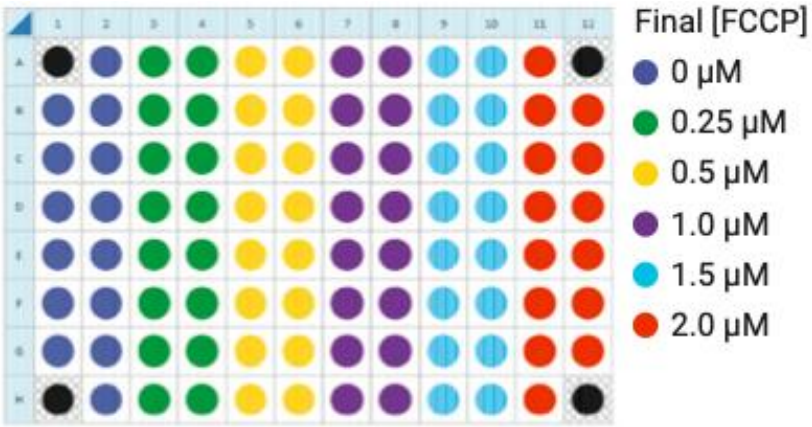

Figure 3.7 Example plate layout for the FCCP titration experiment (81).

Data analysis was conducted to determine which FCCP concentration was most suitable for the given cell line.

3.3.12 Seahorse Cell Mito Stress Test BA and PA Singular Treatments

Cells were seeded in Seahorse XF Cell Culture Microplates at the optimal density for the given cell line and allowed to settle for 24 hours. Singular treatments of BA and PA were then added to the corresponding wells in 3 biological replicates for 48 hours total. The rest of the assay was conducted according to the "Agilent Seahorse XF Cell Mito Stress Test" protocol using the established optimal FCCP concentration for each cell line.

3.3.13 BCA Protein Assay

The BCA Protein Assay is a widely used method for accurately quantifying protein concentration in biological samples. By determining the protein content of each well after the Seahorse XF Mito Stress Test, the assay provided a means to normalize the data to the actual number of cells present in each well. This ensured that any observed effects on mitochondrial function or cellular metabolism were attributable to the experimental manipulations rather than variations in cell density or protein content.

Preparation of diluted albumin (BSA) standards

An Albumin Standard (BSA) was used to make diluted standards according to **table 3.8**.

Table 3.8 Dilution scheme for albumin standards of the BCA assay.

Dilution Scheme for Standard Test Tube and Microplate Procedure (Working Range = 20-2000 µg/ml)

Vial	Volume of Diluent (µL)	Volume and source of BSA (µL)	Final BSA concentration (µg/mL)
A	0	300 of stock	2000
B	125	375 of stock	1500
C	325	325 of stock	1000
D	175	175 of vial B dilution	750
E	325	325 of vial C dilution	500
F	325	325 of vial E dilution	250
G	325	325 of vial F dilution	125
H	400	100 of vial G dilution	25
I	400	0	0 = blank

Preparation of BCA working reagent (WR)

Equation 3.3 was used to determine the total volume of WR required:

Equation 3.3

$$(\#standards + \#unknowns) * (\#replicates) * (volume\ of\ WR\ per\ sample) = total\ volume\ WR\ required$$

$$(9\ standards + 24\ unknowns) * (3\ replicates) * (200\ \mu L) = 19800\ \mu L = 19.8\ mL\ WR\ required$$

WR was prepared by mixing 50 parts of BCA reagent A with 1 part BCA reagent B.

Microplate procedure (sample to WR ratio = 1:8)

200 µL of the WR was added to each well and mixed thoroughly on a plate shaker for 30 seconds. The plate was further covered and incubated at 37°C for 30 minutes. The plate was cooled to room temperature and absorbance was read at 562 nm on a plate reader.

3.3.14 Viability Staining and Fluorescent Imaging of 3D Spheroids

To assess the viability of the spheroids following downstream treatment experiments, quantitative and qualitative measurements were obtained through the use of the fluorescent dyes Calcein AM and propidium iodide (PI). The concentrations of these dyes were

determined and established based on the protocol provided by Tia Tidwell (82). Calcein was applied at a concentration of 4 µg/mL and allowed to incubate overnight, while PI was added at a concentration of 7.5 µg/mL and incubated for approximately 10 minutes. Following the incubation period, the spheroids underwent two washes by replacing 70 µL of media with an equivalent volume of fresh media to remove any excess dye.
Fluorescence readings were taken at excitation/emission wavelengths of 494/517 nm for Calcein and 488/610 nm for PI. Fluorescent imaging of the stained spheroids was performed using a Nikon SMZ25 stereo microscope equipped with NIS Elements software (version 5.42.02: High content analysis package), allowing for visualization and analysis of the dye uptake and distribution within the spheroid structures.

3.3.15 3D Spheroid Density Optimization

To ensure optimal spheroid growth throughout the treatments, the density for each cell line needed to be optimized. For this purpose, each cell line was seeded in a 200 µL volume per well in low-attachment 96-well, PS, U-bottom CELLSTAR microplates, facilitating spheroid formation. The seeding density ranged from 5,000 to 50,000 cells per well in 4 biological replicates, allowing for a comprehensive exploration of spheroid growth dynamics. Following seeding, the spheroids were cultivated for a duration of 8 days, with 70 µL of growth medium replenished every 3 days to maintain optimal conditions for growth.

At both the 4th and 8th days of spheroid culture, imaging was conducted using a Nikon SMZ25 stereo microscope equipped with NIS Elements software (version 5.42.02: High content analysis package). The software facilitated the measurement of the total diameter of each spheroid. These measurements provided valuable insights into the growth kinetics and morphology of the spheroids over the course of the experiment. The collected data underwent further analysis, allowing for a quantitative assessment of spheroid growth dynamics.

3.3.16 BA/PA and 5-FU Combinatorial Treatment of 3D Spheroids

Cells were initially seeded at optimal density in a 200 µL volume per well within low-attachment 96-well, PS, U-bottom CELLSTAR microplates and allowed to proliferate for a period of 3 days. On the third day, BA/PA concentrations of 5 and 10 mM, previously established as optimal, were introduced in a 100 µL volume into the designated wells. Following a 24-hour incubation period, increasing concentrations of 5-FU, also previously

established by Tia Tidwell (82), were administered to the respective wells and allowed to exert their effects for an additional 24 hours. The layout of the plate is illustrated in **figure 3.8**.

1	2	3	4	5	6	7	8	9	10	11	12
PBS	PBS	PBS	PBS	PBS	PBS	PBS	PBS	PBS	PBS	PBS	PBS
PBS	Blank	Negative control	BA/PA	0.25 µg/mL 5-FU	16.0 µg/mL 5-FU	BA/PA + 0.25 µg/mL	BA/PA + 0.5 µg/mL	BA/PA + 1.0 µg/mL	BA/PA + 4.0 µg/mL	BA/PA + 16.0 µg/mL	PBS
PBS	Blank	Negative control	BA/PA	0.25 µg/mL 5-FU	16.0 µg/mL 5-FU	BA/PA + 0.25 µg/mL	BA/PA + 0.5 µg/mL	BA/PA + 1.0 µg/mL	BA/PA + 4.0 µg/mL	BA/PA + 16.0 µg/mL	PBS
PBS	Blank	Negative control	BA/PA	0.25 µg/mL 5-FU	16.0 µg/mL 5-FU	BA/PA + 0.25 µg/mL	BA/PA + 0.5 µg/mL	BA/PA + 1.0 µg/mL	BA/PA + 4.0 µg/mL	BA/PA + 16.0 µg/mL	PBS
PBS	Blank	Negative control	BA/PA	0.25 µg/mL 5-FU	16.0 µg/mL 5-FU	BA/PA + 0.25 µg/mL	BA/PA + 0.5 µg/mL	BA/PA + 1.0 µg/mL	BA/PA + 4.0 µg/mL	BA/PA + 16.0 µg/mL	PBS
PBS	Blank	Negative control	BA/PA	0.25 µg/mL 5-FU	16.0 µg/mL 5-FU	BA/PA + 0.25 µg/mL	BA/PA + 0.5 µg/mL	BA/PA + 1.0 µg/mL	BA/PA + 4.0 µg/mL	BA/PA + 16.0 µg/mL	PBS
PBS	Blank	Negative control	BA/PA	0.25 µg/mL 5-FU	16.0 µg/mL 5-FU	BA/PA + 0.25 µg/mL	BA/PA + 0.5 µg/mL	BA/PA + 1.0 µg/mL	BA/PA + 4.0 µg/mL	BA/PA + 16.0 µg/mL	PBS
PBS	PBS	PBS	PBS	PBS	PBS	PBS	PBS	PBS	PBS	PBS	PBS

Figure 3.8 Spheroid plate layout with concentrations for the combination treatment of 5 mM BA and 10 mM PA +increasing concentrations of 5-FU (0.25 ug/mL to 16.0 ug/mL).

Subsequently, Calcein AM and PI staining was performed according to the protocol outlined in subsection 3.4.14. Following staining, fluorescence measurements were taken at ex/em 485/530 nm and 535/610 nm for Calcein AM and PI, respectively. Fluorescent imaging was conducted before proceeding to data analysis.

3.4 Data Analysis

3.4.1 Normalization of absorbance/fluorescence raw data

To ensure the accuracy and reliability of the results obtained from both the CCK-8 and fluorescence staining assays, a normalization step was implemented. This step aimed to account for any potential variability and background noise in the absorbance readings.

The absorbance raw data underwent correction by normalizing to an untreated control group, establishing a baseline for comparison across different experimental conditions. The normalization formula used is depicted in **equation 3.4**:

Equation 3.4

$$Normalized\ replicate = \frac{Raw\ absorbance\ value}{Mean\ untreated\ control} * 100\%$$

This equation allowed the calculation of the normalized values for each replicate, expressed as a percentage relative to the untreated control group. This percentage representation allowed for a standardized comparison of the treatment effects on cell viability across multiple experimental conditions. Furthermore, the mean normalized value and standard deviation (SD) were computed for each experimental group to assess the central tendency and variability of the data, respectively.

3.4.2 Seahorse Cell Mito Stress Test

Following the Seahorse XF Cell Mito Stress Test, data analysis was conducted. This analysis involved assessing several parameters derived from the Seahorse XF assay, including basal respiration, proton leak, spare respiratory capacity, and ATP-production coupled respiration. The data obtained were plotted as OCR over time in minutes. These curves allowed for the visualization of the cellular response to increasing concentrations of FCCP.
Basal respiration is the mean OCR value before the addition of any modulator injections. Proton leak is the mean OCR value after the oligomycin injection, which inhibits ATP synthase. Spare respiratory capacity is calculated by subtracting the mean basal respiration from the maximal respiration. Lastly, ATP-production coupled respiration is calculated by subtracting the proton leak from the basal respiration. These parameters provide valuable insights into mitochondrial function and cellular bioenergetics.

3.4.3 Dixon´s Q-test

Dixon´s Q-test has been used to identify possible outliers in a data set (equation 3.5)

Equation 3.5

$$Q_n = \frac{(x_a - x_b)}{R}$$

Where:

R: range of all data points

Xa: suspected outlying value

Xb: data point value closest to xa

The Q statistic is further compared to a critical value from Dixon´s Q-test table at a 90% confidence interval. If the value of Q exceeds the critical value, the suspected value is considered an outlier.

Table 3.9 Dixon´s Q-test table critical values at a 90% confidence interval.

N= number of biological replicates, Q=critical value

n	3	4	5	6	7	8	9	10
Q	0.94	0.76	0.64	0.56	0.51	0.47	0.44	0.41

4. Results

4.1 CCK-8 Cell Density Optimalisation

To determine the optimal cell density for the CCK-8 treatment assays in this study, the mean CCK-8 absorbance value at 450 nm is plotted against its corresponding cell density number which yields an increasing line graph as shown in the following figures.

For the HCT116 cell line (**figure 4.1**), the absorbance increases to approximately 10,000 cells before it reaches a plateau.

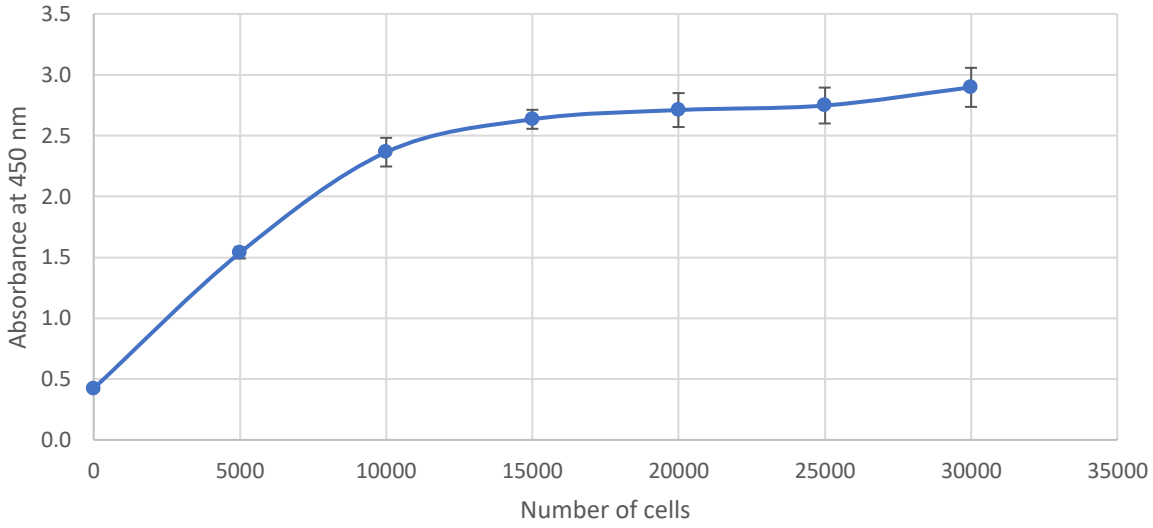

Figure 4.1 HCT116 CCK-8 Cell Density Optimalisation.

Absorbance values from the CCK-8 assay with increasing cell densities measured at 450 nm against cell density for cell line HCT116. Mean of N = 4 biological replicates, Error bars = Std. Dev. Accompanying data is listed in Appendix B.

For the SW948 cell line, the absorbance increases to approximately 5,000 cells before its plateau (**figure 4.2**).

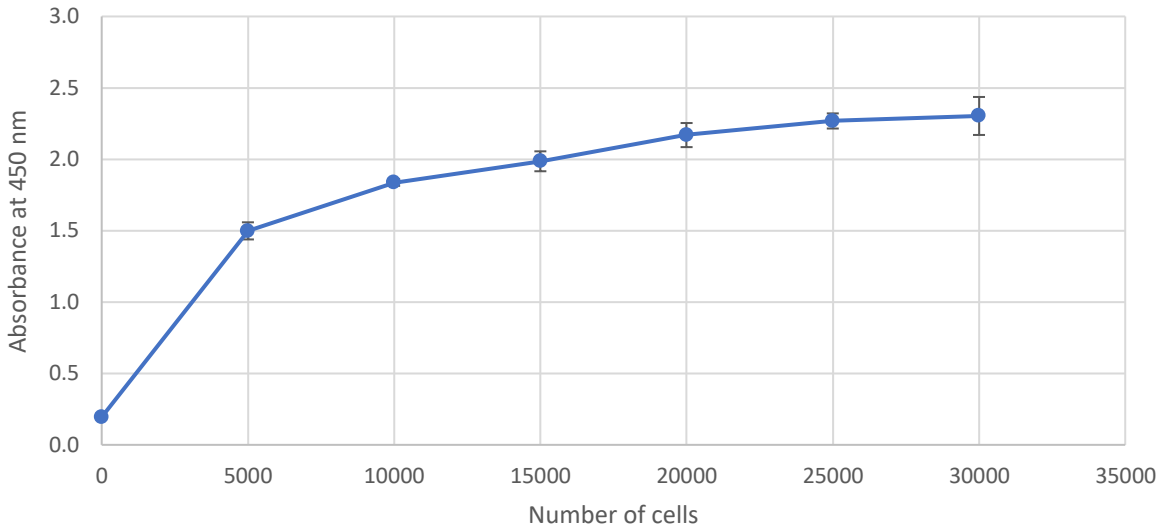

Figure 4.2 SW948 CCK-8 Cell Density Optimalisation.

Absorbance values from the CCK-8 assay with increasing cell densities measured at 450 nm against cell density for cell line SW948. Mean of N = 4 biological replicates, Error bars = Std. Dev. Accompanying data is listed in Appendix B.

4.2 BA and PA Treatments Affect Cell Proliferation in CRC

In this study, the impact of glucose deprivation on three distinct colorectal cancer cell lines—HCT116, SW948, and Caco-2—was systematically investigated over an extended period. The experimental design involved subjecting the cell lines to two distinct concentrations of glucose, 0,5- and 5,0 mM, before exposing the cells to increasing singular treatments of BA and PA for 48 hours. The accompanied data are represented in Appendix B.

4.2.1 BA Causes Dose Dependent Responses in Cell Proliferation

Exposure to increasing concentrations of BA resulted in a decreasing trend in absorbance values for both glucose concentrations tested in HCT116 cells (**figure 4.3**). The replicate mean of cells grown in to 0.5 mM glucose exhibited a faster decrease compared to those grown in to 5.0 mM glucose as the BA concentration increased.

At the 1.0 mM BA concentration, there was an initial increase in absorbance values for cells exposed to 0.5 mM glucose, followed by a subsequent decline. However, the higher SD observed in the 0.5 mM glucose group suggests greater variability within the data. For the 5.0 mM group, there is a slight linear decline in viability with increasing BA concentration.

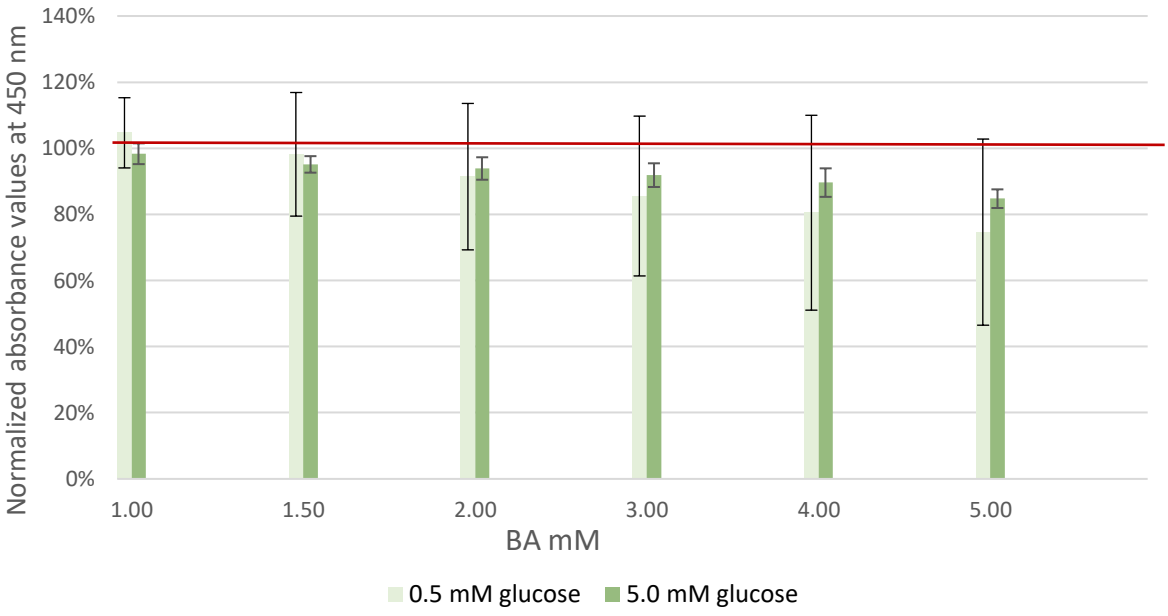

Figure 4.3 HCT116 BA treatments after 48H.

Normalized absorbance values from the CCK-8 assay measured at 450 nm for cell line HCT116 in physiological glucose or glucose deprived medium after a 48H exposure treatment of various concentrations of BA. The 100% reference line in the figures corresponds to the mean value observed in the untreated control group. Mean of N = 6 biological replicates, Error bars = Std. Dev. Accompanying data is listed in Appendix C.

The trends observed for the SW948 cell line exposed to singular treatments of BA (**figure 4.4**) exhibited similarities to those observed for the HCT116 cell line. For both glucose concentrations (0.5 mM and 5.0 mM), the absorbance values tended to be higher in the 0.5 mM group compared to the 5.0 mM group. Additionally, a clear decrease in viability was evident with increasing BA concentration for both glucose groups. However, unlike the HCT116 cell line, there was no initial increase in absorbance observed at the lowest treatment concentrations for the SW948 cell line. Instead, the decrease in absorbance increased substantially with higher BA concentrations, particularly evident in the 5.0 mM glucose group. The most effective treatment was observed with 5 mM BA for the 5.0 mM glucose group, with absorbance values reaching only 24%.

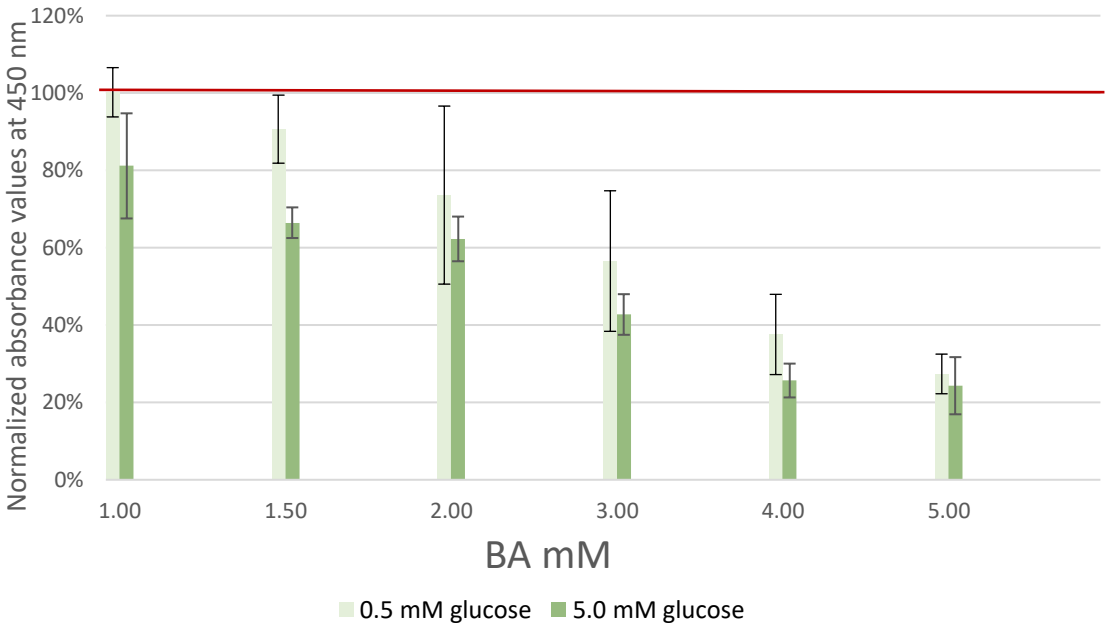

Figure 4.4 SW948 BA treatments after 48H.

Normalized absorbance values from the CCK-8 assay measured at 450 nm for cell line SW948 in physiological glucose or glucose deprived medium after a 48H exposure treatment of various concentrations of BA. The 100% reference line in the figures corresponds to the mean value observed in the untreated control group. Mean of N = 6 biological replicates, Error bars = Std. Dev. Accompanying data is listed in Appendix C.

The response of Caco-2 cells to BA treatments after 48 hours (**figure 4.5**) exhibited distinct characteristics compared to the HCT116 and SW948 cell lines. Notably, for the 0.5 mM glucose group, there was an increase in viability observed after BA exposure, consistent across all concentrations tested. This increase in viability was particularly pronounced, with

the highest viability observed at 122% for both 1.0 mM and 2.0 mM BA concentrations. Even at the highest BA concentration of 5.0 mM, viability remained relatively high at 108%.
For the 5.0 mM glucose group, there was a contrast to the glucose-starved group. The lowest concentration of BA resulted in a notable decrease in cell viability, sinking to 76%, with a further decline with increasing BA concentration in this growth condition.

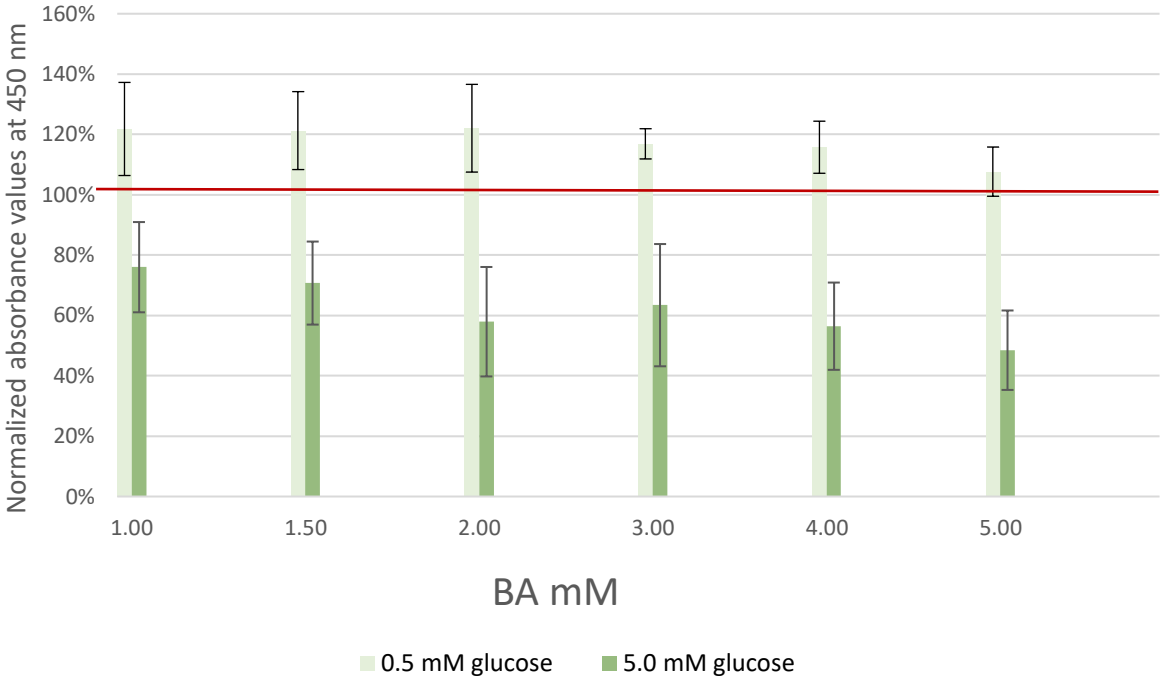

Figure 4.5 Caco-2 BA treatments after 48H.

Normalized absorbance values from the CCK-8 assay measured at 450 nm for cell line Caco-2 in physiological glucose or glucose deprived medium after a 48H exposure treatment of various concentrations of BA. The 100% reference line in the figures corresponds to the mean value observed in the untreated control group. Mean of N = 6 biological replicates, Error bars = Std. Dev. Accompanying data is listed in Appendix C.

4.2.2 PA Causes Dose Dependent Responses in Cell Proliferation

In the singular treatment of HCT116 cells with PA (**figure 4.6**), a clear increase in absorbance was observed for the 0.5 mM glucose concentration at 5 mM PA. However, as the PA concentration increased further, there was a subsequent decrease in absorbance. Similarly, for the 5.0 mM glucose group, increasing PA concentration led to a decrease in absorbance. Overall, the absorbance values for the 0.5 mM glucose group tended to be slightly higher than those for the 5.0 mM glucose group across all PA concentrations tested. Notably, the most effective treatment, as evidenced by the lowest absorbance values and presumably the highest cytotoxicity, was observed with 50 mM PA for the 5.0 mM glucose group.

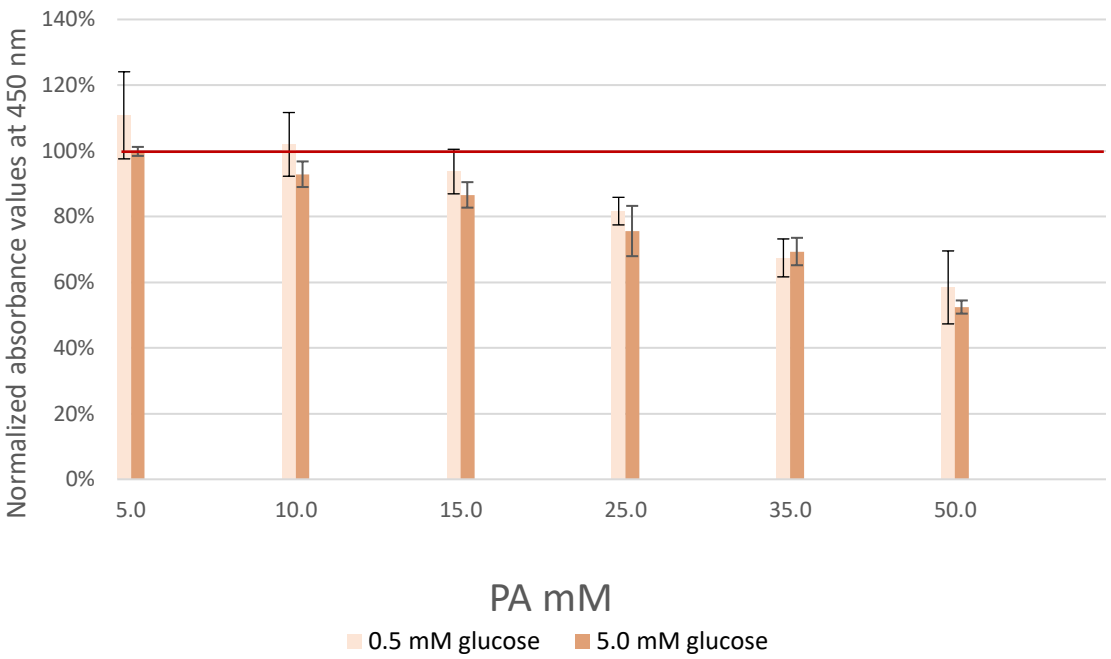

Figure 4.6 HCT116 PA treatments after 48H.

Normalized absorbance values from the CCK-8 assay measured at 450 nm for cell line HCT116 in physiological glucose or glucose deprived medium after a 48H exposure treatment of various concentrations of PA. The 100% reference line in the figures corresponds to the mean value observed in the untreated control group. Mean of N = 6 biological replicates, Error bars = Std. Dev. Accompanying data is listed in Appendix C.

The response of SW948 cells to singular treatments of PA for 48 hours (**figure 4.7**) exhibited trends similar to those observed for BA treatments, with a clear decrease in viability observed with higher PA concentrations for both glucose groups (0.5 mM and 5.0 mM).
Consistent with the BA treatments, the 0.5 mM glucose group demonstrated higher viability compared to the 5.0 mM glucose group across all treatment concentrations. However, unlike the HCT116 cell line, there was no observable increase in viability at the lowest concentration of PA for the SW948 cell line. It is noteworthy that while there was no apparent increase in viability at the lowest PA concentration, the variability observed in the data for the 0.5 mM glucose group at 5 mM PA might suggest otherwise.
Similar to the BA treatments, the most effective treatment was observed for the 5.0 mM glucose group at 50 mM PA, with viability reaching only 18%.

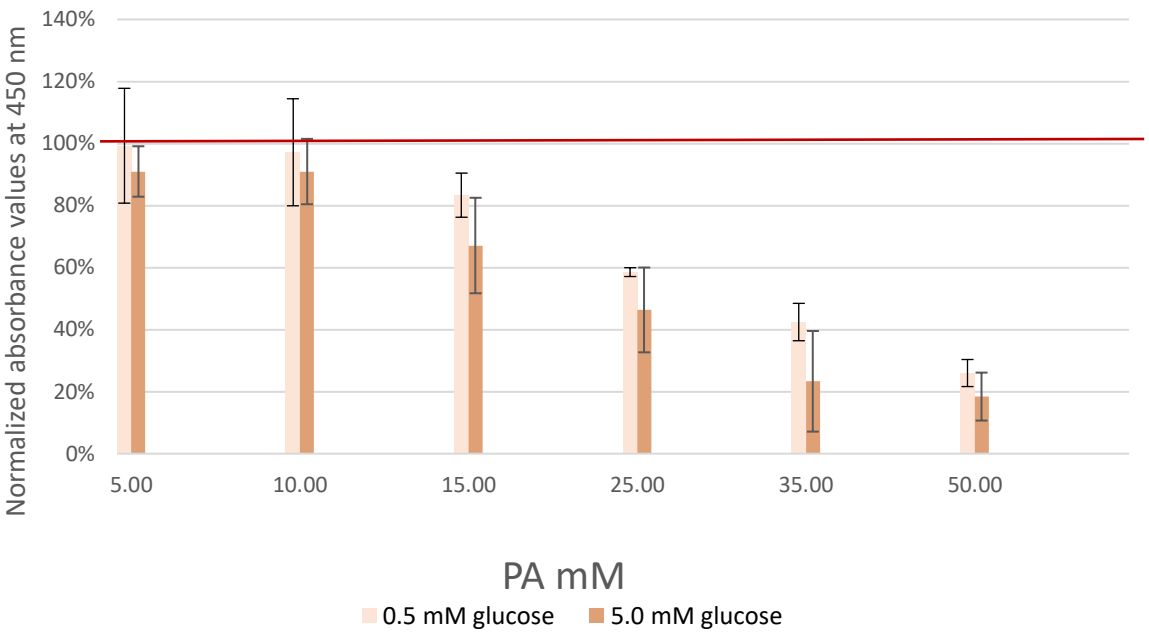

Figure 4.7 SW948 PA treatments after 48H.

Normalized absorbance values from the CCK-8 assay measured at 450 nm for cell line SW948 in physiological glucose or glucose deprived medium after a 48H exposure treatment of various concentrations of PA. The 100% reference line in the figures corresponds to the mean value observed in the untreated control group. Mean of N = 6 biological replicates, Error bars = Std. Dev. Accompanying data is listed in Appendix C.

The response of Caco-2 cells to PA treatments (**figure 4.8**) exhibited similar trends to those observed for the other cell lines, characterized by a decreasing trend in viability with increasing PA concentration for both glucose groups (0.5 mM and 5.0 mM). However, the decrease in viability for the 0.5 mM glucose group began at the 25 mM PA treatment, whereas lower concentrations showed little to no response relative to the control group. Additionally, there appeared to be a slight increase in viability observed in the lowest PA treatment for the 0.5 mM glucose group, with a mean value of 106%, but given the relatively high SD calculated at 16%, this increase may be coincidental.

Furthermore, a clear difference in viability was observed between the 0.5 mM and 5.0 mM glucose groups, with the 5.0 mM glucose group exhibiting a stronger reaction to PA treatment and consequently lower viability compared to the 0.5 mM glucose group.

The most significant effect of PA treatment for Caco-2 cells was observed in the 5.0 mM glucose group at the highest treatment concentration of 50 mM, where the mean viability was only 23%.

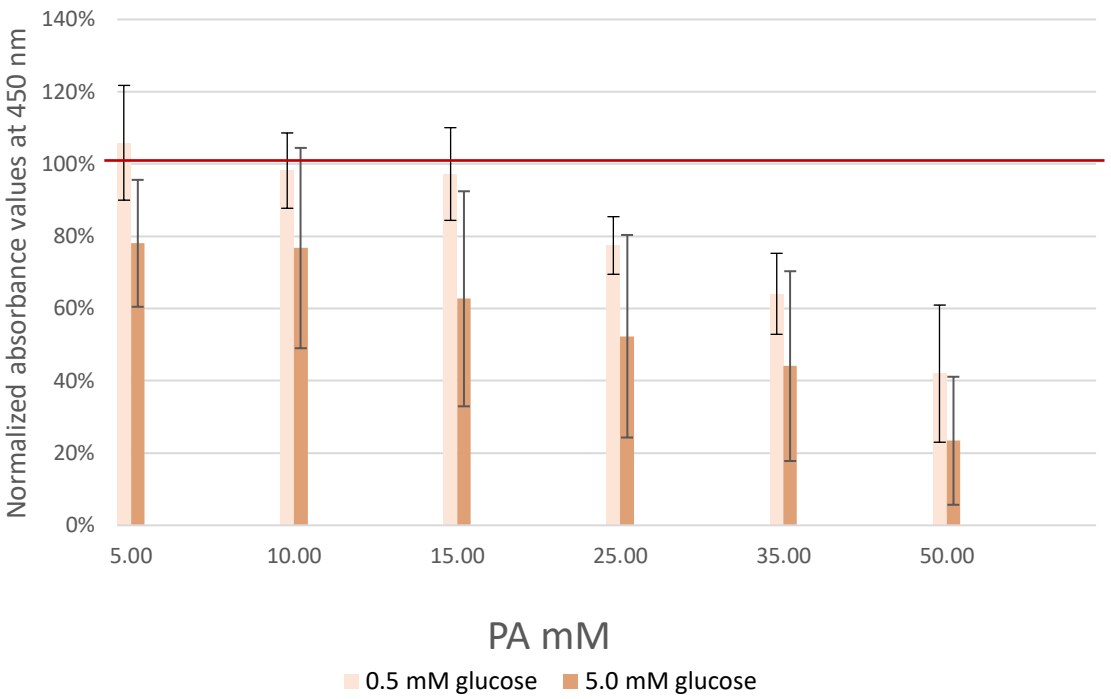

Figure 4.8 Caco-2 PA treatments after 48H.

Normalized absorbance values from the CCK-8 assay measured at 450 nm for cell line Caco-2 in physiological glucose or glucose deprived medium after a 48H exposure treatment of various concentrations of PA. The 100% reference line in the figures corresponds to the mean value observed in the untreated control group. Mean of N = 6 biological replicates, Error bars = Std. Dev. Accompanying data is listed in Appendix C.

4.4 Seahorse XF Cell Mito Stress Test FCCP Titration and Cell Density Optimalisation

Prior to conducting the Seahorse XF Cell Mito stress test treatment experiment, it was imperative to perform FCCP titration and optimal cell density determination. This preliminary step is crucial for ensuring accurate and reliable assessment of mitochondrial function and cellular bioenergetics using the Seahorse XF Analyzer.

For the HCT116 cell line, 0.5 μM FCCP had previously been established as optimal concentration in our group, thus only cell density needed to be established for this cell line. **Figure 4.9** illustrates the normalized OCR values over time for three different cell densities: 15,000 cells per well, 25,000 cells per well, and 35,000 cells per well. The graph includes distinct indicators representing the injection events of various modulators during the experiment.

At a cell density of 15K per well, the OCR response remains relatively stable throughout the experiment, showing consistent responsiveness to the injected modulators. In contrast, the 25K cell density exhibits the highest OCR response among all tested densities. Following the injection of modulators, the OCR increases substantially after the FCCP injection, indicating robust mitochondrial respiration. However, it is noteworthy that while maximal respiration surpasses the baseline level, there is a subsequent decline in OCR after reaching a plateau. Conversely, the 30K cell density demonstrates minimal responsiveness to the injected modulators, with little to no discernible changes in OCR over the course of the experiment.

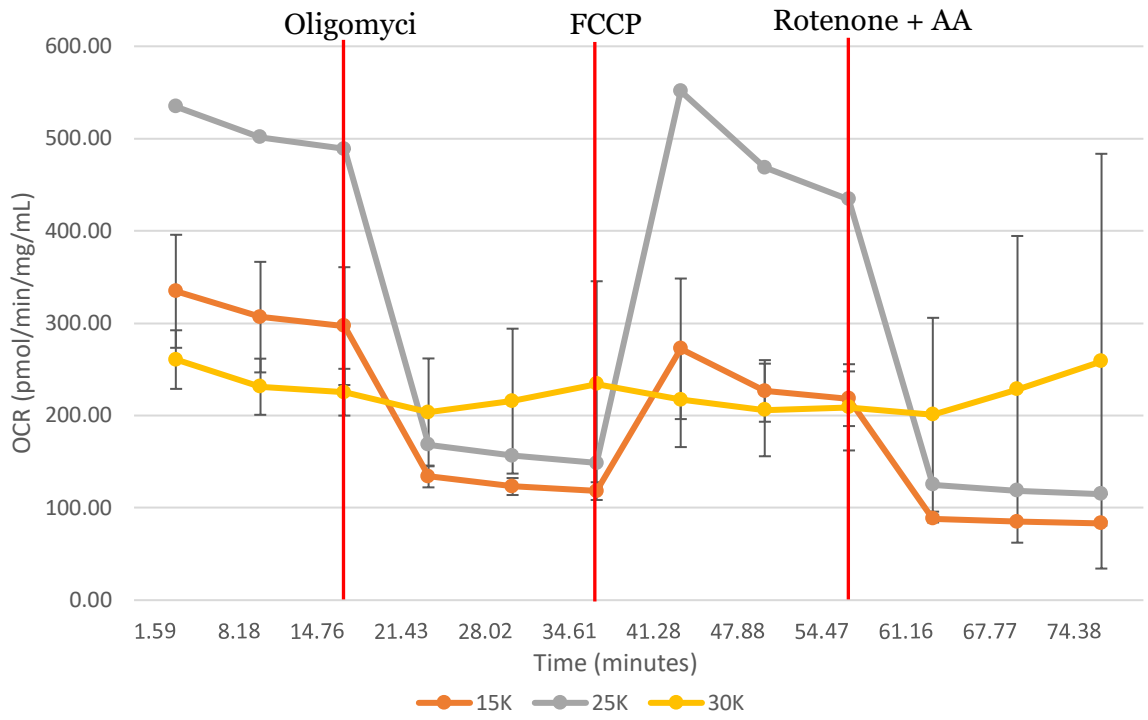

Figure 4.9 HCT116 optimal cell density determination of 15-, 25-, and 35K cell density

Seahorse XFp Cell Mito Stress Test Assay with 0,5 uM FCCP concentration. Y-axis shows normalized OCR (pmol/min/mg/mL) values. X-axis shows measured time events (minutes). Vertical red indicators represent modulator injections. Mean of up to N = 2 biological replicates. Error bars = Std. Dev. Accompanying data is listed in Appendix D.

In the Seahorse XF Cell Mito Stress Test performed on the SW948 cell line, both FCCP titration and cell density determination assays were simultaneously conducted using cell densities of 10,000 and 15,000 cells per well for all six FCCP concentrations. The normalized data obtained from these assays are presented in **Figure 4.10**.

Across all tested groups, the maximal respiration values were observed to be lower than the baseline, indicating that no spare respiratory capacity was present under the experimental conditions. When comparing the two cell densities, it was observed that the OCR values for the 10,000 cell per well density were consistently lower than those for the 15,000 cell per well density across all FCCP concentrations.

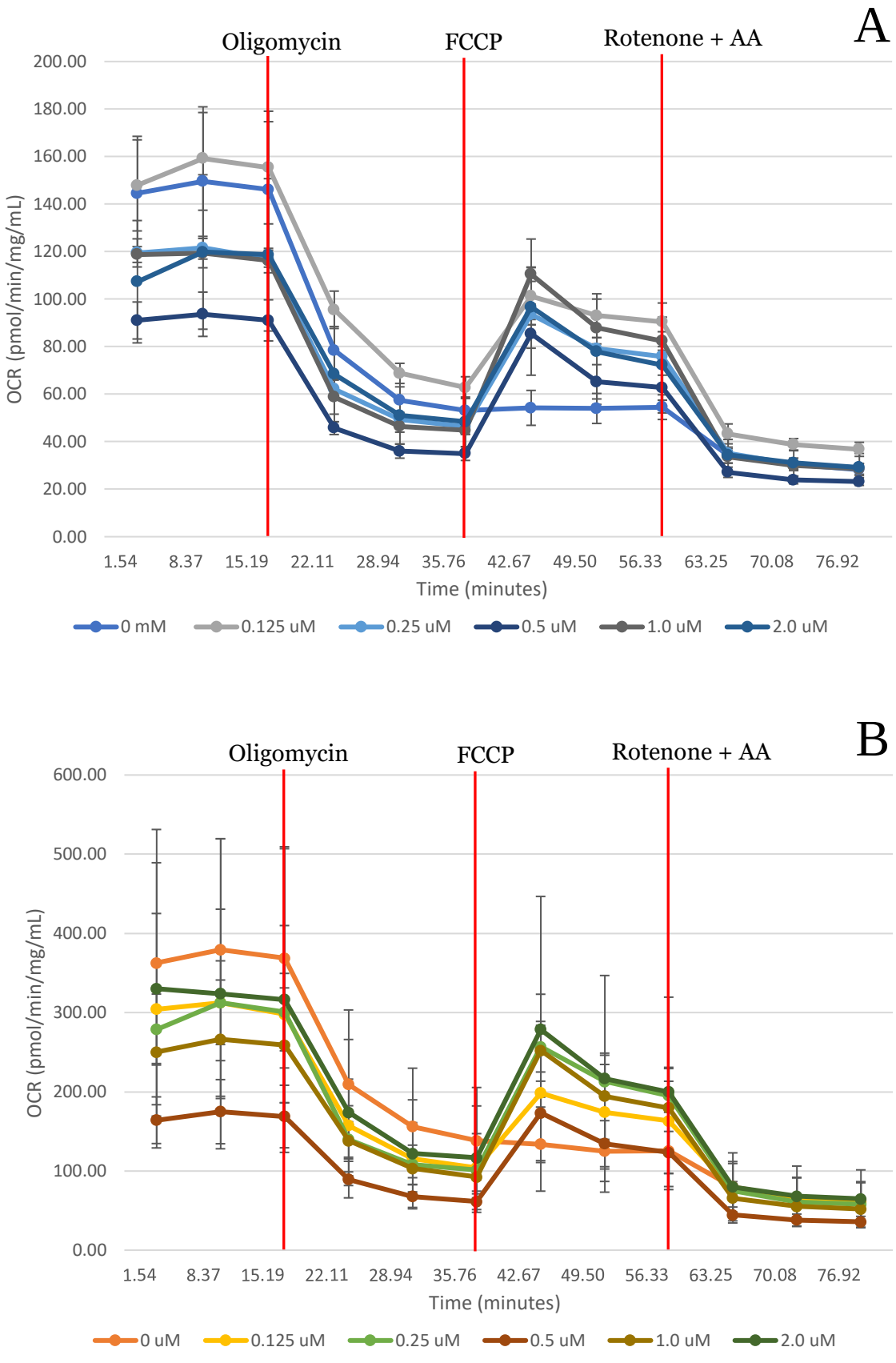

Figure 4.10 SW948 FCCP titration and optimal cell density determination

A) 10K, and B) 15K cell density Seahorse XF Cell Mito Stress Test Assay. Y-axis shows normalized OCR (pmol/min/mg/mL) values. X-axis shows measured time events (minutes). Vertical red indicators represent modulator injections. Mean of N = 3 biological replicates. Error bars = Std. Dev. Accompanying data is listed in Appendix D.

Only FCCP titration was conducted on the Caco-2 cell line since the optimal cell density at 5K had already been established previously in the research group. **Figure 4.11** shows the OCR value over time for all six FCCP concentrations.

The 0 uM FCCP concentration indicates the baseline OCR in the absence of FCCP-induced mitochondrial uncoupling. Across all FCCP concentrations, a relatively stable maximal respiration is observed after the FCCP injection. The FCCP concentration of 0.25 uM stands out with the highest OCR values throughout all measurements.

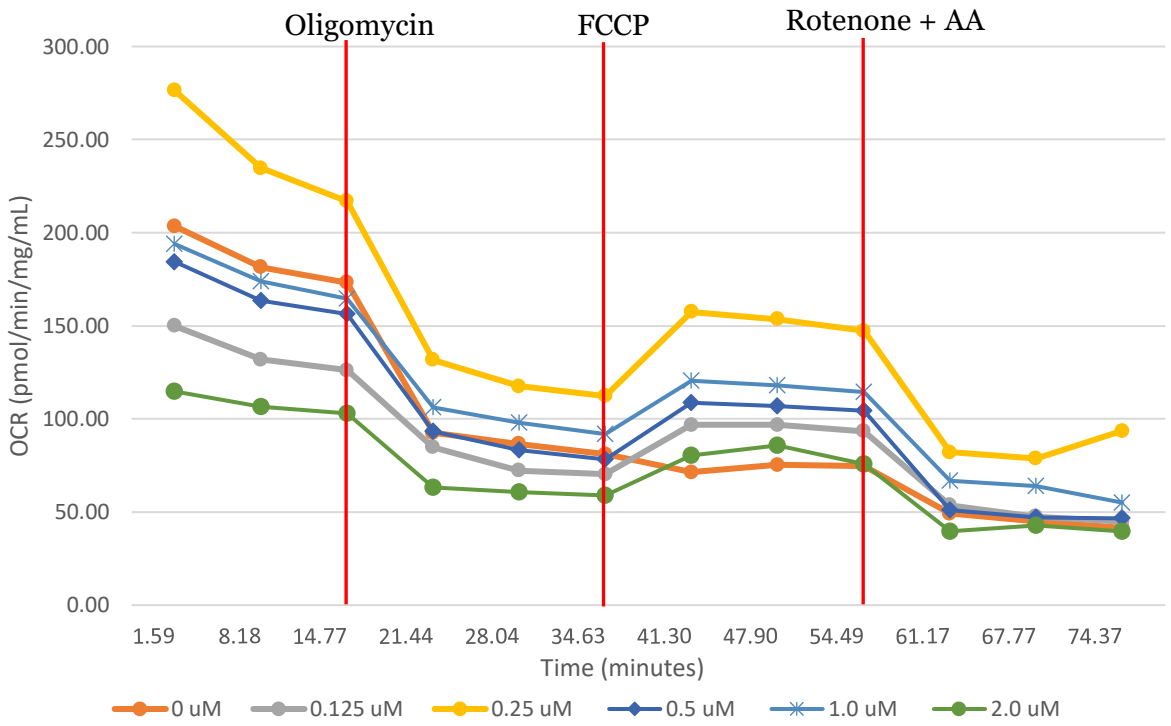

Figure 4.11 Caco-2 FCCP titration 5K cell density Seahorse XF Cell Mito Stress Test Assay.

Y-axis shows normalized OCR (pmol/min/mg/mL) values. X-axis shows measured time events (minutes). Vertical red indicators represent modulator injections. N = 1 biological replicate. Error bars = Std. Dev. Accompanying data is listed in Appendix D.

4.5 BA and PA Affect Mitochondrial Respiration

The Seahorse Cell XF Mito Stress Test was performed to evaluate the mitochondrial function and metabolic activity of CRC lines following treatment with varying concentrations of BA and PA. This assay provides insights into several key parameters of mitochondrial respiration, including basal respiration, proton leak, spare respiratory capacity, and ATP-production coupled respiration. These parameters are essential for understanding how BA and PA impact the bioenergetic profiles of CRC cells and their potential role in modifying cellular metabolism.

Figure 4.12 shows the normalized OCR (pmol/min/mg/mL) values per minute for each singular BA treatments on the HCT116 cell line throughout the full procedure of the assay. The untreated control exhibited minimal response at maximal respiration, indicating basal OCR levels. In contrast, all BA treatments resulted in an increase in maximal respiration compared to the untreated control. Specifically, 1.0 mM BA treatment led to an overall increase in OCR, while 1.5 mM BA treatment yielded the highest OCR values overall. However, as BA concentration increased beyond 1.5 mM, there was a subsequent decrease in OCR, with 5.0 mM BA treatment being the most effective in reducing OCR.

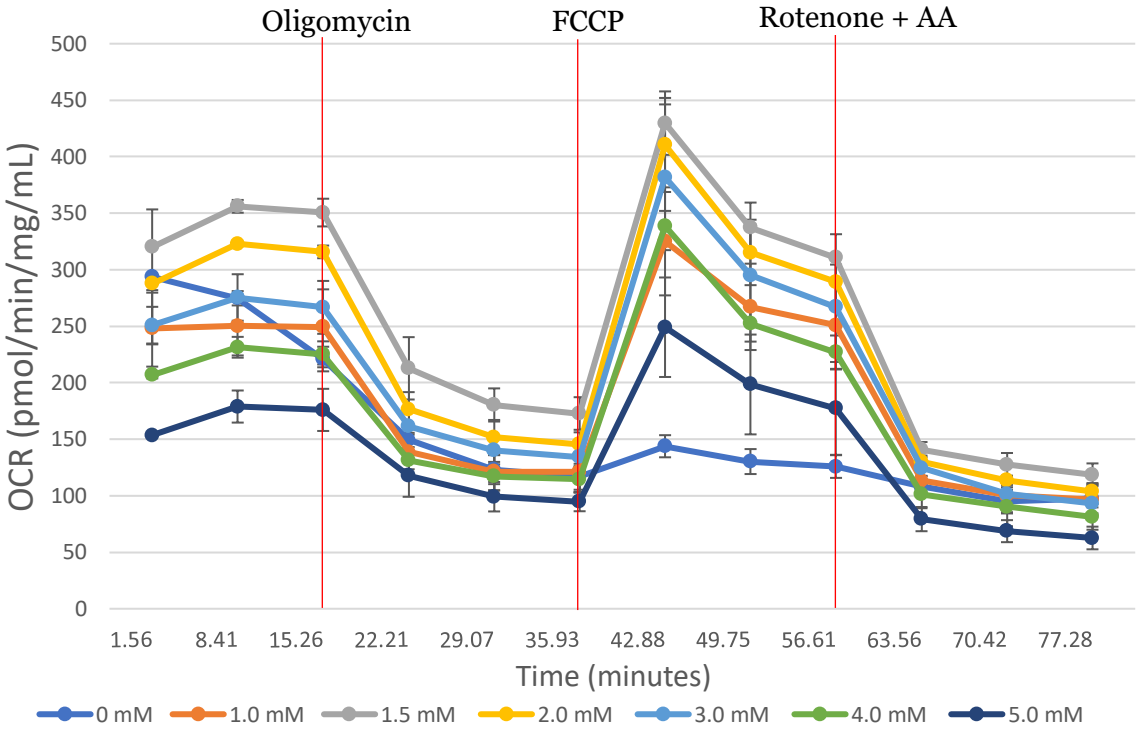

Figure 4.12 HCT116 Seahorse XF Cell Mito Stress Test Assay after 48H singular treatments of BA.

Y-axis shows normalized OCR (pmol/min/mg/mL) values. X-axis shows measured time events (minutes). N = 3 biological replicates. Error bars = Std. Dev. Accompanying data is listed in Appendix E.

For the SW948 cell line (**figure 4.14**), the untreated control stands as the highest overall OCR of all the BA treatments. Upon BA treatment, distinct responses in OCR were observed. Treatment with 1.0 mM BA led to a significant decrease in OCR values compared to the untreated control, indicating a suppressive effect on mitochondrial respiration. Subsequent treatment with 1.5 mM BA resulted in an increase in OCR values, suggesting a potential stimulatory effect on mitochondrial activity. However, this increase was followed by a gradual decline in OCR. Notably, treatment with 5.0 mM BA exhibited OCR values similar to those observed with 1.0 mM BA, albeit with the lowest maximal respiration among all treatments.

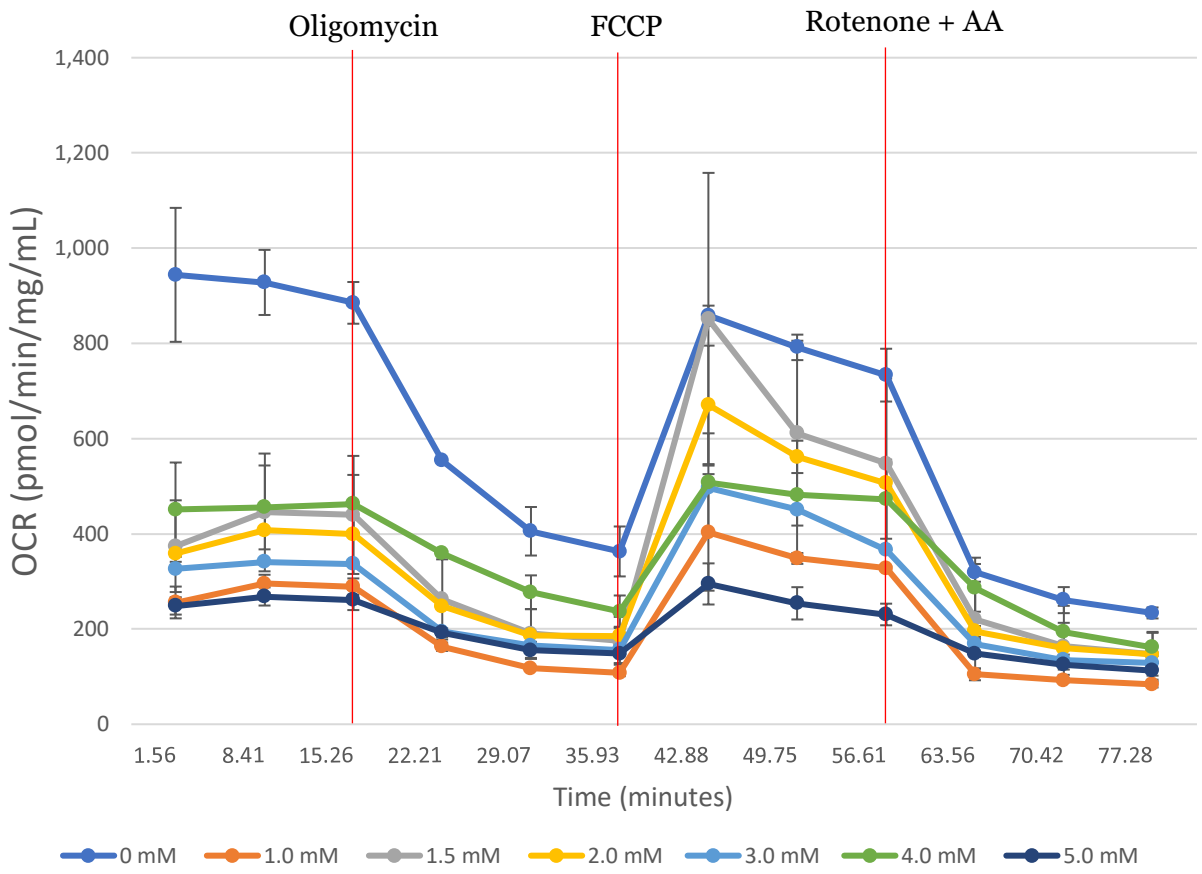

Figure 4.13 SW948 Seahorse XF Cell Mito Stress Test Assay after 48H singular treatments of BA.

Y-axis shows normalized OCR (pmol/min/mg/mL) values. X-axis shows measured time events (minutes). N = 3 biological replicates. Error bars = Std. Dev. Accompanying data is listed in Appendix E.

In the Seahorse Cell Mito Stress Test BA 48H treatments conducted on the Caco-2 cell line, a diverse range of responses to increasing concentrations of BA was observed. **Figure 4.16** depicts the normalized OCR values per minute for each singular BA treatment.
Distinct trends in OCR were observed with increasing BA treatment concentrations in Caco-2 cells. Treatment with 1.0 mM BA resulted in the highest OCR values among all concentrations tested, indicating a stimulatory effect on mitochondrial respiration. Subsequent treatments with 1.5 and 2.0 mM BA exhibited OCR values lower than those observed with 1.0 mM BA but still higher than the untreated control. In contrast, treatment with 3.0 mM BA led to the lowest overall OCR values. Interestingly, treatments with 4.0 and 5.0 mM BA resulted in increased OCR values compared to 3.0 mM BA treatment, with 5.0 mM BA treatment exhibiting the second-highest overall OCR.

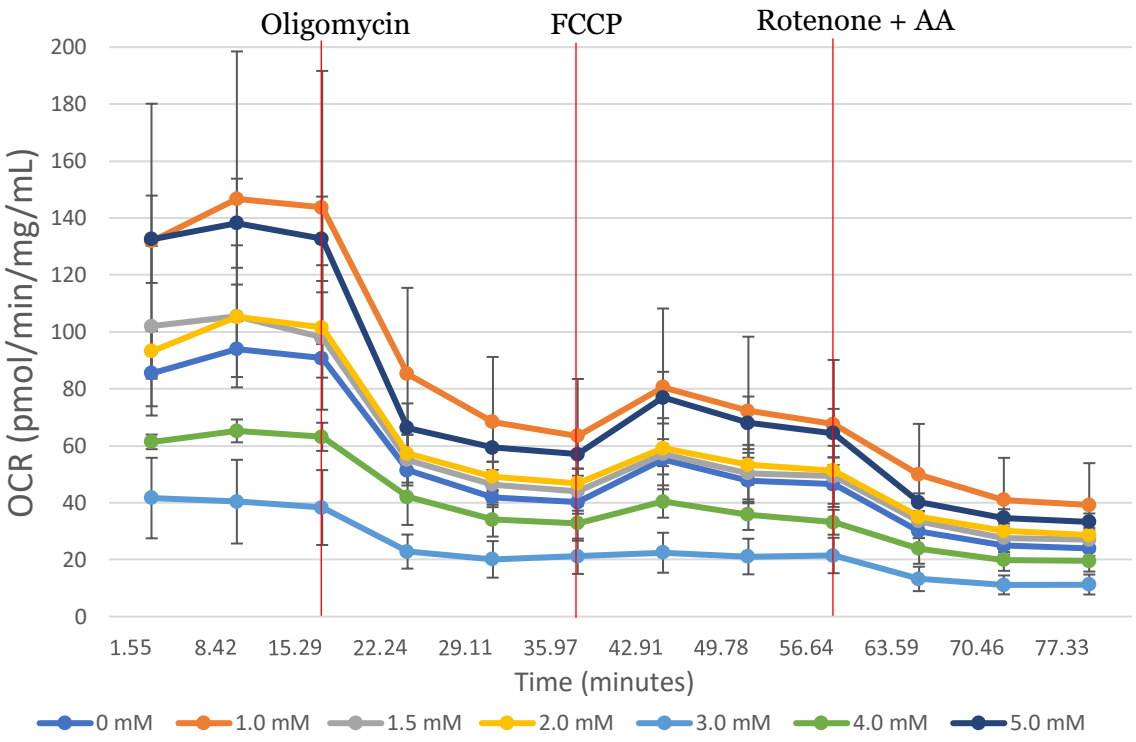

Figure 4.14 Caco-2 Seahorse XF Cell Mito Stress Test Assay after 48H singular treatments of BA.

Y-axis shows normalized OCR (pmol/min/mg/mL) values. X-axis shows measured time events (minutes). N = 3 biological replicates. Error bars = Std. Dev. Accompanying data is listed in Appendix E.

Figure 4.15 shows the basal respiration for the three cell lines HCT116, SW948, and Caco-2 with increasing BA concentration treatments. All the cell lines show an initial increase in basal respiration with increasing BA concentration before a drop. The OCR peak is variable among the cell lines. For HCT116, the peak is at 1.5 mM BA, for SW948 the peak besides the untreated control is at 3.0 mM BA albeit with the highest SD, and for Caco-2 the peak is at the lowest BA concentration of 1.0 mM.

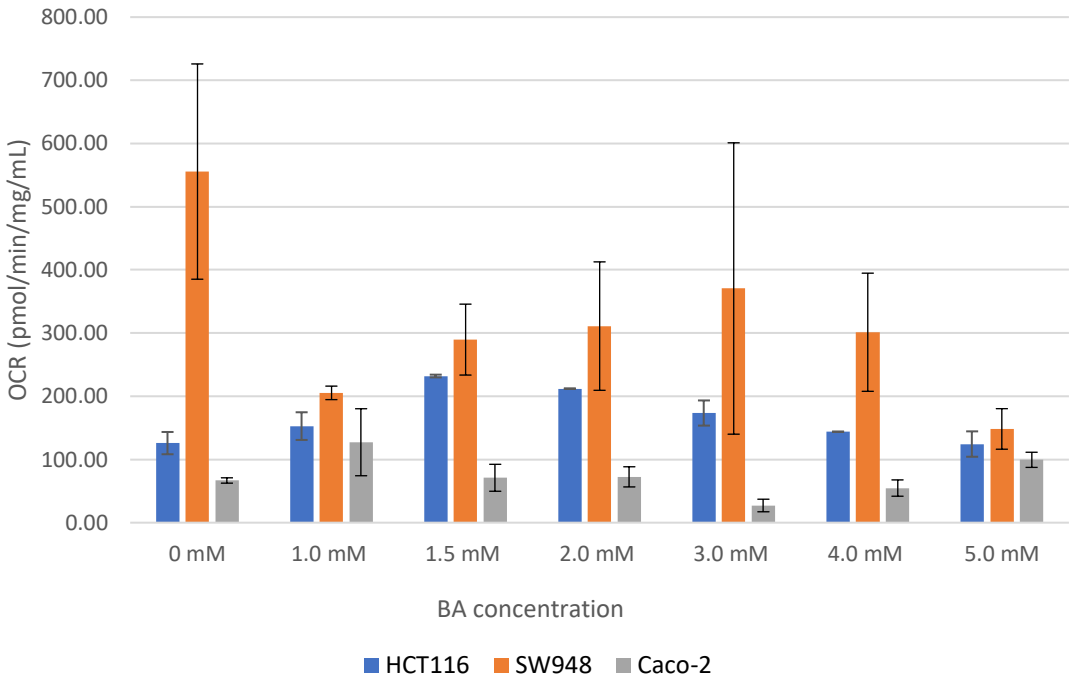

Figure 4.15 Basal respiration for cell lines HCT116, SW948, and Caco-2 with increasing butyrate (BA) concentrations. Y-axis shows normalized OCR (pmol/min/mg/mL) values. X-axis shows BA concentration. N = 3 biological replicates. Error bars = Std. Dev. Accompanying data is listed in Appendix E.

Figure 4.16 shows the proton leak for the three cell lines with increasing BA concentrations. Overall, all cell lines show an increase in proton leak at a certain concentration of BA. For the HCT116 cell line, all BA treatments show heightened OCR relative to the untreated control, peaking at 1.5 mM. For SW948, the OCR significantly decreases from the untreated control to the lowest BA treatment, although the proton leak increases with higher BA concentrations, peaking at 4.0 mM. Caco-2 has the lowest overall OCR among the three cell lines. The 1.0 mM BA treatment has the highest proton leak, including the untreated control. The lowest OCR is with the 3.0 mM BA treatment.

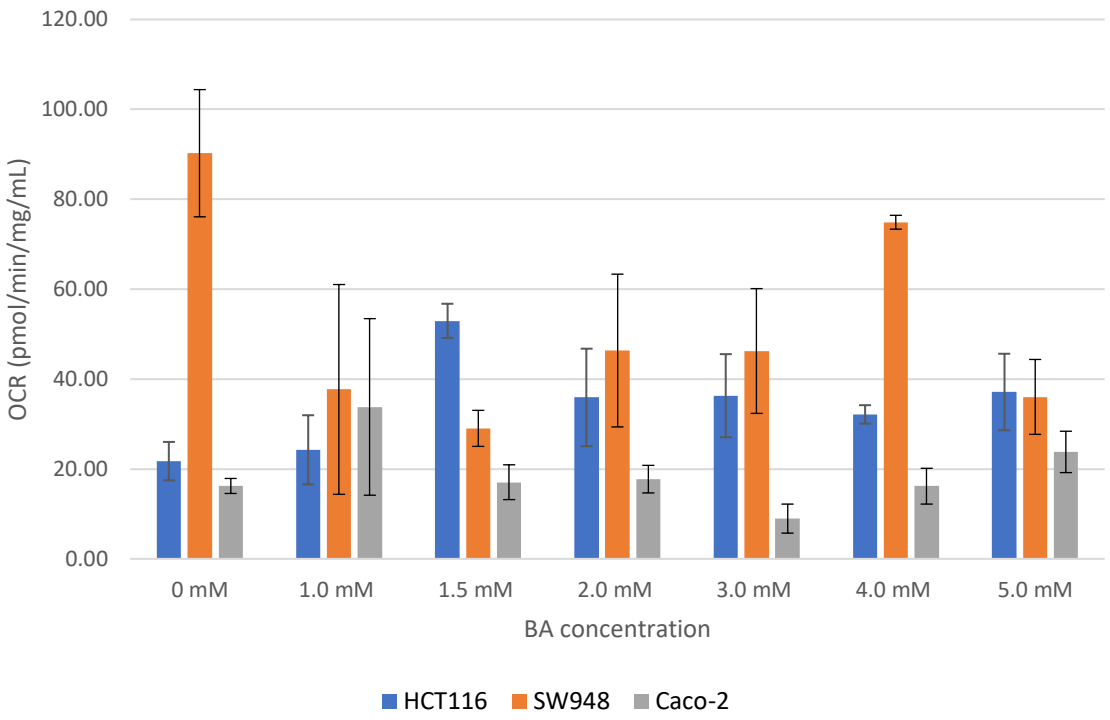

Figure 4.16 Proton leak for cell lines HCT116, SW948, and Caco-2 with increasing butyrate (BA) concentrations. Y-axis shows normalized OCR (pmol/min/mg/mL) values. X-axis shows BA concentration. N = 3 biological replicates. Error bars = Std. Dev. Accompanying data is listed in Appendix E.

Figure 4.17 shows the OCR measurements for spare respiratory capacity with increasing BA treatments for all three cell lines. HCT116 shows an absence of spare respiratory capacity for the untreated control, but BA treatments increase the OCR for all concentrations, peaking at 4.0 mM. For the SW948 cell line, the initial OCR at the untreated control is almost 0 before significantly increasing with low BA treatments, then gradually decreasing to almost 0 for the highest concentrations. Caco-2 do not exhibit any spare respiratory capacity for any of the treatments, including the untreated control.

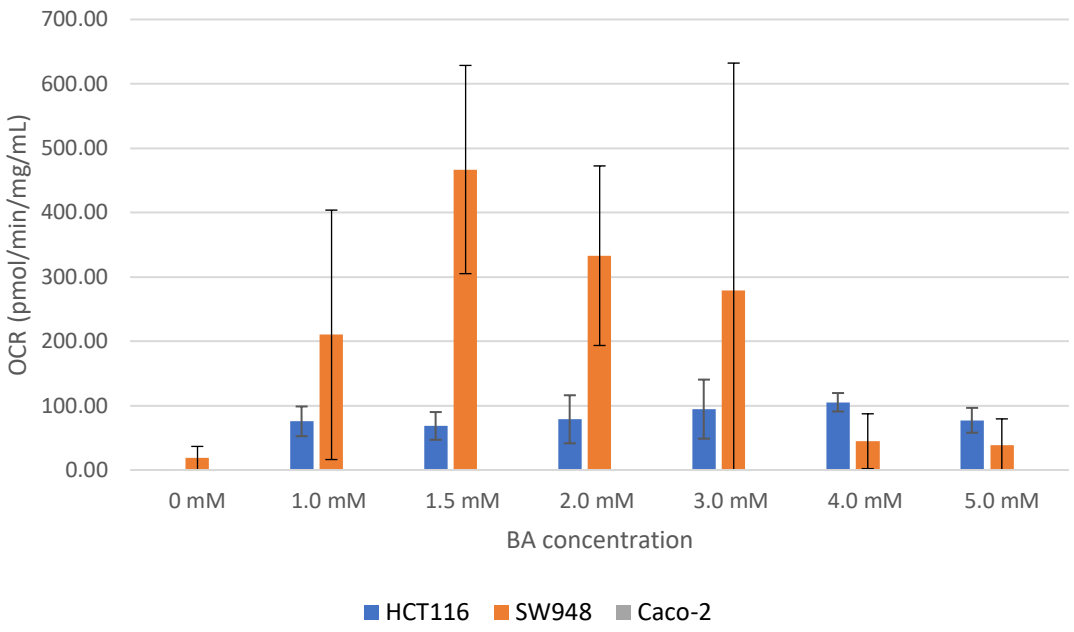

Figure 4.17 Spare respiratory capacity for cell lines HCT116, SW948, and Caco-2 with increasing butyrate (BA) concentrations.

Y-axis shows normalized OCR (pmol/min/mg/mL) values. X-axis shows BA concentration. N = 3 biological replicates. Error bars = Std. Dev. Accompanying data is listed in Appendix E.

Figure 4.18 shows the ATP-production linked respiration for all three cell lines. For the HCT116 cell line, BA slightly enhances ATP production at low concentrations, peaking at 1.5 mM BA. SW948 shows a significant decrease relative to the untreated control, with unstable values across the BA concentrations, although lowest at 5.0 mM BA. Caco-2 shows a peak at 1.0 mM BA before decreasing and then increasing again at the highest BA concentrations.

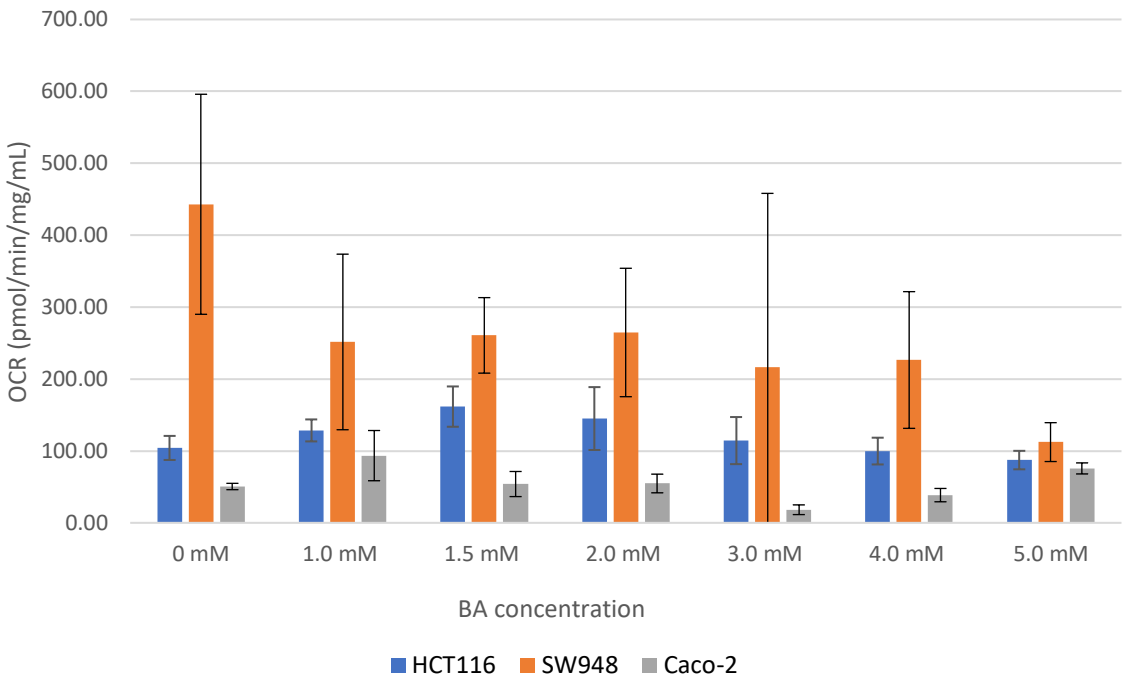

Figure 4.18 ATP production linked respiration for cell lines HCT116, SW948, and Caco-2 with increasing butyrate (BA) concentrations.

Y-axis shows normalized OCR (pmol/min/mg/mL) values. X-axis shows BA concentration. N = 3 biological replicates. Error bars = Std. Dev. Accompanying data is listed in Appendix E.

In the Seahorse Cell Mito Stress Test PA singular treatments conducted on the HCT116 cell line, similar trends in mitochondrial respiration were observed compared to the BA treatments. **Figure 4.19** illustrates the normalized OCR values per minute for each singular PA treatment.

Consistent with the BA treatments, low doses of PA at 5 and 10 mM led to an increase in OCR relative to the untreated control. This suggests that lower concentrations of PA may enhance mitochondrial respiration and metabolic activity in HCT116 cells, similar to the observed effects with BA. However, treatment with 15 mM PA resulted in a significant decrease in the overall OCR compared to lower doses, indicating a suppressive effect on mitochondrial respiration. Treatment with 25 mM PA led to an increase in OCR, with OCR values approaching those observed in the untreated control group.

In contrast, the highest PA treatment concentrations of 35 and 50 mM resulted in the lowest OCR values among all treatments, with 50 mM PA exhibiting the lowest OCR overall. Additionally, there was little to no response to the FCCP injection, indicating a lack of spare respiratory capacity and maximal respiration peak.

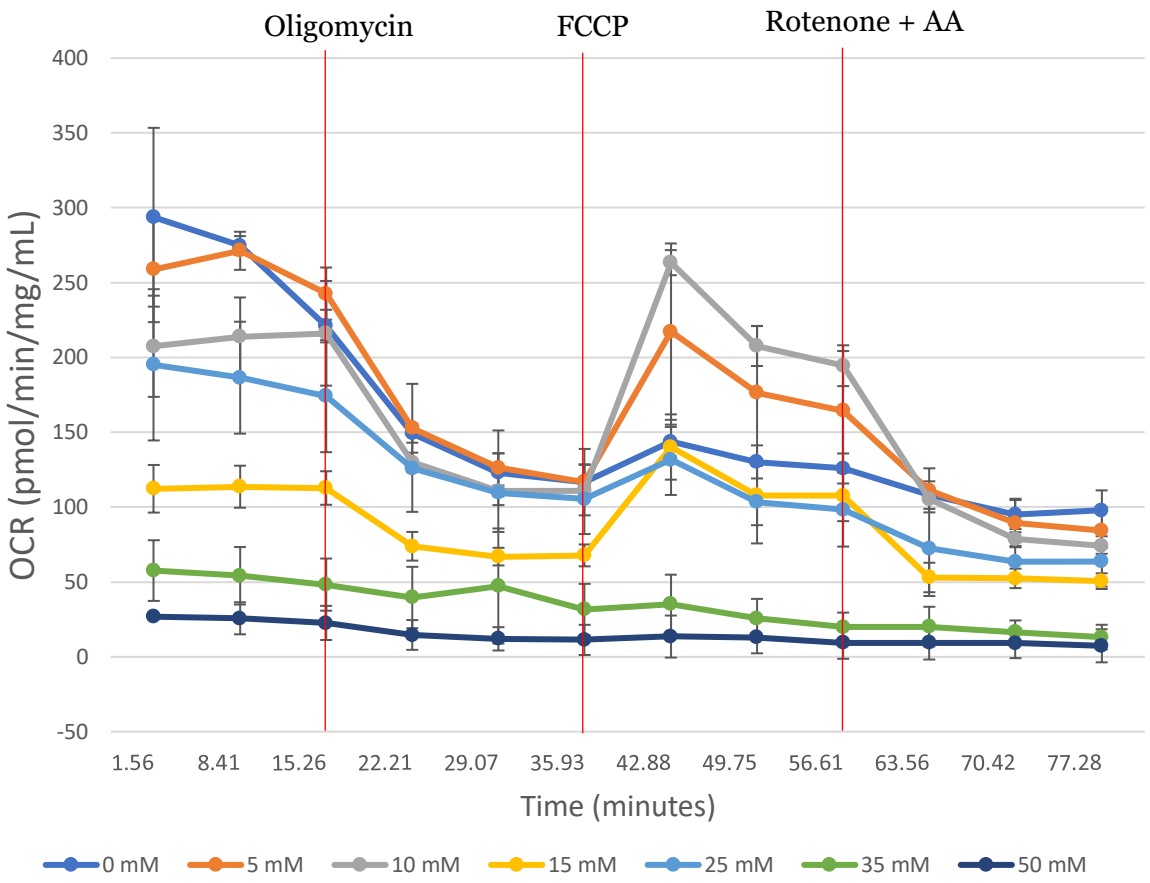

Figure 4.19 HCT116 Seahorse XF Cell Mito Stress Test Assay after 48H singular treatments of PA.

Y-axis shows normalized OCR (pmol/min/mg/mL) values. X-axis shows measured time events (minutes). N = 3 biological replicates. Error bars = Std. Dev. Accompanying data is listed in Appendix E.

In the Seahorse Cell Mito Stress Test PA singular treatments conducted on the SW948 cell line, notable trends in mitochondrial respiration were observed across all PA treatment concentrations. **Figure 4.20** illustrates the normalized OCR values per minute for each singular PA treatment. Contrary to the observed responses in the HCT116 cell line, all PA treatments in the SW948 cell line resulted in a profound decrease in OCR values relative to the untreated control. Even at lower doses, PA treatments led to a significant reduction in OCR values. The treatment with the highest PA concentrations of 35 and 50 mM resulted in the lowest OCR values among all treatments. There was little to no response to the injected modulators at these concentrations.

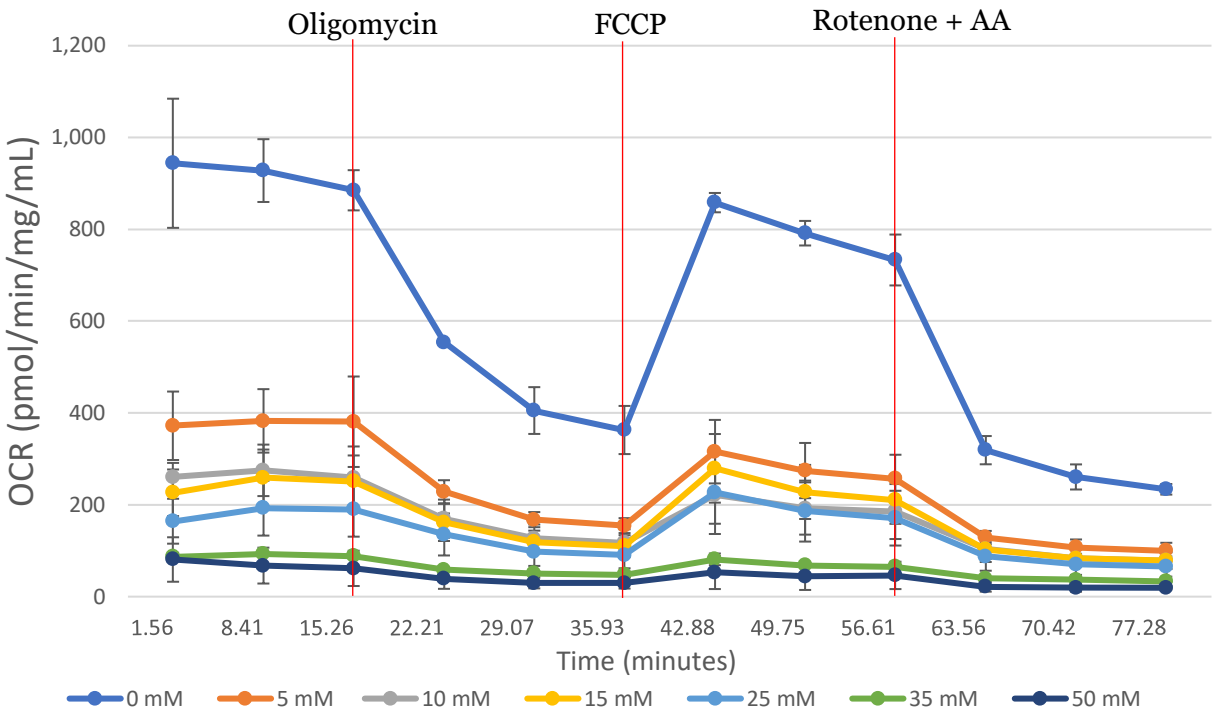

Figure 4.20 SW948 Seahorse XF Cell Mito Stress Test Assay after singular treatments of PA.

Y-axis shows normalized OCR (pmol/min/mg/mL) values. X-axis shows measured time events (minutes). N = 3 biological replicates. Error bars = Std. Dev. Accompanying data is listed in Appendix E.

In the Seahorse Cell Mito Stress Test PA singular treatments conducted on the Caco-2 cell line, consistent patterns in mitochondrial respiration were observed, resembling the responses seen in the SW948 cell line. **Figure 4.21** illustrates the OCR values per minute for each singular PA treatment.

Similar to the SW948 cell line, all PA treatments in the Caco-2 cell line resulted in an overall decrease in OCR values compared to the untreated control. Notably, treatment with 10 mM PA resulted in the second lowest OCR values among all treatments, indicating a substantial inhibition of mitochondrial respiration at this concentration. Treatments with 15- and 25 mM PA led to a transient increase in OCR values before subsequently declining at higher concentrations (35 and 50 mM). Consistent with the observations in the SW948 cell line, treatment with the highest PA concentration of 50 mM resulted in the lowest overall OCR values among all treatments, indicating a maximal suppression of mitochondrial respiration.

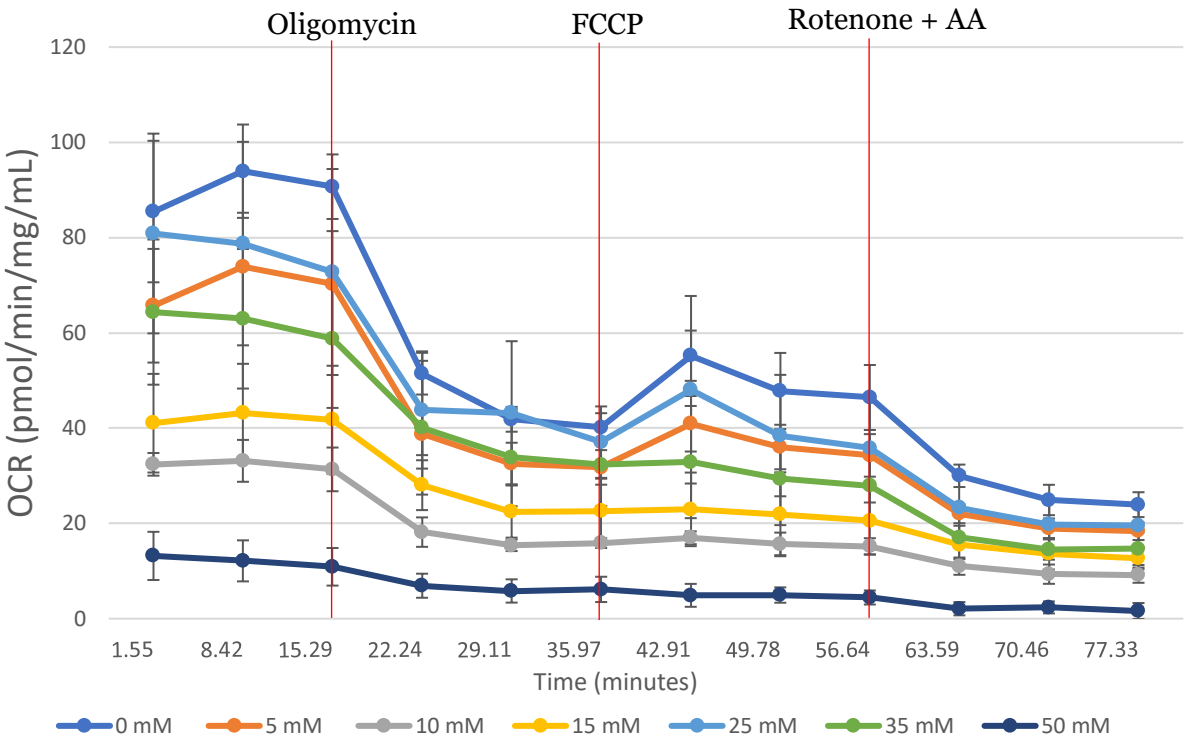

Figure 4.21 Caco-2 Seahorse XF Cell Mito Stress Test Assay after 48H singular treatments of PA.

Y-axis shows normalized OCR (pmol/min/mg/mL) values. X-axis shows measured time events (minutes). N = 3 biological replicates. Error bars = Std. Dev. Accompanying data is listed in Appendix E.

Figure 4.22 shows the basal respiration parameter for the PA treatments of all cell lines. HCT116 shows a biphasic response, peaking at 5 mM PA before decreasing and then further increasing at 25 mM. The highest basal respiration for SW948 is with the untreated control. PA treatments significantly lowers the OCR with a progressive decrease with increasing PA concentration. For Caco-2, increasing PA concentration decreases the OCR before a slight increase at the highest concentrations.

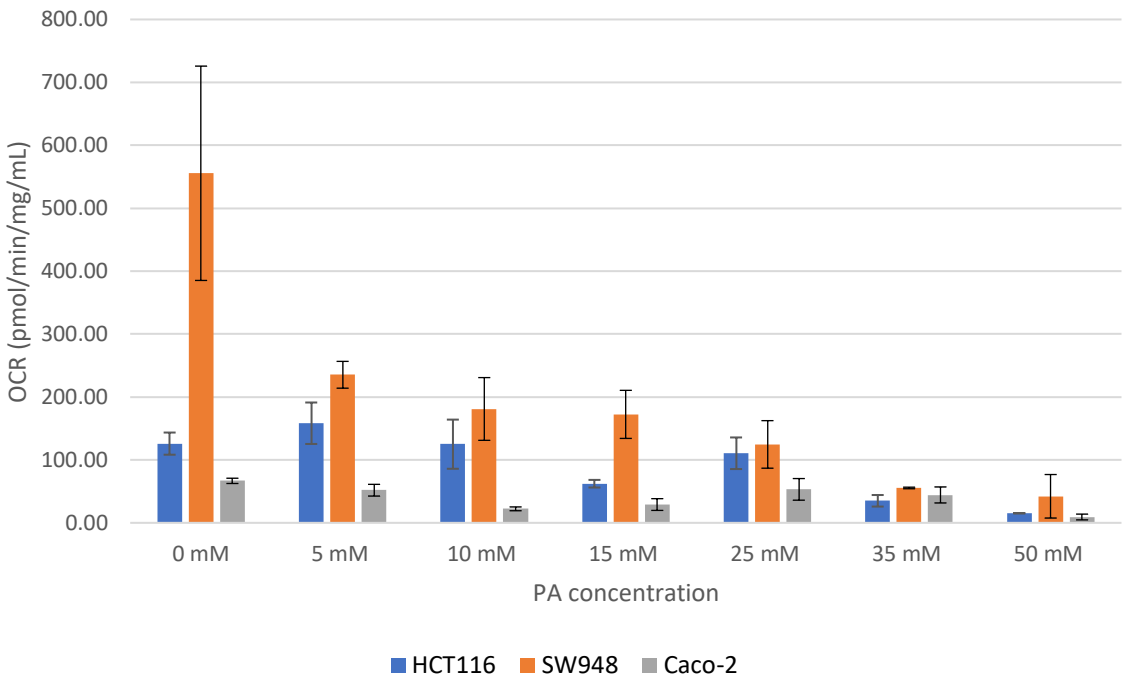

Figure 4.22 Basal respiration for cell lines HCT116, SW948, and Caco-2 with increasing propionate (PA) concentrations. Y-axis shows normalized OCR (pmol/min/mg/mL) values. X-axis shows BA concentration. N = 3 biological replicates. Error bars = Std. Dev. Accompanying data is listed in Appendix E.

Figure 4.23 shows the proton leak for the three cell lines under increasing PA treatments. HCT116 exhibits variable results with an initial increase in OCR for the lowest PA concentration. The proton leak decreases for the 10- and 15 mM treatment before increasing again at the 25 mM PA treatment. SW948 has a steady decrease with increasing PA concentration. For the Caco-2 cell line, the proton leak initially decreases from the untreated control to 10 mM PA. The OCR peaks at 25 mM before decreasing yet again. The lowest proton leak for all cell lines lies at the highest PA concentration, the 50 mM treatment.

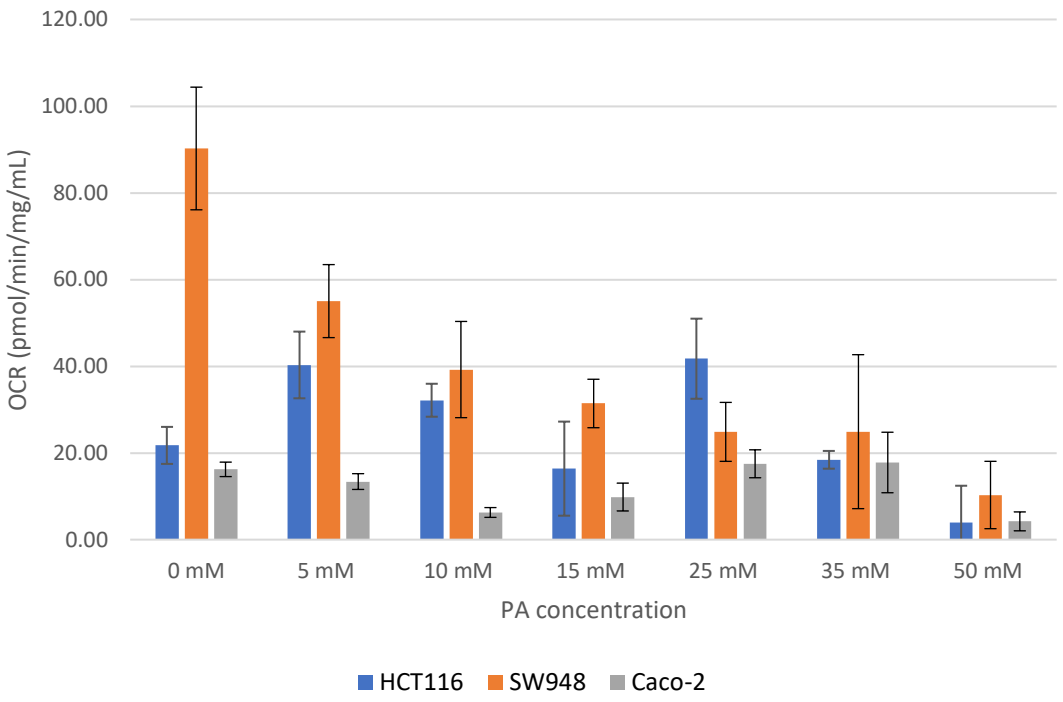

Figure 4.23 Proton leak for cell lines HCT116, SW948, and Caco-2 with increasing propionate (PA) concentrations. Y-axis shows normalized OCR (pmol/min/mg/mL) values. X-axis shows BA concentration. N = 3 biological replicates. Error bars = Std. Dev. Accompanying data is listed in Appendix E.

Figure 4.24 shows the spare respiratory capacity for all cell lines with increasing PA treatments. HCT116 only has OCR in the 5, 10, and 15 mM PA. SW948 has a slight spare respiratory capacity at the intreated control, but peaks at the 25 mM PA treatment. Like the BA treatments, Caco-2 shows no spare respiratory capacity for any of the treatments.

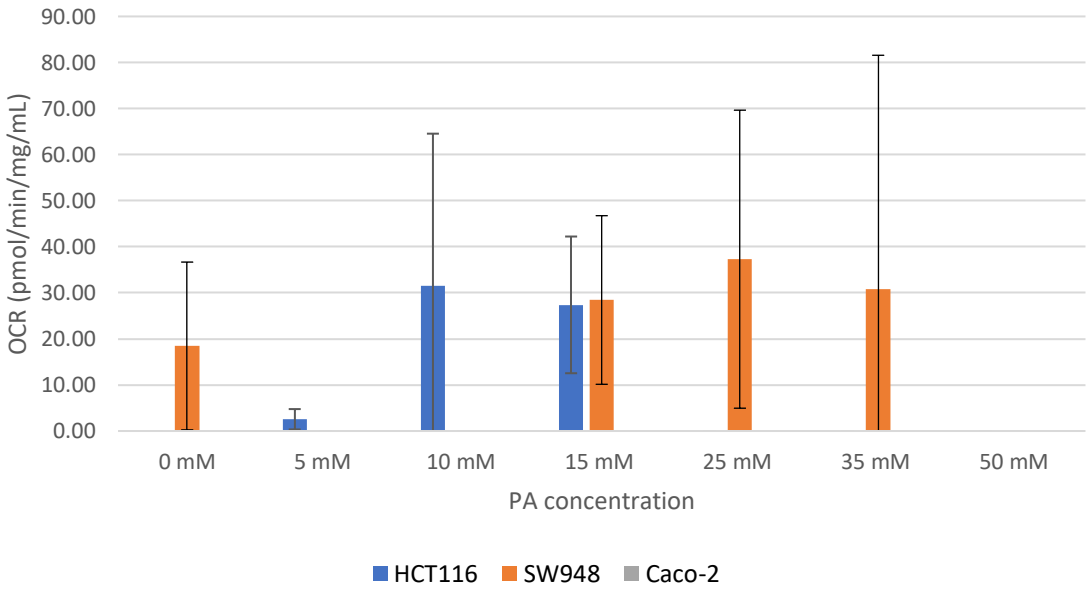

Figure 4.24 Spare respiratory capacity for cell lines HCT116, SW948, and Caco-2 with increasing propionate (PA) concentrations

Y-axis shows normalized OCR (pmol/min/mg/mL) values. X-axis shows BA concentration. N = 3 biological replicates. Error bars = Std. Dev. Accompanying data is listed in Appendix E.

Figure 4.25 shows the ATP production linked respiration for all cell lines with increasing PA treatments. HCT116 has a peak at the 5 mM PA treatment before gradually decreasing with increasing PA concentration. For both the SW948 and Caco-2 cell line, the highest OCR lies at the untreated control. Increasing PA concentration decreases the OCR. The lowest ATP production linked respiration for all cell lines is with the highest PA treatment.

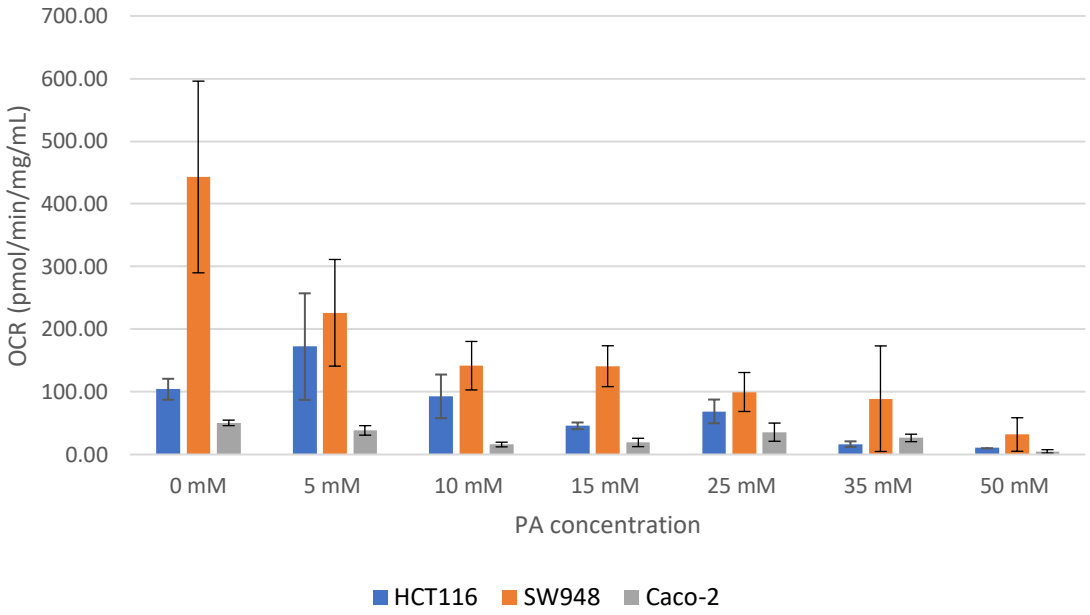

Figure 4.25 ATP production linked respiration for cell lines HCT116, SW948, and Caco-2 with increasing propionate (PA) concentrations

Y-axis shows normalized OCR (pmol/min/mg/mL) values. X-axis shows BA concentration. N = 3 biological replicates. Error bars = Std. Dev. Accompanying data is listed in Appendix E.

4.3 BA and PA Combinatorial Treatments Decrease Cell Viability Synergistically

To deepen the understanding of how BA and PA affect CRC cell viability, an expanded investigation was conducted using combinations of these SCFAs. This study also examined how these effects are modulated by glucose availability, reflecting different metabolic conditions. By exploring the interplay between BA, PA, and glucose levels, this assay aimed to uncover potential therapeutic strategies that exploit metabolic vulnerabilities in cancer cells. Additionally, this experiment aimed to determine the potential of BA and PA as a pretreatment to enhance the efficacy of 5-FU.

Figure 4.26 A and B depict the combinatorial efficacy of BA+PA treatments for the HCT116 cell line grown in both 0.5 mM and 5.0 mM glucose concentrations. At low concentrations of PA, increasing concentrations of BA appeared to have a more significant impact on cell viability. Conversely, BA seemed to have a diminished effect on higher concentrations of PA. The least effective combination for both glucose groups was observed with 5+1 BA+PA. However, the most effective treatment varied between the glucose groups. For the 0.5 mM glucose group, the combination of 50+3 BA+PA exhibited the highest efficacy. In contrast, for the 5.0 mM glucose group, all BA concentrations combined with 50 mM PA were the most effective.
It is noteworthy that the SD for both glucose groups was relatively high, reaching up to 21%. Overall, BA+PA treatments exerted a more pronounced effect on the glucose-starved group.

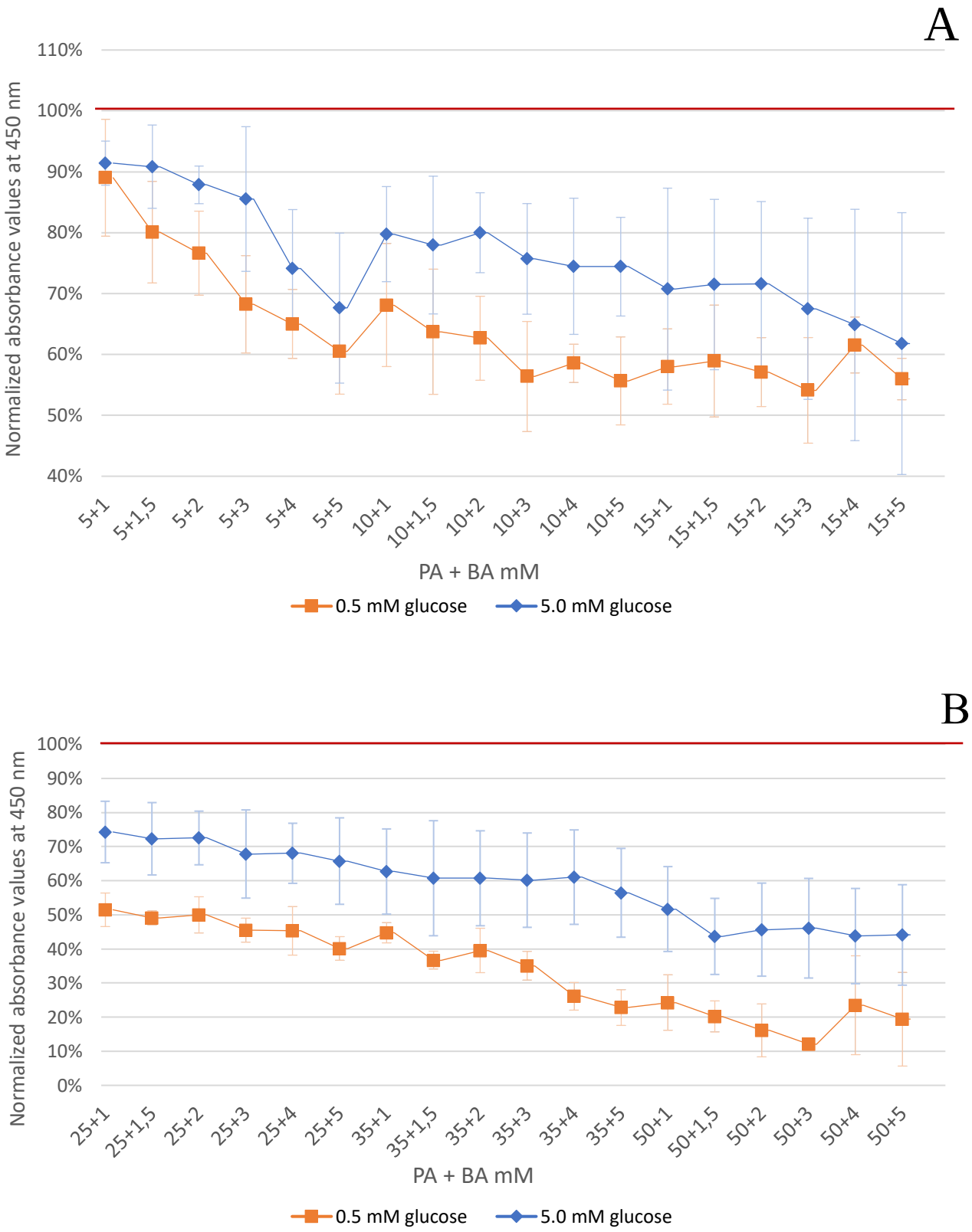

Figure 4.26 HCT116 combination treatment

Normalized absorbance values from the CCK-8 assay measured at 450 nm for cell line HCT116 in physiological glucose or glucose deprived medium after a 48H exposure treatment of increasing concentration of A) PA (5-15 mM) vs BA (1-5 mM)

and B) PA (25-50 mM) vs BA (1-5 mM). The 100% reference line in the figures corresponds to the mean value observed in the untreated control group. Mean of N = 6 biological replicates, Error bars = Std. Dev. Accompanying data is listed in Appendix F.

The response of the SW948 cell line to BA+PA combination treatments mirrors the trends observed in the HCT116 cell line, although with some notable differences. **Figure 4.27** A and B illustrate how increasing concentrations of BA exerted a higher impact on cell viability, particularly evident for lower PA concentrations.

The efficacy of BA+PA combination treatments varied depending on the glucose concentration. For the first three PA concentrations (5, 10, and 15 mM), the combination treatment demonstrated a more pronounced effect on the 5.0 mM glucose group compared to the 0.5 mM glucose group. However, this trend shifted with the 25 mM PA combinations and above, indicating a complex interplay between BA, PA, and glucose availability in modulating treatment efficacy. For the 0.5 mM glucose group, the 50+4 and 50+5 BA+PA combinations yielded the highest efficacy, resulting in viabilities of 14% and 20%, respectively. In contrast, for the 5.0 mM glucose group, the most effective treatment was 50+4 BA+PA, with a viability of 20%.

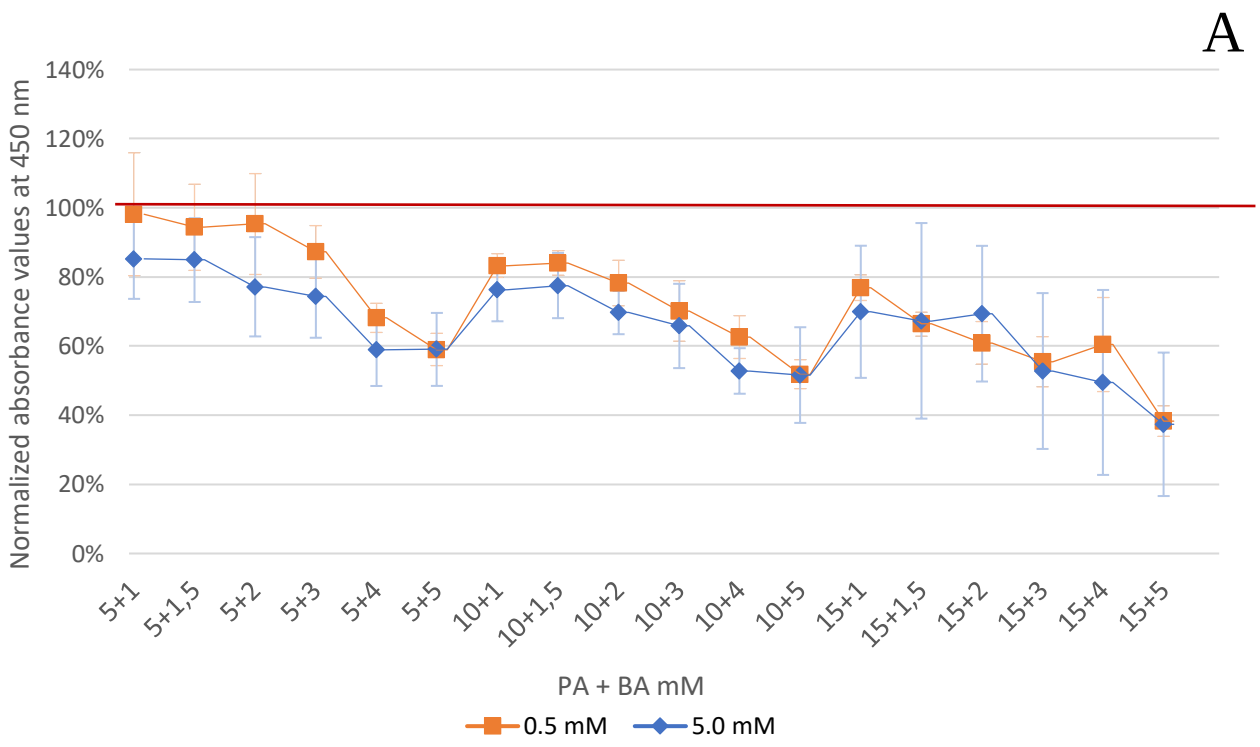

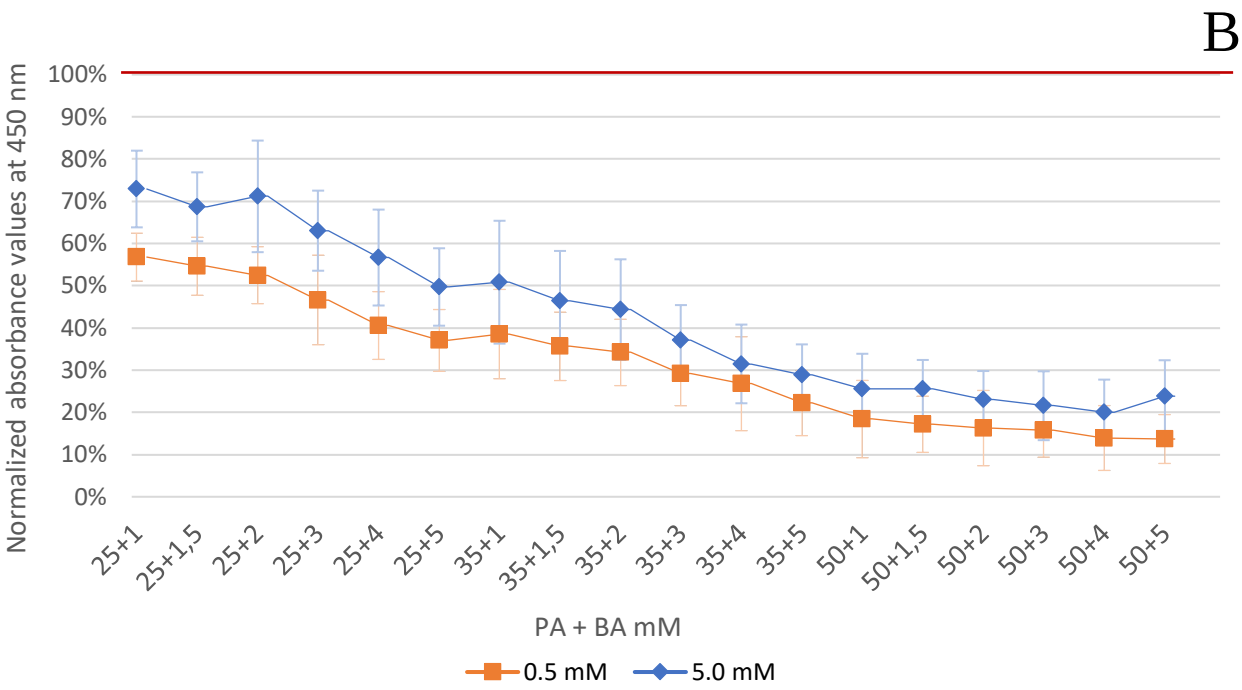

Figure 4.27 SW948 combination treatment

Normalized absorbance values from the CCK-8 assay measured at 450 nm for cell line SW948 in physiological glucose or glucose deprived medium after a 48H exposure treatment of increasing concentration of A) PA (5-15 mM) vs BA (1-5 mM) and B) PA (25-50 mM) vs BA (1-5 mM). The 100% reference line in the figures corresponds to the mean value observed in the untreated control group. Mean of N = 6 biological replicates, Error bars = Std. Dev. Accompanying data is listed in Appendix F.

The response of the Caco-2 cell line to BA+PA combination treatments (**figure 4.28**) revealed a more uneven trend, characterized by high and unstable SD.

Despite the high variability, notable treatment responses were observed. For the 0.5 mM glucose group, the 50+4 BA+PA treatment exhibited a substantial increase in viability compared to the closest treatments. Importantly, this increase was consistent across both plates, encompassing all six replicates. The most effective treatments for the Caco-2 cell line were identified as 50+3 PA+BA, resulting in a viability of 9% for the 0.5 mM glucose group, and 50+4 PA+BA, yielding a viability of 31% for the 5.0 mM glucose group. An overall higher efficacy of the combination treatment was observed for the 0.5 mM glucose group compared to the 5.0 mM glucose group.

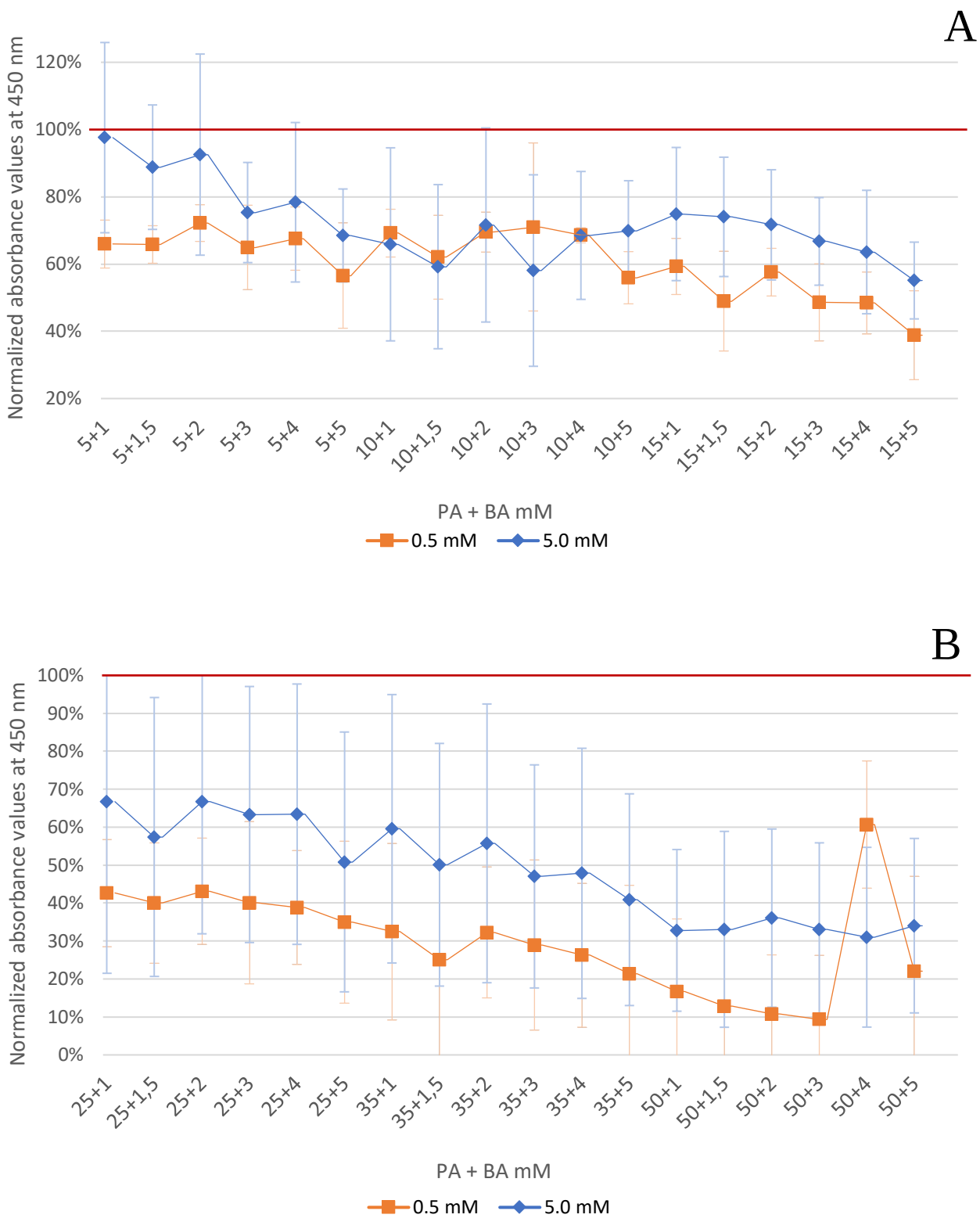

Figure 4.28 Caco-2 combination treatment

Normalized absorbance values from the CCK-8 assay measured at 450 nm for cell line Caco-2 in physiological glucose or glucose deprived medium after a 48H exposure treatment of increasing concentration of A) PA (5-15 mM) vs BA (1-5 mM) and B) PA (25-50 mM) vs BA (1-5 mM). The 100% reference line in the figures corresponds to the mean value observed in

the untreated control group. Mean of N = 6 biological replicates, Error bars = Std. Dev. Accompanying data is listed in Appendix F.

4.6 3D Spheroid Density Optimization

To better mimic the 3D form of a growing tumor, cancer spheroids were made from the same CRC cell lines. To find the optimal cell density number to conduct further experiments, a cell density evaluation was performed.

The following figures show transmitted images and the average diameter of the spheroids, measured in micrometers, at both day 4 and day 8 of culture conducted for the three distinct cell lines: HCT116, SW948, and Caco-2. These data provide insights into the growth dynamics of spheroids at different initial cell densities for each cell line. By imaging and examination of the mean diameter of the spheroids at days 4 and 8, we can infer how the initial cell density affects spheroid growth over time. Optimal spheroid growth typically occurs when the initial cell density allows for robust proliferation without inducing excessive cell death or compromising nutrient and oxygen diffusion throughout the spheroid structure.

Figure 4.29 A and B illustrates the imaging and the mean diameter of spheroids formed from increasing seeding cell numbers over time is depicted for the HCT116 cell line at 4 and 8 days post-seeding.
At seeding densities ranging from 5,000 to 30,000 cells, compact spheroids are observed at day 4, with an increase in contrast indicative of higher cell density. For the spheroids seeded at a density of 50,000 cells, an outer diameter is already distinguishable at day 4. By day 8, this outer diameter becomes evident at seeding densities between 15,000 and 50,000 cells. Notably, spheroids seeded with 5k and 10k cells exhibit a modest increase in diameter from day 4 to day 8, suggesting ongoing growth and expansion of the spheroids. However, this trend is reversed for higher seeding densities (15, 20, 30, and 50k), where the diameter decreases over the same period

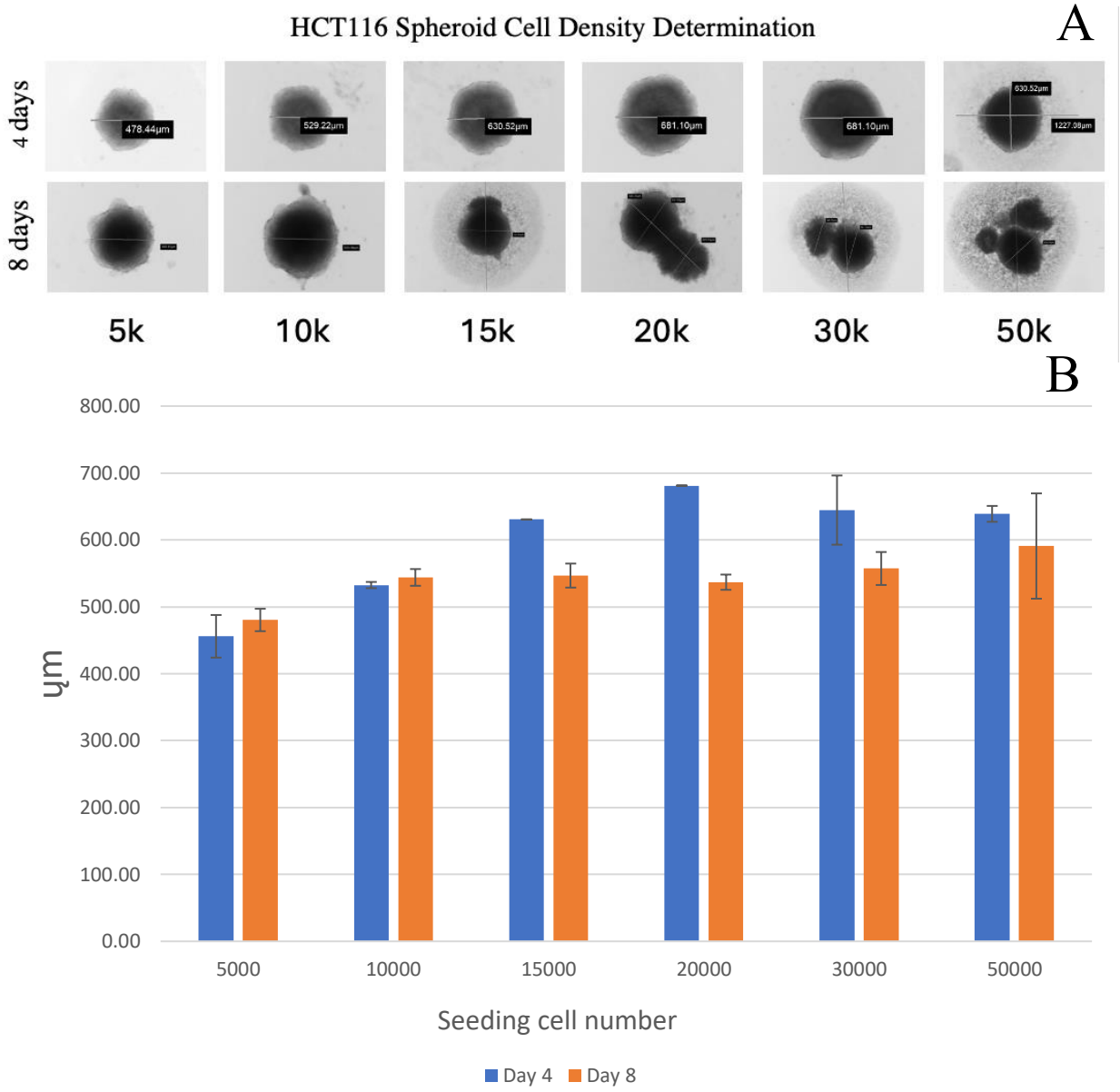

Figure 4.29 HCT116 spheroid density optimalisation

Spheroids of the HCT116 cell line at increasing initial cell densities over a period from day 4 to day 8 by A) transmitted light images using a Nikon SMZ25 stereo microscope with NIS Elements software and B) quantitative measurements of spheroid diameters. Y-axis shows mean diameter in micrometers. X-axis show increasing initial cell seeding densities. N = 2-3 biological replicates. Error bars = Std. Dev. Accompanying data is listed in Appendix G.

Figure 4.30 A and B illustrates the imaging and the mean diameter of spheroids formed from increasing seeding cell numbers over time is depicted for the SW948 cell line at 4 and 8 days post-seeding.

At 4 days, the outer diameter of the spheroid becomes slightly visible at a seeding density of 15,000 cells and is more prominent at densities ranging from 20,000 to 50,000 cells. By 8 days, this outer diameter is observable at seeding densities between 10,000 and 50,000 cells.

Spheroids seeded with 5-20k initial cell densities exhibit similar measurements and display an increasing trend in diameter, suggesting ongoing growth and expansion of the spheroids over the 8-day period. However, for the 30k initial cell density, there is a notable decrease in diameter after 8 days, indicating potential issues with spheroid growth or compaction at this higher density. Additionally, while the mean diameter of spheroids seeded with 50k initial cell density appears to increase from day 4 to day 8, it's important to note the high standard deviation, indicating variability within the samples.

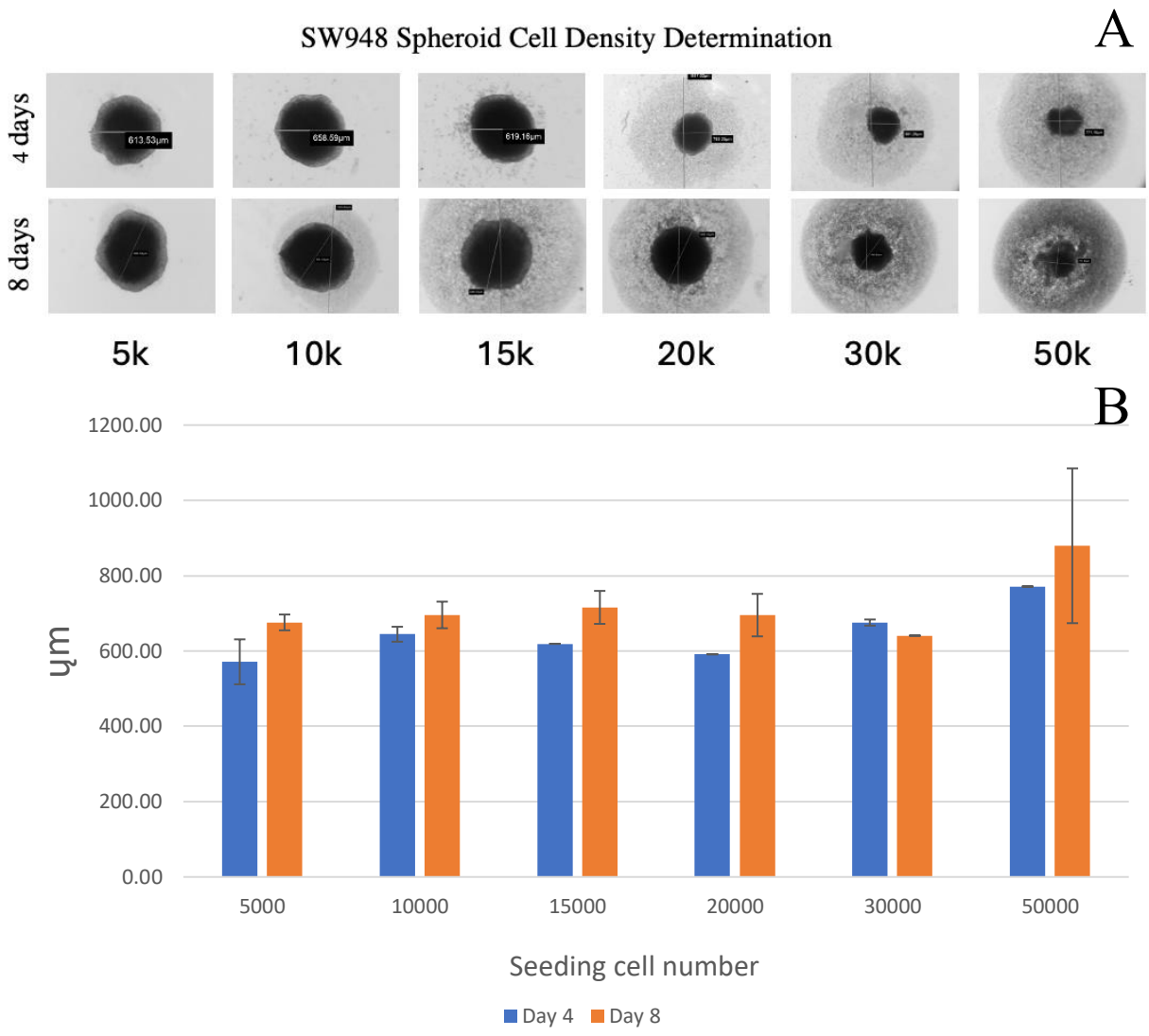

Figure 4.30 SW948 spheroid density optimalisation

Spheroids of the SW948 cell line at increasing initial cell densities over a period from day 4 to day 8 by A) transmitted light images using a Nikon SMZ25 stereo microscope with NIS Elements software and B) quantitative measurements of spheroid diameters. Y-axis shows mean diameter in micrometers. X-axis show increasing initial cell seeding densities. N = 2-3 biological replicates. Error bars = Std. Dev. Accompanying data is listed in Appendix G.

Figure 4.31 A and B illustrates the imaging and the mean diameter of spheroids formed from increasing seeding cell numbers over time is depicted for the SW948 cell line at 4 and 8 days post-seeding.

These spheroids appear more rigid than the other two cell lines, and lack a distinct spherical border. At 4 days, the outer diameter is observed at seeding densities of 30,000 to 50,000 cells. By 8 days, the spheroids lose their structural integrity and appear to disintegrate, with the outer border visible at all initial cell densities. A noticeable increase in spheroid diameter is observed from the 4th to the 8th day of culture for all initial cell densities. However, there appears to be no clear increase correlation between increasing initial cell density and spheroid diameter.

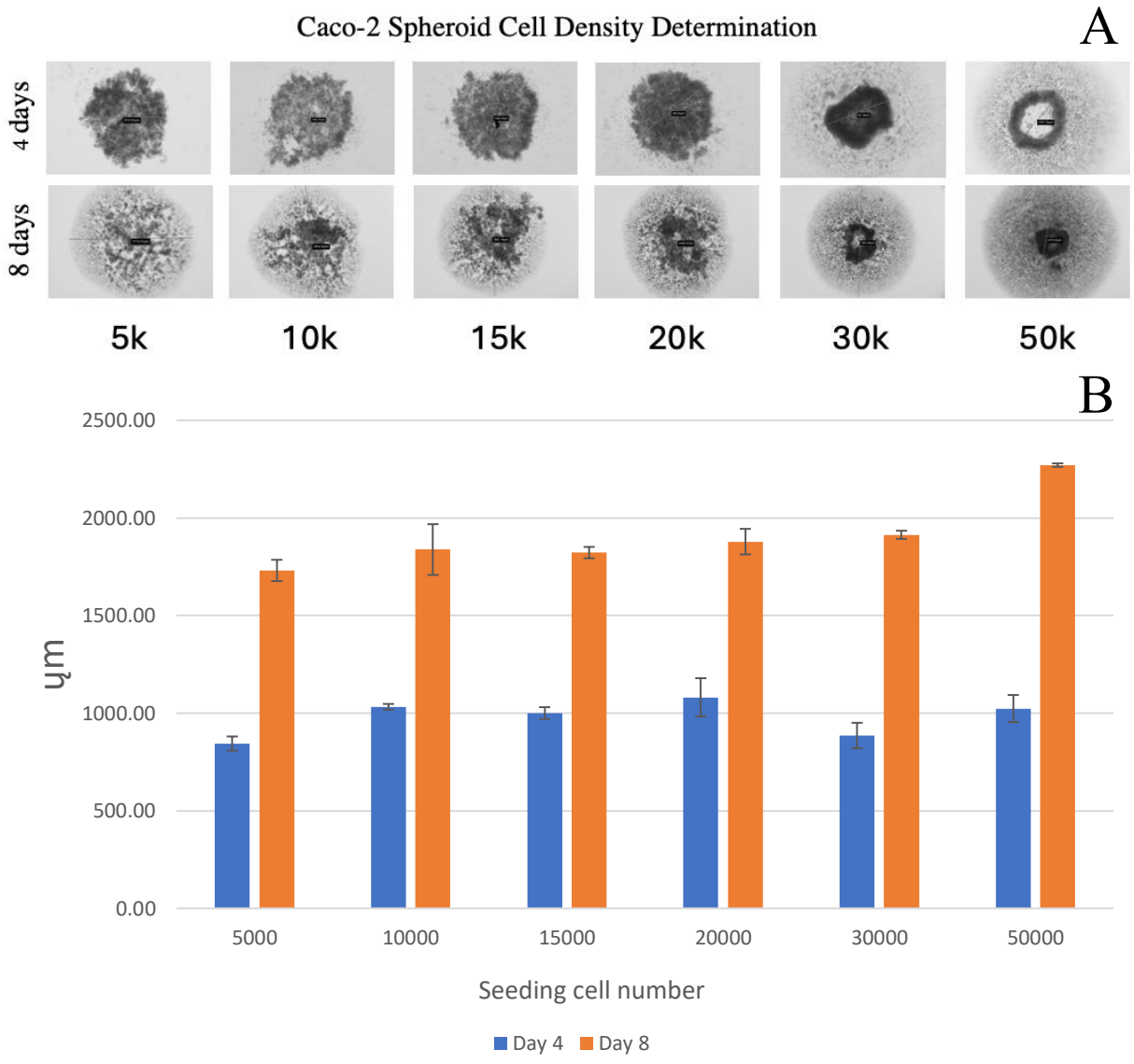

Figure 4.31 Caco-2 spheroid density optimalisation

Spheroids of the Caco-2 cell line at increasing initial cell densities over a period from day 4 to day 8 by A) transmitted light images using a Nikon SMZ25 stereo microscope with NIS Elements software and B) quantitative measurements of spheroid diameters. Y-axis shows mean diameter in micrometers. X-axis show increasing initial cell seeding densities. N = 2-3 biological replicates. Error bars = Std. Dev. Accompanying data is listed in Appendix G.

4.7 BA/PA Pretreatment to 5-FU Chemotherapy of 3D Spheroids Reveals Variability and Inconsistency

This assay was designed to investigate the combined effects of BA and PA on CRC spheroid viability and to evaluate their potential to enhance the efficacy of 5-FU, a commonly used chemotherapeutic agent. By utilizing a 3D spheroid model, which better mimics the tumor microenvironment compared to 2D cell cultures, we aimed to gain insights into the metabolic and cytotoxic responses of cancer cells to these treatments.

The following figures show the results of the fluorescent imaging and the mean fluorescence measurements for each individual combination treatment as well as the BA/PA treatment and the lowest and highest 5-FU treatment alone. The graph data is normalized to the untreated control. Green color in the fluorescence imaging is the Calcein AM, and the red represents the PI. The green Calcein AM represents the level of living cells, whereas PI is an impermeable dye that only stains dead cells.

Figure 4.32 shows the results for the HCT116 cell line. Overall, the Calcein AM is significantly decreased for all groups relative to the untreated control. The weakest Calcein signal is for both the BA/PA + 1,0 5-FU and BA/PA 4,0 5-FU. The BA/PA + 0,25 5-FU has the highest fluorescence signal of PI.

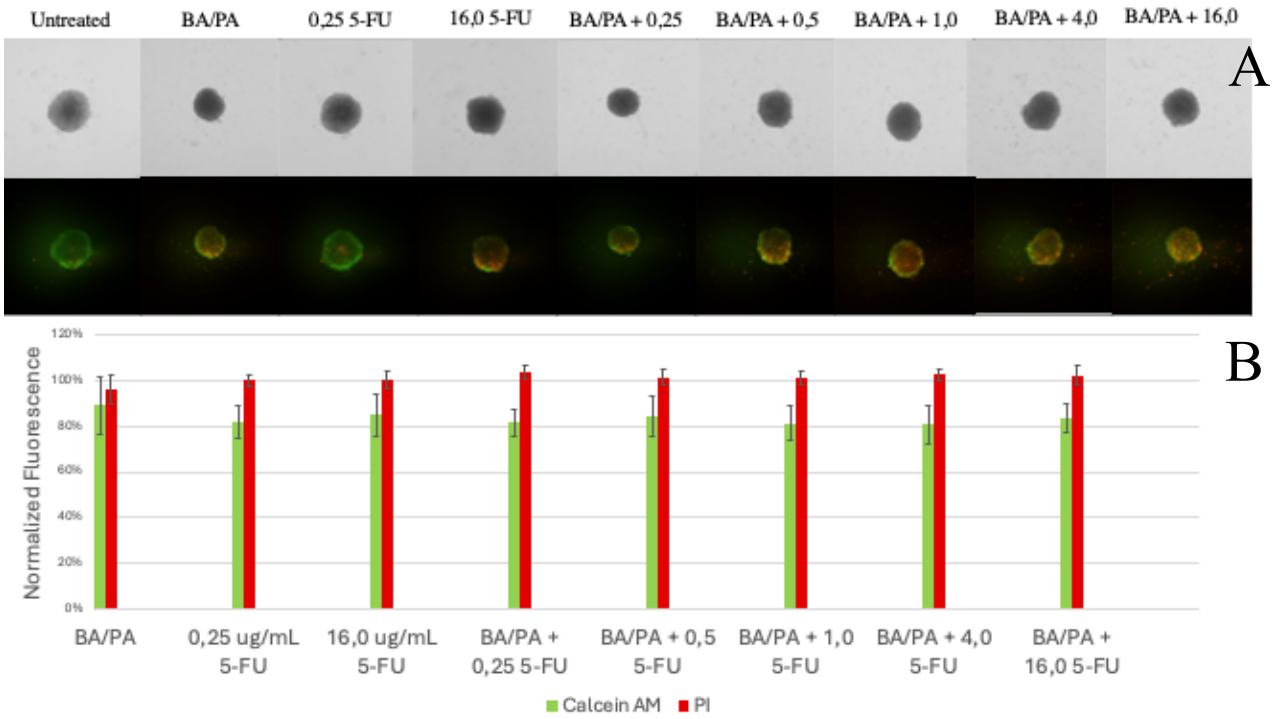

Figure 4.32 HCT116 BA/PA + 5-FU

A) Fluorescent imaging and B) normalized fluorescence data of spheroids of the HCT116 cell line after various treatments of 5+10 mM BA/PA and 5-FU in ug/mL. Green signal represents Calcein AM, and red signal represents PI. N = 6 biological replicates. Error bars = Std. Dev. Accompanying data is listed in Appendix H.

Figure 4.33 presents the results for the SW948 cell line. The treatment with BA/PA alone results in the highest Calcein AM fluorescence value among all treatments, indicating the highest cell viability. Interestingly, the combination treatments of BA/PA with 0.25 µg/mL, 0.5 µg/mL, and 4.0 µg/mL 5-FU exhibit higher Calcein AM values than the untreated control. On the other hand, the strongest PI fluorescence signals, indicating the highest levels of cell death, are observed with the singular lowest (0.25 µg/mL) and highest (16.0 µg/mL) 5-FU treatments.

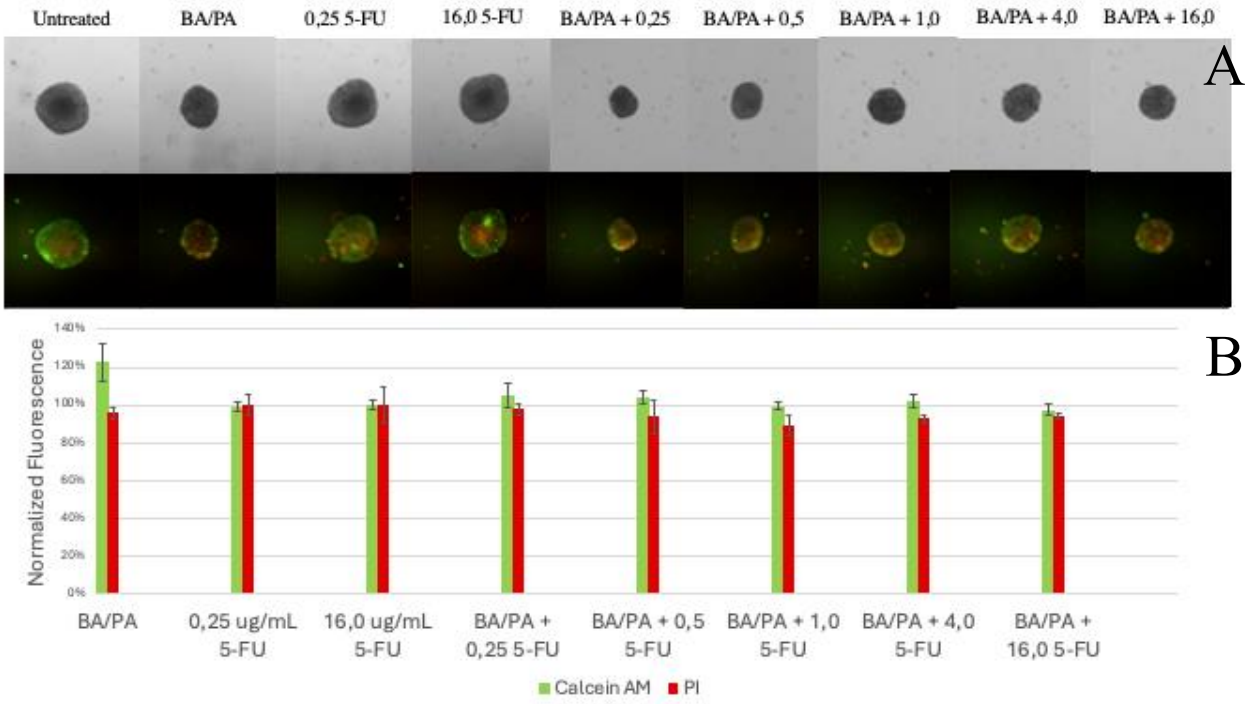

Figure 4.33 SW948 BA/PA + 5-FU

A) Fluorescent imaging and B) normalized fluorescence data of spheroids of the SW948 cell line after various treatments of 5+10 mM BA/PA and 5-FU in ug/mL Green signal represents Calcein AM, and red signal represents PI. N = 6 biological replicates. Error bars = Std. Dev. Accompanying data is listed in Appendix H.

Figure 4.34 shows the results for the Caco-2 cell line. The BA/PA + 1.0 µg/mL 5-FU treatment exhibits the weakest Calcein AM fluorescence signal, indicating the lowest cell viability among the treatment groups. In contrast, the singular treatments with the lowest (0.25 µg/mL) and highest (16.0 µg/mL) concentrations of 5-FU display the highest PI fluorescence signals, which are indicative of increased cell death. However, these PI signals do not exceed those of the untreated control, suggesting that while these concentrations of 5-FU induce cytotoxicity, the extent of cell death remains comparable to the baseline level observed in the untreated condition.

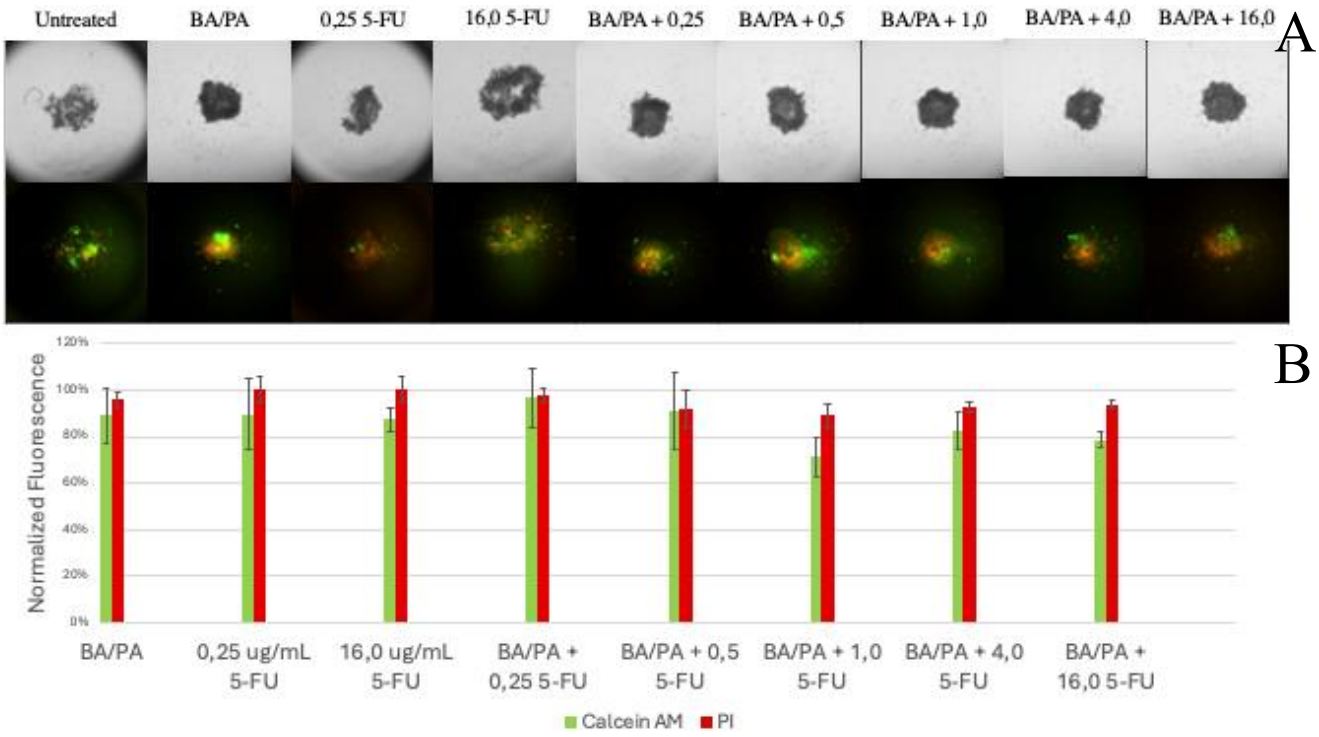

Figure 4.34 Caco-2 BA/PA + 5-FU

A) Fluorescent imaging and B) normalized fluorescence data of spheroids of the Caco-2 cell line after various treatments of 5+10 mM BA/PA and 5-FU in ug/mL Green signal represents Calcein AM, and red signal represents PI. N = 6 biological replicates. Error bars = Std. Dev. Accompanying data is listed in Appendix H.

5. Discussion

Increasing cases of CRC is a global health concern where diet and the gut microbiome plays an important part in CRC progression. BA and PA are naturally occurring SCFAs produced by the gut microbiota through the fermentation of dietary fibers. They have been shown to possess anti-carcinogenic properties, including the ability to inhibit cell proliferation, induce apoptosis, and modulate gene expression in cancer cells. In addition to their role in maintaining gut health and homeostasis, these SCFAs makes promising candidates for cancer treatment. We wanted to test how BA and PA as singular, combinatorial, and as a pretreatment to chemotherapy, affect three different CRC cell lines HCT116, SW948, and Caco-2. To stimulate various stress conditions, two glucose concentrations were used together with the singular and combinatorial treatments,

Singular BA/PA Treatments Exhibit Cytotoxic Dose Dependent Responses While Glucose Deprivation Decreases the Overall Cytotoxicity of BA/PA

Generally, the response of the HCT116, SW948, and Caco-2 cell lines to BA treatments exhibited a common decreasing trend in viability with increasing BA concentration, consistent with previous studies (74,83). This observed decrease in viability can be attributed to several mechanisms associated with BA-induced metabolic alterations in cancer cells. BA has been shown to inhibit HDAC-activity, leading to alterations in gene expression and cell cycle arrest (84). Additionally, BA can induce apoptosis in cancer cells by an induction of a cell stress response, further contributing to decreased cell viability (74). The higher sensitivity of cancer cells to BA-induced cytotoxicity compared to normal cells may be attributed to dysregulated metabolism and increased reliance on glycolysis for energy production, commonly known as the Warburg effect (62).

Similar with the BA treatments, the response of the HCT116, SW948, and Caco-2 cell lines to PA treatments exhibited a decreasing trend in viability with increasing PA concentration. This decrease in viability is consistent with previous studies demonstrating the cytotoxic effects of PA on cancer cells (75,85). PA has been reported to interfere with fatty acid metabolism and phospholipid synthesis, further contributing to impaired cell proliferation and survival (86).

Cancer cells exhibit metabolic plasticity, an ability to adapt their metabolic phenotypes under unfavorable conditions (87). Our findings show that decreased glucose availability increases

the overall viability of colorectal cancer cells compared to the standard physiological glucose environment when exposed to singular treatments of either BA or PA. In normal colonocytes, BA and PA can be utilized for oxidative metabolism as an alternative metabolic substrate. In cancerous cells, glycolysis is favored, leading to an inefficient metabolism of BA and PA (88). Given the metabolic plasticity of cancer cells, BA and PA might be utilized as an energy source more than a cytotoxic agent under glucose starved conditions.

Glucose deprivation can impair glycolysis and the PPP, leading to oxidative stress caused by an imbalance between the production of ROS and the antioxidant system (53,89). This redox imbalance can lead to cell death. However, BA has the ability to modulate oxidative stress responses and decrease ROS levels (90). The interaction between glucose starvation and BA exposure might boost cellular antioxidant capacity by adjusting oxidative stress responses and antioxidant production, which might lead to reduced cytotoxicity and increased cell survival.

Interestingly, the Caco-2 cell line exhibited a unique response to BA treatments for the glucose starved group, characterized by a distinct increase in viability relative to the untreated control, across all BA concentrations tested. This unexpected increase in viability contradicts the typical cytotoxic effects of BA observed in cancer cells. One possible explanation for this phenomenon is the metabolic flexibility of Caco-2 cells, which may exhibit differential responses to metabolic stressors compared to other CRC lines (91). The exposure of BA might lead to a modulation of the cell's metabolic plasticity, and BA could be solely used as a metabolic energy source, although further investigation is warranted to elucidate the underlying mechanisms.

We also aimed to investigate the impact of these SCFAs on key mitochondrial parameters, including basal respiration, proton leak, spare respiratory capacity, and ATP-production coupled respiration. The Seahorse XF Cell Mito Stress Test provided a robust platform to measure these parameters, offering insights into the metabolic responses of CRC cells to BA and PA treatments.
Both BA and PA displayed a biphasic response in mitochondrial respiration across the HCT116, SW948, and Caco-2 cell lines. At lower concentrations (1.0-1.5 mM for BA and 5-10 mM for PA), there was an increase in OCR, suggesting a stimulatory effect on mitochondrial function. This could be attributed to enhanced mitochondrial biogenesis or upregulation of respiratory chain activity, potentially mediated by HDAC inhibition and

subsequent gene expression changes promoting mitochondrial function. Higher concentrations (3.0-5.0 mM for BA and 25-50 mM for PA) resulted in decreased OCR, indicative of mitochondrial stress or toxicity. This could be due to the overproduction of ROS, leading to oxidative damage and impairment of mitochondrial components, or direct inhibition of respiratory chain complexes.

Basal respiration represents the initial OCR before any of the modulators are added, and is calculated by subtracting the non-mitochondrial respiration (OCR after rotenone + AA) from the initial baseline measurements. Thus, indicating the overall mitochondrial activity under normal conditions. High basal respiration suggests an active mitochondria and a high ATP demand, while low basal respiration might indicate mitochondrial dysfunction or low ATP requirements. Proton leak is calculated by subtracting the non-mitochondrial respiration from the OCR after the oligomycin injection, and represents the amount of proton flux across the mitochondrial membrane independent of ATP synthase. Oligomycin inhibits complex V in the ETC which prevents protons from flowing back into the mitochondrial matrix through ATP synthase, thus stopping ATP production. High proton leak might be an indicator of mitochondrial uncoupling, which can protect against oxidative stress, but also reduce the efficiency of ATP production. FCCP functions as a protonophore, creating a free flow of protons across the mitochondrial membrane, measuring the cells maximal respiration. Spare respiratory capacity is calculated by subtracting the basal respiration from the maximal respiration, indicating the extra capacity the mitochondria has under stress or increased workload. High spare respiratory capacity suggests a flexible mitochondrial system that is capable of responding to high energy demands, while low spare respiratory capacity might indicate a compromised energy production capability. The ATP-production linked respiration measures the portion of metabolism directly linked to ATP production, and is calculated by subtracting the OCR after the oligomycin injection from the basal respiration. It determines how effectively the mitochondria are producing ATP. A decrease in this parameter could indicate issues with ATP synthase or a shift towards a more glycolytic metabolism. The slight increase in ATP production can suggest that lower concentrations of BA can be beneficial for energy metabolism in terms of using the SCFA as an energy source.

Variations in basal respiration, proton leak, spare respiratory capacity, and ATP-production linked respiration observed across the different cell lines underscores the importance of understanding cell type specific effects.

BA/PA Combinations Exhibit Synergistic Effects and Increase Cytotoxicity Under Glucose Starved Conditions

The general data indicate potential synergistic interactions at lower concentrations of PA with increasing BA, particularly notable in the HCT116 and SW948 cell lines. Synergistic effects are often used in combination therapies to enhance therapeutic efficacy while minimizing toxicity (92). This observed synergy may result from a complementary mechanisms of action of BA and PA. Conversely, high concentrations of PA seemed to reduce the cells' sensitivity to BA, which underscores the importance of optimizing combination ratios to achieve the desired therapeutic outcome.

The observed enhanced efficacy of BA/PA combinations under glucose-starved conditions compared to higher glucose conditions contradicts the increased viability in the singular treatments, but aligns with existing literature on the metabolic dependencies of cancer cells. Cancer cells often exhibit increased sensitivity to metabolic stress due to their high metabolic rate and reliance on glucose (57). Under glucose starvation, cells are more vulnerable to treatments that further disrupt their metabolic pathways (93). This increased sensitivity was present in all three cell lines, suggesting that metabolic stress favors the cytotoxic effects of BA and PA combinatorial treatments.

BA and PA Gave Mixed Responses to Pretreatment in Enhancing 5-FU Chemotherapy Efficacy

The goal of pretreatment is to sensitize cancer cells to chemotherapy, making them more vulnerable to subsequent cytotoxic attacks. By priming the cells at a moderate level, there is an opportunity to maximize the impact of chemotherapy. The 5+10 mM BA+PA combination showed significant, yet not overly aggressive reductions in cell viability across the colorectal cancer cell lines tested. This indicates a potent effect that is substantial enough to impact cell survival but not so high as to cause extreme toxicity that could complicate further treatment processes. The pretreatment of BA and PA to 5-FU on colorectal cancer cell lines HCT116, SW948, and Caco-2 was assessed using fluorescent measurements and imaging to determine cell viability and cytotoxicity. The fluorescence signals of Calcein AM and PI were used as indicators of living and dead cells, respectively.

For the HCT116 cell line, the combination of BA/PA pretreatment with 1.0 μg/mL and 4.0 μg/mL 5-FU resulted in the lowest Calcein AM fluorescence signals, indicating significant reductions in cell viability. This suggests that the combination treatments were highly effective in reducing the viability of HCT116 cells. The highest PI fluorescence signal was observed for the BA/PA + 0.25 μg/mL 5-FU combination, indicating elevated levels of cell death at this concentration.

These results are consistent with current research suggesting that SCFAs can enhance the efficacy of chemotherapeutic agents (28,48). SCFAs like BA and PA are known to modulate cellular metabolism, induce apoptosis, and enhance the anti-tumor effects of chemotherapy. The significant reduction in cell viability and increased cell death observed in our study align with these mechanisms. However, the varying efficacy at different 5-FU concentrations highlights the importance of optimizing dosage for maximal therapeutic effect.

In the SW948 cell line, BA/PA pretreatment alone resulted in the highest Calcein AM fluorescence, indicating that SCFAs may have a protective effect on cell viability in the absence of 5-FU. Interestingly, the combination treatments of BA/PA with 0.25 μg/mL, 0.5 μg/mL, and 4.0 μg/mL 5-FU showed higher cell viability compared to the untreated control. This suggests a potential antagonistic interaction between BA/PA and 5-FU at these concentrations, where the presence of SCFAs may mitigate the cytotoxic effects of 5-FU. The highest PI fluorescence signals were observed with the lowest (0.25 μg/mL) and highest (16.0 μg/mL) concentrations of 5-FU alone, indicating significant cell death. These findings suggest that while SCFAs alone can maintain cell viability, their combination with certain concentrations of 5-FU may not produce a synergistic cytotoxic effect, and in some cases, might reduce the efficacy of 5-FU.

For the Caco-2 cell line, the combination treatment of BA/PA with 1.0 μg/mL 5-FU resulted in the weakest Calcein AM fluorescence signal, indicating the lowest cell viability. Conversely, the highest PI fluorescence signals were seen with the lowest (0.25 μg/mL) and highest (16.0 μg/mL) concentrations of 5-FU alone. However, these signals did not exceed those of the untreated control, suggesting that while 5-FU induces cytotoxicity, its effect is comparable to the baseline level observed without treatment.

These results indicate that for Caco-2 cells, a certain threshold of 5-FU concentration, when combined with SCFAs, can significantly reduce cell viability. However, the cytotoxic effects do not linearly correlate with increasing concentrations of 5-FU, highlighting the complex interplay between SCFAs and chemotherapy agents in different cellular contexts.

5.1 Methodological Considerations and Limitations

Glucose Deprivation and Assay Timing

The cell lines were subjected to different glucose conditions (0.5 mM and 5 mM) and tested at various time points based on their confluency. Cells under glucose starvation had difficulties proliferating, leading to some assays being performed later than others. This prolonged glucose starvation likely had an overall impact on cellular metabolism and viability, potentially affecting the consistency of the results. To improve this, future studies should standardize the timing of assays.

Seahorse XF Cell Mito Stress Test

The accuracy of the Seahorse XF Cell Mito Stress Test results depends on precise calibration and assay conditions. Variations in these factors could potentially influence the observed OCR values and should be controlled to ensure reproducibility and reliability of the data. The BA and PA singular treatments with the Seahorse XF Cell Mito Stress Test was only replicated once. Despite having several replicates, running the assay only once per cell line can introduce variability and affect the reliability of the results. High SD observed in some treatments indicates inconsistency. Repeating the Seahorse assay multiple times for each cell line and averaging the results would provide a more robust and reliable dataset. Additionally, ensuring consistent assay conditions and reagent quality across all runs can further reduce variability.

CCK-8 BA/PA Combination Treatments

As outlined in the methods section, we performed six biological replicates over two individual plates to ensure robustness and reliability of the experimental data. However, it is noteworthy that there was a clear difference in absorbance for the same treatment across the two different plates. Several factors could potentially influence this variability, including differences in cell confluence, microenvironmental conditions, and technical variations during experimental procedures. These discrepancies may contribute to the observed unreliable data and high SD.

Fluorescence Staining

Measuring fluorescence signals in 3D spheroids is inherently more complicated than in 2D cell cultures. The 3D structure of spheroids can cause uneven penetration of staining dyes,

leading to heterogeneous fluorescence signals. This can result in inaccurate quantification of cell viability and death within different regions of the spheroid. Additionally, the measured fluorescence versus the fluorescence imaging did not correlate to each other. Increased signal in the fluorescence imaging did not correlate to increased fluorescence signal measured. To improve the accuracy of these measurements, future studies could employ more advanced imaging techniques such as confocal microscopy to obtain more uniform and reliable fluorescence signals.

6. Conclusion and Future Perspectives

Conclusion

Singular BA and PA treatments showed a common trend of decreased viability with increasing concentrations for all cell lines, consistent with their known anticarcinogenic effects. In glucose deprived media, the CRC cells showed increased viability to BA and PA treatments, suggesting that CRC cells might utilize BA and PA as alternative energy sources more than cytotoxic agents. The Seahorse XF Cell Mito Stress Test showed a biphasic response, where lower concentrations enhanced mitochondrial function and higher concentrations caused mitochondrial stress. Variations in basal respiration, proton leak, spare respiratory capacity, and ATP-production linked respiration among the three cell lines indicate cell type specific responses, which underscores the need for optimized and personalized treatment concentrations. Combinatorial treatments of BA and PA indicate potential synergistic effects at lower PA concentrations with increasing BA. However, higher PA concentrations seemed to reduce the sensitivity to BA. Under glucose starved conditions, the combination of BA and PA had enhanced efficacy compared to the standard physiological concentration, indicating increased cytotoxicity under metabolic stress.
We also aimed to use a combination of BA and PA as a pretreatment to 5-FU chemotherapy. The results, however, gave variable and unreliable data. The response varied across the different concentration and cell lines. These results do not exclude the possibility of SCFAs enhancing the efficacy of chemotherapeutic agents, but one should employ more advanced imaging techniques for more accurate results.

Future Perspectives

Future studies should focus on elucidating the specific underlying mechanisms of BA and PA induced metabolic alterations in different CRC cell lines, both as singular- and combinatorial treatments. Also, understanding the cell type specific responses is important for the development of personalized therapy. The full metabolic profiles of each individual cell line should be taken into consideration when determining the optimal concentrations for combination treatments. Exploring the synergistic and possible antagonistic interactions between these SCFAs to chemotherapeutic agents will also help optimize combination therapies.

Glucose deprivation has shown to have a significant effect on modulating the efficacy of BA and PA, and offers valuable insight into the enhancement of cancer treatment. Although, a decreased glucose concentration *in vivo,* also called hypoglycemia, could potentially be life-threatening (94) and could be difficult to implicate clinically as a part of combination treatments. Other stress factors that could possibly influence the cytotoxic and metabolic effects of these SCFAs, such as hypoxia, nutrient deprivation or oxidative stress should be investigated to improve therapeutic strategies in a more representative manner.

Additionally, to better mimic the *in vivo* conditions and thus a more representative effect and understanding of these SCFAs, future research should employ more advanced culture models such as spheroids or organoids that can provide a more accurate representation of the tumor microenvironment. This allows for the study of cell-cell and cell-matrix interactions and will close the gap between *in vitro* studies and clinical applications.

If BA and PA ultimately show to have a significant effect on enhancing CRC treatment, these SCFAs could be integrated into the treatment regimen. Investigating how manipulating the gut microbiome composition can enhance SCFA production is an area of interest. Donohoe et. al showed that neither SCFA producing bacteria nor a high fiber diet on their own had a protective effect against the development of CRC, but showed a positive effect when combined (95). The manipulation could therefore consist of a combination of SCFA supplements, probiotics, prebiotics, or synbiotics. Also, a personalized nutrition recommendation that optimize SCFA production should be developed for individuals at risk for CRC.

References

1. Nall R. Medical News Today. 2020 [cited 2024 May 7]. What to know about cancer. Available from: https://www.medicalnewstoday.com/articles/323648
2. WHO. World Health Organization. 2024 [cited 2024 May 15]. Global cancer burden growing, amidst mounting need for services. Available from: https://www.who.int/news/item/01-02-2024-global-cancer-burden-growing--amidst-mounting-need-for-services
3. WHO. Colorectal cancer [Internet]. 2023 [cited 2024 May 16]. Available from: https://www.who.int/news-room/fact-sheets/detail/colorectal-cancer
4. Holmes D. A disease of growth. Nature. 2015 May;521(7551):S2–3.
5. Balchen V, Simon K. Colorectal cancer development and advances in screening. Clin Interv Aging. 2016 Jul;Volume 11:967–76.
6. Bluegrass Coalition for Colorectal Screening, KMA Cancer Committee. Colorectal cancer facts. J Ky Med Assoc. 2005 Mar;103(3):118.
7. Stracci F, Zorzi M, Grazzini G. Colorectal Cancer Screening: Tests, Strategies, and Perspectives. Front Public Health [Internet]. 2014 Oct 27 [cited 2024 May 29];2. Available from: http://journal.frontiersin.org/article/10.3389/fpubh.2014.00210/abstract
8. Levine JS, Ahnen DJ. Adenomatous Polyps of the Colon. N Engl J Med. 2006 Dec 14;355(24):2551–7.
9. Frank SA. Dynamics of Cancer: Incidence, Inheritance, and Evolution [Internet]. Princeton (NJ): Princeton University Press; 2007 [cited 2024 May 29]. Available from: http://www.ncbi.nlm.nih.gov/books/NBK1568/
10. Zhu X, Li S. Ferroptosis, Necroptosis, and Pyroptosis in Gastrointestinal Cancers: The Chief Culprits of Tumor Progression and Drug Resistance. Adv Sci. 2023 Sep;10(26):2300824.
11. Dey A, Mitra A, Pathak S, Prasad S, Zhang AS, Zhang H, et al. Recent Advancements, Limitations, and Future Perspectives of the use of Personalized Medicine in Treatment of Colon Cancer. Technol Cancer Res Treat. 2023 Jan;22:153303382311784.
12. Colon Cancer Treatment (PDQ®) - NCI [Internet]. 2024 [cited 2024 Jun 2]. Available from: https://www.cancer.gov/types/colorectal/hp/colon-treatment-pdq
13. Sawicki T, Ruszkowska M, Danielewicz A, Niedźwiedzka E, Arłukowicz T, Przybyłowicz KE. A Review of Colorectal Cancer in Terms of Epidemiology, Risk Factors, Development, Symptoms and Diagnosis. Cancers. 2021 Apr 22;13(9):2025.
14. Mármol I, Sánchez-de-Diego C, Pradilla Dieste A, Cerrada E, Rodriguez Yoldi M. Colorectal Carcinoma: A General Overview and Future Perspectives in Colorectal Cancer. Int J Mol Sci. 2017 Jan 19;18(1):197.
15. Chao X, Lei Z, Hongqin L, Ziwei W, Dechuan L, Weidong D, et al. Faeces from malnourished colorectal cancer patients accelerate cancer progression. Clin Nutr. 2022 Mar;41(3):632–44.
16. Portincasa P, Bonfrate L, Vacca M, De Angelis M, Farella I, Lanza E, et al. Gut Microbiota and Short Chain Fatty Acids: Implications in Glucose Homeostasis. Int J Mol Sci. 2022 Jan 20;23(3):1105.
17. Bull MJ, Plummer NT. Part 1: The Human Gut Microbiome in Health and Disease. Integr Med Encinitas Calif. 2014 Dec;13(6):17–22.
18. Song M, Chan AT, Sun J. Influence of the Gut Microbiome, Diet, and Environment on Risk of Colorectal Cancer. Gastroenterology. 2020 Jan;158(2):322–40.
19. Saus E, Iraola-Guzmán S, Willis JR, Brunet-Vega A, Gabaldón T. Microbiome and colorectal cancer: Roles in carcinogenesis and clinical potential. Mol Aspects Med. 2019 Oct;69:93–106.

20. Siddiqui R, Boghossian A, Alharbi AM, Alfahemi H, Khan NA. The Pivotal Role of the Gut Microbiome in Colorectal Cancer. Biology. 2022 Nov 9;11(11):1642.
21. Sarhadi V, Lahti L, Saberi F, Youssef O, Kokkola A, Karla T, et al. Gut Microbiota and Host Gene Mutations in Colorectal Cancer Patients and Controls of Iranian and Finnish Origin. Anticancer Res. 2020 Mar;40(3):1325–34.
22. Baena R, Salinas P. Diet and colorectal cancer. Maturitas. 2015 Mar;80(3):258–64.
23. Sánchez-Alcoholado L, Ramos-Molina B, Otero A, Laborda-Illanes A, Ordóñez R, Medina JA, et al. The Role of the Gut Microbiome in Colorectal Cancer Development and Therapy Response. Cancers. 2020 May 29;12(6):1406.
24. Yang Y, Misra BB, Liang L, Bi D, Weng W, Wu W, et al. Integrated microbiome and metabolome analysis reveals a novel interplay between commensal bacteria and metabolites in colorectal cancer. Theranostics. 2019;9(14):4101–14.
25. Tan J, McKenzie C, Potamitis M, Thorburn AN, Mackay CR, Macia L. The Role of Short-Chain Fatty Acids in Health and Disease. In: Advances in Immunology [Internet]. Elsevier; 2014 [cited 2024 May 18]. p. 91–119. Available from: https://linkinghub.elsevier.com/retrieve/pii/B9780128001004000039
26. Fusco W, Lorenzo MB, Cintoni M, Porcari S, Rinninella E, Kaitsas F, et al. Short-Chain Fatty-Acid-Producing Bacteria: Key Components of the Human Gut Microbiota. Nutrients. 2023 May 6;15(9):2211.
27. Healthline [Internet]. 2016 [cited 2024 Jun 14]. How Short-Chain Fatty Acids Affect Health and Weight. Available from: https://www.healthline.com/nutrition/short-chain-fatty-acids-101
28. Al-Qadami GH, Secombe KR, Subramaniam CB, Wardill HR, Bowen JM. Gut Microbiota-Derived Short-Chain Fatty Acids: Impact on Cancer Treatment Response and Toxicities. Microorganisms. 2022 Oct 17;10(10):2048.
29. Biology LibreTexts [Internet]. 2016 [cited 2024 Jun 5]. 6.11: Fatty Acid Oxidation. Available from: https://bio.libretexts.org/Bookshelves/Biochemistry/Book%3A_Biochemistry_Free_and_Easy_(Ahern_and_Rajagopal)/06%3A_Metabolism_I_-_Oxidative_Reductive_Processes/6.11%3A_Fatty_Acid_Oxidation
30. Fig1_FA_β-oxidation.png 552 × 424 bildepunkter [Internet]. [cited 2024 Jun 5]. Available from: https://lipidlibrary.aocs.org/Images/LipidLibrary/Animal/Fig1_FA_%CE%B2-oxidation.png
31. Propionic Acid Pathway Mnemonic for USMLE [Internet]. [cited 2024 May 22]. Available from: https://pixorize.com/view/5125
32. Wongkittichote P, Ah Mew N, Chapman KA. Propionyl-CoA carboxylase – A review. Mol Genet Metab. 2017 Dec;122(4):145–52.
33. Mirzaei R, Afaghi A, Babakhani S, Sohrabi MR, Hosseini-Fard SR, Babolhavaeji K, et al. Role of microbiota-derived short-chain fatty acids in cancer development and prevention. Biomed Pharmacother. 2021 Jul;139:111619.
34. Hu S, Liu L, Chang EB, Wang JY, Raufman JP. Butyrate inhibits pro-proliferative miR-92a by diminishing c-Myc-induced miR-17-92a cluster transcription in human colon cancer cells. Mol Cancer. 2015 Dec;14(1):180.
35. Seto E, Yoshida M. Erasers of Histone Acetylation: The Histone Deacetylase Enzymes. Cold Spring Harb Perspect Biol. 2014 Apr 1;6(4):a018713–a018713.
36. Lazarova DL, Bordonaro M. Vimentin, colon cancer progression and resistance to butyrate and other HDAC is. J Cell Mol Med. 2016 Jun;20(6):989–93.
37. Li Q, Cao L, Tian Y, Zhang P, Ding C, Lu W, et al. Butyrate Suppresses the Proliferation of Colorectal Cancer Cells via Targeting Pyruvate Kinase M2 and Metabolic Reprogramming. Mol Cell Proteomics. 2018 Aug;17(8):1531–45.

38. Filippone A, Lanza M, Campolo M, Casili G, Paterniti I, Cuzzocrea S, et al. The Anti-Inflammatory and Antioxidant Effects of Sodium Propionate. Int J Mol Sci. 2020 Apr 24;21(8):3026.
39. Kim K, Kwon O, Ryu TY, Jung CR, Kim J, Min JK, et al. Propionate of a microbiota metabolite induces cell apoptosis and cell cycle arrest in lung cancer. Mol Med Rep. 2019 Aug;20(2):1569–74.
40. Silva LG, Ferguson BS, Avila AS, Faciola AP. Sodium propionate and sodium butyrate effects on histone deacetylase (HDAC) activity, histone acetylation, and inflammatory gene expression in bovine mammary epithelial cells1. J Anim Sci [Internet]. 2018 Sep 25 [cited 2024 May 24]; Available from: https://academic.oup.com/jas/advance-article/doi/10.1093/jas/sky373/5106615
41. Kobayashi M, Mikami D, Uwada J, Yazawa T, Kamiyama K, Kimura H, et al. A short-chain fatty acid, propionate, enhances the cytotoxic effect of cisplatin by modulating GPR41 signaling pathways in HepG2 cells. Oncotarget. 2018 Jul 31;9(59):31342–54.
42. Ash R, Baird GD. Activation of volatile fatty acids in bovine liver and rumen epithelium. Evidence for control by autoregulation. Biochem J. 1973 Oct 1;136(2):311–9.
43. Casale J, Patel P. Fluorouracil. In: StatPearls [Internet]. Treasure Island (FL): StatPearls Publishing; 2024 [cited 2024 May 22]. Available from: http://www.ncbi.nlm.nih.gov/books/NBK549808/
44. Peng C, Saffo S, Shusterman M, Becker DJ, Berlin J, Oberstein PE, et al. Analysis of the impact of eliminating bolus 5-fluorouracil in metastatic colorectal cancer. J Clin Oncol. 2023 Feb 1;41(4_suppl):59–59.
45. Zhang N, Yin Y, Xu SJ, Chen WS. 5-Fluorouracil: Mechanisms of Resistance and Reversal Strategies. Molecules. 2008 Aug 5;13(8):1551–69.
46. Chemical-structure-of-5-fluorouracil_W640.jpg 606 × 648 bildepunkter [Internet]. [cited 2024 Jun 3]. Available from: https://www.researchgate.net/publication/332193052/figure/fig1/AS:743948725272577@1554382606623/Chemical-structure-of-5-fluorouracil_W640.jpg
47. Sethy C, Kundu CN. 5-Fluorouracil (5-FU) resistance and the new strategy to enhance the sensitivity against cancer: Implication of DNA repair inhibition. Biomed Pharmacother. 2021 May;137:111285.
48. Geng HW, Yin FY, Zhang ZF, Gong X, Yang Y. Butyrate Suppresses Glucose Metabolism of Colorectal Cancer Cells via GPR109a-AKT Signaling Pathway and Enhances Chemotherapy. Front Mol Biosci. 2021 Mar 29;8:634874.
49. Loh S. English: Simplified summary of the 10 reactions in glycolysis noting the reactants and products [Internet]. 2022 [cited 2024 Jun 4]. Available from: https://commons.wikimedia.org/w/index.php?curid=118301216
50. Tricarboxylic Acid Cycle Metabolism Service - Creative Proteomics [Internet]. [cited 2024 Jun 4]. Available from: https://metabolomics.creative-proteomics.com/citrate-cycle-metabolism-service.htm
51. Khan Academy, ETC [Internet]. [cited 2024 Jun 4]. Available from: https://cdn.kastatic.org/ka-perseus-images/62120415688fc64d57237535d282247e981bdfed.png
52. Stincone A, Prigione A, Cramer T, Wamelink MMC, Campbell K, Cheung E, et al. The return of metabolism: biochemistry and physiology of the pentose phosphate pathway. Biol Rev. 2015 Aug;90(3):927–63.
53. Stine ZE, Altman BJ, Hsieh AL, Gouw AM, Dang CV. Deregulation of the Cellular Energetics of Cancer Cells. In: Pathobiology of Human Disease [Internet]. Elsevier; 2014 [cited 2024 May 22]. p. 444–55. Available from: https://linkinghub.elsevier.com/retrieve/pii/B9780123864567019122

54. Pentose Phosphate Pathway - Glycolysis Gluconeogenesis And The Pentose Phosphate Pathway - MCAT Content [Internet]. [cited 2024 Jun 4]. Available from: https://jackwestin.com/resources/mcat-content/glycolysis-gluconeogenesis-and-the-pentose-phosphate-pathway/pentose-phosphate-pathway
55. Hanahan D, Weinberg RA. Hallmarks of Cancer: The Next Generation. Cell. 2011 Mar 4;144(5):646–74.
56. Hallmarks of Cancer [Internet]. [cited 2024 Jun 3]. Available from: https://ars.els-cdn.com/content/image/1-s2.0-S0092867411001279-gr6.jpg
57. Warburg O, Wind F, Negelein E. THE METABOLISM OF TUMORS IN THE BODY. J Gen Physiol. 1927 Mar 7;8(6):519–30.
58. Corrado M, Scorrano L, Campello S. Mitochondrial Dynamics in Cancer and Neurodegenerative and Neuroinflammatory Diseases. Int J Cell Biol. 2012;2012:1–13.
59. Porporato PE, Filigheddu N, Pedro JMBS, Kroemer G, Galluzzi L. Mitochondrial metabolism and cancer. Cell Res. 2018 Mar;28(3):265–80.
60. Wang SF, Chen S, Tseng LM, Lee HC. Role of the mitochondrial stress response in human cancer progression. Exp Biol Med. 2020 May;245(10):861–78.
61. Brown RE, Short SP, Williams CS. Colorectal Cancer and Metabolism. Curr Colorectal Cancer Rep. 2018 Dec;14(6):226–41.
62. Levine AJ, Puzio-Kuter AM. The Control of the Metabolic Switch in Cancers by Oncogenes and Tumor Suppressor Genes. Science. 2010 Dec 3;330(6009):1340–4.
63. Liou GY, Storz P. Reactive oxygen species in cancer. Free Radic Res. 2010 Jan;44(5):479–96.
64. Lieberman BP, Ploessl K, Wang L, Qu W, Zha Z, Wise DR, et al. PET Imaging of Glutaminolysis in Tumors by 18F-(2S,4R)4-Fluoroglutamine. J Nucl Med. 2011 Dec 1;52(12):1947–55.
65. Sharkey L. Glutamine and Cancer: How It Works, What to Do [Internet]. 2022 [cited 2024 May 18]. Available from: https://www.healthline.com/health/glutamine-and-cancer#short-answer
66. Yang L, Venneti S, Nagrath D. Glutaminolysis: A Hallmark of Cancer Metabolism. Annu Rev Biomed Eng. 2017 Jun 21;19(Volume 19, 2017):163–94.
67. Liu G, Zhu J, Yu M, Cai C, Zhou Y, Yu M, et al. Glutamate dehydrogenase is a novel prognostic marker and predicts metastases in colorectal cancer patients. J Transl Med. 2015 Dec;13(1):144.
68. Song Z, Wei B, Lu C, Li P, Chen L. Glutaminase sustains cell survival via the regulation of glycolysis and glutaminolysis in colorectal cancer. Oncol Lett. 2017 Sep;14(3):3117–23.
69. 220px-Glutaminolysisengl2.png 220 × 165 bildepunkter [Internet]. [cited 2024 Jun 5]. Available from: https://upload.wikimedia.org/wikipedia/commons/thumb/f/fb/Glutaminolysisengl2.png/220px-Glutaminolysisengl2.png
70. Kapałczyńska M, Kolenda T, Przybyła W, Zajączkowska M, Teresiak A, Filas V, et al. 2D and 3D cell cultures – a comparison of different types of cancer cell cultures. Arch Med Sci [Internet]. 2016 [cited 2024 Jun 14]; Available from: https://www.termedia.pl/doi/10.5114/aoms.2016.63743
71. Breslin S, O'Driscoll L. Three-dimensional cell culture: the missing link in drug discovery. Drug Discov Today. 2013 Mar;18(5–6):240–9.
72. Introduction to 3D Cell Culture [Internet]. [cited 2024 Jun 14]. Available from: https://no.promega.com/resources/guides/cell-biology/3d-cell-culture-guide/
73. Sedlak JC, Yilmaz ÖH, Roper J. Metabolism and Colorectal Cancer. Annu Rev Pathol Mech Dis. 2023 Jan 24;18(1):467–92.

74. Fung KYC, Brierley GV, Henderson S, Hoffmann P, McColl SR, Lockett T, et al. Butyrate-Induced Apoptosis in HCT116 Colorectal Cancer Cells Includes Induction of a Cell Stress Response. J Proteome Res. 2011 Apr;10(4):1860–9.
75. Pham CH, Lee JE, Yu J, Lee SH, Yu KR, Hong J, et al. Anticancer Effects of Propionic Acid Inducing Cell Death in Cervical Cancer Cells. Molecules. 2021 Aug 16;26(16):4951.
76. Wan L, Wen H, Li Y, Lyu J, Xi Y, Hoshii T, et al. ENL links histone acetylation to oncogenic gene expression in acute myeloid leukaemia. Nature. 2017 Mar 9;543(7644):265–9.
77. CCK-8 sigma - Google-søk [Internet]. [cited 2024 Jun 5]. Available from: https://www.google.com/search?client=safari&rls=en&q=CCK-8+sigma&ie=UTF-8&oe=UTF-8
78. Seahorse XF Cell Mito Stress Test Kit User Guide.
79. app5-300.gif 300 × 499 bildepunkter [Internet]. [cited 2024 May 29]. Available from: https://www.merckmillipore.com/INTERSHOP/static/WFS/Merck-Site/-/Merck/en_US/Freestyle/BI-Bioscience/Cell-Analysis/Muse/app5-300.gif
80. Zhang J, Yi M, Zha L, Chen S, Li Z, Li C, et al. Sodium Butyrate Induces Endoplasmic Reticulum Stress and Autophagy in Colorectal Cells: Implications for Apoptosis. Chang YJ, editor. PLOS ONE. 2016 Jan 19;11(1):e0147218.
81. FCCP Titration Protocol [Internet]. Agilent; Available from: https://www.agilent.com/cs/library/instructionsheet/public/is-fccp-optimization-5994-4807en-agilent.pdf
82. Tidwell TR, Røsland G, Tronstad KJ, Søreide K, Hagland HR. Comparing *in vitro* cytotoxic drug sensitivity in colon and pancreatic cancer using 2D and 3D cell models: contrasting viability and growth inhibition in clinically relevant dose and repeated drug cycles [Internet]. 2023 [cited 2024 May 29]. Available from: http://biorxiv.org/lookup/doi/10.1101/2023.11.22.568335
83. Oncel S, Safratowich BD, Lindlauf JE, Liu Z, Palmer DG, Briske-Anderson M, et al. Efficacy of Butyrate to Inhibit Colonic Cancer Cell Growth Is Cell Type-Specific and Apoptosis-Dependent. Nutrients. 2024 Feb 14;16(4):529.
84. Candido E. Sodium butyrate inhibits histone deacetylation in cultured cells. Cell. 1978 May;14(1):105–13.
85. Ryu TY, Kim K, Han TS, Lee MO, Lee J, Choi J, et al. Human gut-microbiome-derived propionate coordinates proteasomal degradation via HECTD2 upregulation to target EHMT2 in colorectal cancer. ISME J. 2022 May;16(5):1205–21.
86. Yu H, Li R, Huang H, Yao R, Shen S. Short-Chain Fatty Acids Enhance the Lipid Accumulation of 3T3-L1 Cells by Modulating the Expression of Enzymes of Fatty Acid Metabolism. Lipids. 2018 Jan;53(1):77–84.
87. Raudenská M, Masařík M, Peltanová B, Hönigová K, Navrátil J, Masařík M. Metabolic plasticity of cancer cells. Klin Onkol [Internet]. 2022 Jun 15 [cited 2024 May 20];35(3). Available from: https://www.linkos.cz/files/klinicka-onkologie/505/6064.pdf
88. Donohoe DR, Collins LB, Wali A, Bigler R, Sun W, Bultman SJ. The Warburg Effect Dictates the Mechanism of Butyrate-Mediated Histone Acetylation and Cell Proliferation. Mol Cell. 2012 Nov;48(4):612–26.
89. Ren Y, Shen HM. Critical role of AMPK in redox regulation under glucose starvation. Redox Biol. 2019 Jul;25:101154.
90. Ye Q, Zeng X, Wang S, Zeng X, Yang G, Ye C, et al. Butyrate drives the acetylation of histone H3K9 to activate steroidogenesis through PPARγ and PGC1α pathways in ovarian granulosa cells. FASEB J [Internet]. 2021 Feb [cited 2024 May 21];35(2). Available from: https://onlinelibrary.wiley.com/doi/10.1096/fj.202000444R

91. Klepinina L, Klepinin A, Truu L, Chekulayev V, Vija H, Kuus K, et al. Colon cancer cell differentiation by sodium butyrate modulates metabolic plasticity of Caco-2 cells via alteration of phosphotransfer network. Najbauer J, editor. PLOS ONE. 2021 Jan 20;16(1):e0245348.
92. He B, Lu C, Zheng G, He X, Wang M, Chen G, et al. Combination therapeutics in complex diseases. J Cell Mol Med. 2016 Dec;20(12):2231–40.
93. Koppula P, Zhang Y, Shi J, Li W, Gan B. The glutamate/cystine antiporter SLC7A11/xCT enhances cancer cell dependency on glucose by exporting glutamate. J Biol Chem. 2017 Aug;292(34):14240–9.
94. Hypoglycemia - Symptoms and causes - Mayo Clinic [Internet]. [cited 2024 Jun 13]. Available from: https://www.mayoclinic.org/diseases-conditions/hypoglycemia/symptoms-causes/syc-20373685
95. Donohoe DR, Holley D, Collins LB, Montgomery SA, Whitmore AC, Hillhouse A, et al. A Gnotobiotic Mouse Model Demonstrates That Dietary Fiber Protects against Colorectal Tumorigenesis in a Microbiota- and Butyrate-Dependent Manner. Cancer Discov. 2014 Dec 1;4(12):1387–97.

Appendices

Appendix A

Table 0.1 List of chemicals used in cell culture.

Chemical	Supplier	Product Code
DMEM (Dulbecco's Modified Eagle's Media) without glucose, L- glutamine and sodium pyruvate	Corning	17-207-CV
Fetal Bovine Serum, heat inactivated	Biowest	S181H
Glucose Solution 1M	Corning	25-037-Cl
L-glutamine 100X	Corning	25-005-Cl
Phosphate Buffered Saline (PBS)	Biowest	L0616
PenStrep solution 100X	Biowest	L0022-020
Seahorse XF Media	Agilent Technologies	-
Trypsin 0.25%	Corning	25-053-Cl

Table 0.2 List of Culture Flask and Microplates

Product	Supplier
Microplate 96-well, PS, U-Bottom, Clear CELLSTAR	Greiner Bio-One
Seahorse XFe96 Cell Culture Microplate	Agilent Technologies
Seahorse XFp Cell Culture Miniplate	Agilent Technologies
T-75 Ventilated Cell Flask	Falcon

Table 0.3 Commercial Kits

Product	Supplier
BCA Protein Assay Kit	Thermo Fisher Scientific
Muse Count & Viability Kit	Luminex
Seahorse XF Cell Mito Stress Test Kit	Agilent Technologies

Table 0.4 List of Electronic Equipment

Product	Supplier
Muse Cell Analyzer	Merck Millipore
Seahorse XF Pro Analyzer	Agilent Technologies
Seahorse XFp Analyzer	Agilent Technologies
SMZ25 Stereo Microscope	Nikon
Spectramax Paradigm Multi-Mode Detection Platform	Molecular Devices

Table 0.5 List of Software

Product	Supplier
NIS Elements Imaging Software	Nikon
Seahorse Wave Dektop Software	Agilent Technologies
SoftMax Pro 6 Version 6.2	Molecular Devices

Table 0.6 List of Chemicals Used in Treatment

Product	Supplier	Product Code
5-Fluorouracil	EMD Millipore	343922-1GM
Calcein AM	Invitrogen	65-0853-78
Propidium Iodide	Sigma-Aldrich	1002957359
Sodium Butyrate	Sigma-Aldrich	1001974665
Sodium Propionate	Sigma-Aldrich	102579793

Appendix B

Table 0.7 Cell density determination CCK-8 absorbance data at 450 nm for HCT116.

Cell number	Mean absorbance	SD
0	0,42	0,02
5000	1,54	0,05
10000	2,36	0,12
15000	2,63	0,08
20000	2,71	0,14
25000	2,75	0,15
30000	2,90	0,16

Table 0.8 Cell density determination CCK-8 absorbance data at 450 nm for SW948.

Cell number	Mean absorbance	Standard deviation
0	0,19	0,01
5000	1,50	0,06
10000	1,84	0,02
15000	1,99	0,07
20000	2,17	0,08
25000	2,27	0,05
30000	2,30	0,13

Appendix C

Table 0.9 CCK-8 BA 48H data for HCT119 at a 10K cell density exposed to 0.5 mM glucose.

BA concentration (mM)	Absorbance value (450 nm)	Normalized to 0 mM control	Replicate mean	SD
1,00	1,336	94 %	105 %	11 %
	1,345	95 %		
	1,363	96 %		
	1,888	113 %		
	1,899	114 %		
	1,922	116 %		
1,50	1,067	73 %	98 %	19 %
	1,168	81 %		
	1,300	91 %		
	1,928	116 %		
	1,865	112 %		
	1,919	115 %		
2,00	1,044	72 %	91 %	22 %
	1,028	70 %		
	1,055	72 %		
	1,792	107 %		
	1,966	118 %		
	1,810	108 %		
3,00	0,906	61 %	86 %	24 %
	0,959	65 %		
	0,953	65 %		
	1,840	110 %		
	1,810	108 %		
	1,740	104 %		
4,00	0,841	56 %	81 %	29 %
	0,748	49 %		
	0,845	56 %		

	1,759	105 %		
	1,779	106 %		
	1,840	110 %		
5,00	0,707	46 %	75 %	28 %
	0,757	50 %		
	0,785	52 %		
	1,647	98 %		
	1,707	102 %		
	1,696	101 %		

Table 0.10 CCK-8 BA 48H data for HCT119 at a 10K cell density exposed to 5.0 mM glucose.

BA concentration (mM)	Absorbance value (450 nm)	Normalized to 0 mM control	Replicate mean	SD
1,00	3,367	99 %	98 %	3 %
	3,498	103 %		
	3,300	97 %		
	3,317	98 %		
	3,379	100 %		
	3,184	94 %		
1,50	3,170	93 %	95 %	2 %
	3,305	97 %		
	3,346	99 %		
	3,172	93 %		
	3,266	96 %		
	3,151	93 %		
2,00	3,302	97 %	94 %	3 %
	3,282	97 %		
	3,216	95 %		
	3,185	94 %		
	3,192	94 %		
	2,989	88 %		

3,00	3,165	93 %	92 %	4 %
	2,981	87 %		
	3,036	89 %		
	3,093	98 %		
	2,913	92 %		
	2,890	92 %		
4,00	3,146	92 %	90 %	4 %
	3,251	95 %		
	3,104	91 %		
	2,952	86 %		
	3,021	89 %		
	2,847	83 %		
5,00	3,034	89 %	85 %	3 %
	2,946	86 %		
	2,936	86 %		
	2,855	84 %		
	2,832	83 %		
	2,767	81 %		

Table 0.11 CCK-8 PA 48H data for HCT116 at a 10K cell density exposed to 0.5 mM glucose.

PA concentration (mM)	Absorbance value (450 nm)	Normalized to 0 mM control	Replicate mean	SD
5,00	1,422	101 %	111 %	13 %
	1,291	91 %		
	1,558	111 %		
	1,900	114 %		
	2,037	123 %		
	2,076	125 %		
10,00	1,356	96 %	102 %	10 %
	1,271	89 %		

	1,362	96 %		
	1,891	114 %		
	1,836	110 %		
	1,796	107 %		
15,00	1,271	89 %	94 %	7 %
	1,218	85 %		
	1,272	89 %		
	1,652	98 %		
	1,709	102 %		
	1,659	99 %		
25,00	1,272	89 %	82 %	4 %
	1,122	78 %		
	1,167	81 %		
	1,400	82 %		
	1,399	82 %		
	1,332	78 %		
35,00	1,081	74 %	67 %	6 %
	0,978	67 %		
	1,075	74 %		
	1,139	65 %		
	1,116	64 %		
	1,053	60 %		
50,00	0,927	63 %	58 %	11 %
	1,004	69 %		
	1,061	73 %		
	0,860	48 %		
	0,869	48 %		
	0,907	51 %		

Table 0.12 CCK-8 PA 48H data for HCT116 at a 10K cell density exposed to 5.0 mM glucose.

PA concentration (mM)	Absorbance value (450 nm)	Normalized to 0 mM control	Replicate mean	SD
1,00	3,473	102 %	100 %	1 %

	3,399	100 %		
	3,342	98 %		
	3,358	99 %		
	3,394	100 %		
	3,364	99 %		
1,50	3,256	96 %	93 %	4 %
	3,342	98 %		
	3,156	93 %		
	3,144	93 %		
	3,110	91 %		
	2,955	87 %		
2,00	3,200	94 %	87 %	4 %
	2,951	86 %		
	2,935	86 %		
	2,945	86 %		
	2,820	83 %		
	2,874	84 %		
3,00	2,452	71 %	76 %	8 %
	2,617	76 %		
	2,165	62 %		
	2,515	80 %		
	2,560	82 %		
	2,565	82 %		
4,00	2,621	76 %	69 %	4 %
	2,461	71 %		
	2,237	65 %		
	2,315	67 %		
	2,297	67 %		
	2,404	70 %		
5,00	1,721	49 %	52 %	2 %
	1,876	54 %		
	1,811	52 %		
	1,851	53 %		

	1,849	53 %		
	1,902	55 %		

Table 0.13 CCK-8 BA 48H data for SW948 at a 5K cell density exposed to 0.5 mM glucose.

BA concentration (mM)	Absorbance value (450 nm)	Normalized to 0 mM control	Replicate mean	SD
1,00	2,291	105 %	100 %	6 %
	2,249	103 %		
	2,372	109 %		
	1,308	95 %		
	1,316	95 %		
	1,298	94 %		
1,50	1,778	80 %	91 %	9 %
	2,015	92 %		
	1,754	79 %		
	1,367	99 %		
	1,326	96 %		
	1,338	97 %		
2,00	1,208	53 %	74 %	23 %
	1,144	50 %		
	1,267	56 %		
	1,333	97 %		
	1,326	96 %		
	1,256	91 %		
3,00	0,926	39 %	57 %	18 %
	0,965	41 %		
	0,936	40 %		
	1,067	75 %		
	1,010	71 %		
	1,034	73 %		
4,00	0,687	28 %	38 %	10 %

	0,689	28 %		
	0,710	29 %		
	0,710	47 %		
	0,707	47 %		
	0,715	47 %		
5,00	0,578	22 %	27 %	5 %
	0,580	23 %		
	0,599	23 %		
	0,547	34 %		
	0,513	31 %		
	0,504	31 %		

Table 0.14 CCK-8 BA 48H data for SW948 at a 5K cell density exposed to 5.0 mM glucose.

BA concentration (mM)	Absorbance value (450 nm)	Normalized to 0 mM control	Replicate mean	SD
1,00	2,288	71 %	81 %	14 %
	2,277	71 %		
	2,389	74 %		
	3,143	106 %		
	2,626	88 %		
	2,446	77 %		
1,50	2,020	62 %	66 %	4 %
	2,060	64 %		
	2,175	71 %		
	2,163	72 %		
	2,067	65 %		
	2,099	66 %		
2,00	1,861	57 %	62 %	6 %
	1,946	63 %		
	1,822	59 %		

	2,325	73 %		
	1,913	60 %		
	1,989	62 %		
3,00	1,257	39 %	43 %	5 %
	1,256	39 %		
	1,295	38 %		
	1,176	43 %		
	1,269	46 %		
	1,372	52 %		
4,00	0,780	22 %	26 %	4 %
	0,794	22 %		
	0,793	22 %		
	1,035	31 %		
	0,875	27 %		
	1,001	31 %		
5,00	0,676	18 %	24 %	7 %
	0,666	17 %		
	0,685	18 %		
	0,904	28 %		
	1,020	32 %		
	1,117	33 %		

Table 0.15 CCK-8 PA 48H data for SW948 at a 5K cell density exposed to 0.5 mM glucose.

PA concentration (mM)	Absorbance value (450 nm)	Normalized to 0 mM control	Replicate mean	SD
5,00	2,548	117 %	99 %	19 %
	2,540	117 %		
	2,467	114 %		
	1,134	81 %		
	1,135	81 %		

	1,197	86 %		
10,00	2,378	109 %	97 %	17 %
	2,559	118 %		
	2,406	111 %		
	1,168	84 %		
	1,145	82 %		
	1,122	80 %		
15,00	1,891	86 %	83 %	7 %
	2,020	92 %		
	1,986	90 %		
	1,075	76 %		
	1,127	80 %		
	1,068	76 %		
25,00	1,303	57 %	59 %	1 %
	1,301	57 %		
	1,294	57 %		
	0,874	60 %		
	0,869	60 %		
	0,870	60 %		
35,00	0,853	36 %	42 %	6 %
	0,820	34 %		
	1,042	45 %		
	0,677	44 %		
	0,721	48 %		
	0,720	48 %		
50,00	0,735	30 %	26 %	4 %
	0,691	28 %		
	0,760	31 %		
	0,426	24 %		

	0,394	22 %		
	0,382	21 %		

Table 0.16 CCK-8 PA 48H data for SW948 at a 5K cell density exposed to 5.0 mM glucose.

PA concentration (mM)	Absorbance value (450 nm)	Normalized to 0 mM control	Replicate mean	SD
1,00	3,034	96 %	91 %	8 %
	3,042	96 %		
	2,932	92 %		
	2,804	94 %		
	2,781	93 %		
	2,250	75 %		
1,50	2,963	93 %	91 %	11 %
	2,905	91 %		
	3,055	96 %		
	2,264	70 %		
	2,978	100 %		
	2,807	94 %		
2,00	2,591	81 %	67 %	15 %
	2,554	80 %		
	2,543	80 %		
	1,947	64 %		
	1,587	51 %		
	1,448	47 %		
3,00	1,833	56 %	46 %	14 %
	1,861	57 %		
	1,829	56 %		
	0,572	24 %		
	0,903	35 %		
	1,316	50 %		

4,00	1,348	40 %	23 %	16 %
	1,324	39 %		
	1,189	35 %		
	0,329	7 %		
	0,380	8 %		
	0,465	11 %		
5,00	0,762	21 %	18 %	8 %
	0,801	22 %		
	0,713	19 %		
	0,291	5 %		
	0,586	15 %		
	0,991	28 %		

Table 0.17 CCK-8 BA 48H data for Caco-2 at a 5K cell density exposed to 0.5 mM glucose.

BA concentration (mM)	Absorbance value (450 nm)	Normalized to 0 mM control	Replicate mean	SD
1,00	0,802	103 %	122 %	15 %
	0,857	111 %		
	0,847	110 %		
	0,623	131 %		
	0,644	137 %		
	0,651	139 %		
1,50	0,886	116 %	121 %	13 %
	0,868	113 %		
	0,839	109 %		
	0,649	138 %		
	0,645	137 %		
	0,567	115 %		
2,00	0,804	103 %	122 %	15 %
	0,866	113 %		

	0,888	116 %		
	0,638	135 %		
	0,594	123 %		
	0,664	142 %		
3,00	0,903	118 %	117 %	5 %
	0,872	114 %		
	0,844	109 %		
	0,599	124 %		
	0,584	120 %		
	0,572	116 %		
4,00	0,798	103 %	116 %	9 %
	0,888	116 %		
	0,886	116 %		
	0,552	111 %		
	0,595	123 %		
	0,609	127 %		
5,00	0,878	115 %	108 %	8 %
	0,806	104 %		
	0,764	98 %		
	0,584	120 %		
	0,542	108 %		
	0,525	103 %		

Table 0.18 CCK-8 BA 48H data for Caco-2 at a 5K cell density exposed to 5.0 mM glucose.

BA concentration (mM)	Absorbance value (450 nm)	Normalized to 0 mM control	Replicate mean	SD
1,00	1,524	81 %	76 %	15 %
	0,932	47 %		
	1,426	75 %		
	1,153	83 %		
	1,202	86 %		

	1,596	85 %		
1,50	1,446	76 %	71 %	14 %
	1,418	75 %		
	1,191	85 %		
	1,133	81 %		
	1,043	53 %		
	1,065	54 %		
2,00	1,358	71 %	58 %	18 %
	0,587	37 %		
	0,640	41 %		
	0,928	46 %		
	1,408	74 %		
	1,467	77 %		
3,00	0,853	58 %	63 %	20 %
	1,359	99 %		
	0,936	47 %		
	0,613	42 %		
	1,091	70 %		
	0,690	65 %		
4,00	0,960	67 %	56 %	14 %
	0,855	42 %		
	1,171	60 %		
	0,976	49 %		
	1,094	78 %		
	0,647	42 %		
5,00	0,956	48 %	48 %	13 %
	0,906	45 %		
	0,964	48 %		
	0,828	57 %		
	0,948	66 %		
	0,584	27 %		

Table 0.19 CCK-8 PA 48H data for Caco-2 at a 5K cell density exposed to 0.5 mM glucose.

PA concentration (mM)	Absorbance value (450 nm)	Normalized to 0 mM control	Replicate mean	SD
5,00	0,693	87 %	106 %	16 %
	0,735	93 %		
	0,768	98 %		
	0,618	129 %		
	0,562	113 %		
	0,565	114 %		
10,00	0,760	97 %	98 %	10 %
	0,704	89 %		
	0,682	85 %		
	0,557	112 %		
	0,542	108 %		
	0,510	99 %		
15,00	0,673	84 %	97 %	13 %
	0,688	86 %		
	0,711	90 %		
	0,532	105 %		
	0,522	102 %		
	0,574	117 %		
25,00	0,711	90 %	77 %	8 %
	0,681	85 %		
	0,617	76 %		
	0,413	71 %		
	0,414	71 %		
	0,418	72 %		
35,00	0,596	72 %	64 %	11 %
	0,595	72 %		
	0,628	77 %		
	0,369	58 %		
	0,347	52 %		

	0,347	52 %		
50,00	0,540	64 %	42 %	19 %
	0,503	59 %		
	0,471	54 %		
	0,269	30 %		
	0,257	26 %		
	0,232	19 %		

Table 0.20 CCK-8 PA 48H data for Caco-2 at a 5K cell density exposed to 5.0 mM glucose.

PA concentration (mM)	Absorbance value (450 nm)	Normalized to 0 mM control	Replicate mean	SD
1,00	1,447	76 %	78 %	18 %
	1,394	73 %		
	1,131	58 %		
	0,982	69 %		
	1,495	110 %		
	1,148	82 %		
1,50	0,936	47 %	77 %	28 %
	0,983	50 %		
	1,150	59 %		
	-			
	1,419	104 %		
	1,365	99 %		
2,00	1,162	60 %	63 %	30 %
	0,601	28 %		
	0,702	33 %		
	1,389	101 %		
	1,264	91 %		
	0,903	63 %		
3,00	0,569	26 %	52 %	28 %
	0,620	29 %		
	0,722	35 %		
	1,101	98 %		

	0,624	59 %		
	0,733	68 %		
4,00	0,627	29 %	44 %	26 %
	0,426	18 %		
	0,390	15 %		
	1,041	74 %		
	0,917	64 %		
	0,934	65 %		
5,00	0,192	4 %	23 %	18 %
	0,270	9 %		
	0,286	9 %		
	0,619	40 %		
	0,586	37 %		
	0,635	41 %		

Appendix D

Table 0.21 HCT116 XF Cell Mito Stress Test 15-30K Cell Density Optimization data with 0.5 uM FCCP.

Time (minutes)	15k		25k		30k	
	Mean	Std Dev	Mean	Std Dev	Mean	Std Dev
1,59	334,61	61,21	534,68	0,00	260,64	31,74
8,18	306,62	59,87	501,57	0,00	231,22	30,41
14,76	296,89	63,81	488,69	0,00	225,30	25,33
21,43	134,00	11,80	168,43	0,00	203,44	58,43
28,02	123,10	9,19	156,32	0,00	215,62	78,50
34,61	118,14	9,60	148,55	0,00	234,08	111,40
41,28	272,30	76,12	551,44	0,00	217,15	51,30
47,88	226,67	33,38	468,52	0,00	206,05	50,16
54,47	218,22	29,61	434,28	0,00	208,91	46,72
61,16	88,33	4,11	125,25	0,00	200,90	104,98
67,77	85,06	1,45	118,61	0,00	228,41	166,13
74,38	83,18	2,27	114,85	0,00	258,89	224,65

Table 0.22 SW948 XF Cell Mito Stress Test FCCP Titration and Cell Density Optimization data.

Time (minutes)		1,54	8,37	15,19	22,11	28,94	35,76	42,67	49,50	56,33	63,25	70,08	76,92
SW948 10k 0 uM	Mean	144,46	149,56	146,04	78,42	57,45	53,12	54,22	53,99	54,53	34,32	30,47	28,20
	Std Dev	24,05	28,98	28,64	17,28	11,18	9,97	7,35	6,32	5,19	3,39	2,64	2,48
SW948 15k 0 uM	Mean	362,46	379,37	368,53	209,31	156,19	138,29	133,88	124,95	125,30	80,01	66,52	61,90
	Std Dev	126,78	140,02	138,42	94,03	73,62	67,14	59,33	51,69	48,79	31,92	25,44	23,24
SW948 10k 0.125 uM	Mean	147,87	159,17	155,37	95,51	68,74	62,75	101,25	93,05	90,50	43,27	38,75	36,77
	Std Dev	19,17	21,76	23,71	7,86	4,24	4,57	12,00	9,18	7,85	4,19	2,55	2,96
SW948 15k 0.125 uM	Mean	304,40	312,44	297,99	157,44	115,69	104,25	198,54	174,34	163,23	76,35	63,52	59,96
	Std Dev	120,73	118,11	111,92	58,55	45,41	42,94	85,42	71,82	66,10	33,09	27,70	26,57
SW948 10k 0.25 uM	Mean	119,45	121,61	117,00	62,16	49,38	46,32	93,54	79,10	75,85	35,11	30,37	29,02
	Std Dev	5,92	4,79	3,55	4,09	2,89	2,13	4,38	2,04	4,13	1,97	0,23	0,58
SW948 15k 0.25 uM	Mean	278,58	312,52	300,62	139,77	108,04	101,25	256,93	213,14	195,05	74,75	60,87	58,07
	Std Dev	44,80	52,83	48,87	22,38	16,52	12,52	31,95	21,39	18,23	11,82	8,44	8,18
SW948 10k 0.5 uM	Mean	91,00	93,62	91,06	45,71	36,00	34,93	85,37	65,19	62,72	27,11	23,87	23,20
	Std Dev	7,79	9,32	8,64	2,71	2,95	2,84	6,05	7,22	5,26	2,16	1,63	1,60
SW948 15k 0.5 uM	Mean	164,11	174,88	168,79	89,15	67,66	61,18	173,14	134,48	123,30	44,42	37,97	35,87
	Std Dev	29,45	40,49	39,48	23,09	15,43	13,39	40,26	29,06	26,67	10,07	7,61	6,83
SW948 10k 1.0 uM	Mean	118,77	119,35	116,23	58,74	46,49	44,76	110,48	87,91	82,36	33,64	29,88	28,56
	Std Dev	3,33	6,16	5,15	7,16	2,49	1,74	3,01	4,17	3,90	2,61	1,41	2,28
SW948 15k 1.0 uM	Mean	250,17	266,33	258,75	138,20	103,13	92,44	251,95	194,37	179,67	65,56	55,39	51,99
	Std Dev	80,84	74,80	72,45	44,17	29,50	26,35	71,24	54,45	51,22	18,11	15,32	14,37
SW948 10k 2.0 uM	Mean	107,32	119,84	118,64	68,42	51,07	48,35	96,63	77,85	72,26	34,46	31,01	29,14
	Std Dev	25,75	32,50	32,06	20,05	12,00	10,43	28,66	22,16	20,17	6,47	5,47	5,88
SW948 15k 2.0 uM	Mean	330,17	323,84	316,44	173,84	121,92	116,73	278,68	216,82	199,92	79,96	68,06	64,88
	Std Dev	201,04	195,79	192,96	92,19	67,94	65,42	167,98	130,02	119,57	42,94	38,15	36,51

Table 0.23 Caco-2 XF Cell Mito Stress Test FCCP Titration at 5K Cell Density data.

Time (minutes)	0 uM FCCP		0,125 uM FCCP		0,25 uM FCCP		0,5 uM FCCP		1,0 uM FCCP		2,0 uM FCCP	
	Mean	Std Dev	Mean	Std Dev	Mean	Std Dev	Mean	Std Dev	Mean	Std Dev	Mean	Std Dev
1,59	203,52	0,00	149,89	0,00	276,34	0,00	184,42	0,00	193,94	0,00	114,78	0,00

8,18	181,53	0,00	131,81	0,00	234,66	0,00	163,55	0,00	173,86	0,00	106,55	0,00
14,77	173,33	0,00	126,18	0,00	216,97	0,00	156,45	0,00	164,59	0,00	103,04	0,00
21,44	92,52	0,00	84,73	0,00	131,73	0,00	93,39	0,00	106,27	0,00	63,27	0,00
28,04	86,51	0,00	72,17	0,00	117,50	0,00	83,36	0,00	98,09	0,00	60,81	0,00
34,63	80,98	0,00	70,24	0,00	112,39	0,00	78,27	0,00	91,70	0,00	58,79	0,00
41,3	71,40	0,00	96,73	0,00	157,55	0,00	108,81	0,00	120,61	0,00	80,46	0,00
47,9	75,22	0,00	96,74	0,00	153,54	0,00	106,86	0,00	118,12	0,00	85,66	0,00
54,49	74,76	0,00	93,35	0,00	147,28	0,00	104,24	0,00	114,35	0,00	75,92	0,00
61,17	49,08	0,00	53,58	0,00	82,08	0,00	50,86	0,00	66,82	0,00	39,67	0,00
67,77	45,08	0,00	47,52	0,00	78,71	0,00	47,02	0,00	63,95	0,00	42,71	0,00
74,37	41,50	0,00	44,85	0,00	93,54	0,00	46,60	0,00	55,08	0,00	39,69	0,00

Appendix E

Table 0.24 XF Cell Mito Stress Test HCT116 Mitochondrial Respiration with 0,5 uM FCCP and a 15K cell density after BA singular treatments

Time (minutes)	HCT116 0 mM		HCT116 1.0 mM BA		HCT116 1.5 mM BA		HCT116 2.0 mM BA		HCT116 3 mM BA		HCT116 4 mM BA		HCT116 5 mM BA	
	Mean	Std Dev	Mean	Std Dev	Mean	Std Dev	Mean	Std Dev	Mean	Std Dev	Mean	Std Dev	Mean	Std Dev
1,56	293,66	59,72	248,10	33,86	320,06	0,56	287,71	8,01	250,93	16,24	206,82	2,99	153,37	0,23
8,41	274,73	6,35	250,36	26,23	356,09	5,65	322,82	1,98	275,44	20,56	231,39	9,21	178,92	14,20
15,26	220,96	10,89	249,40	33,24	350,58	12,26	315,78	5,60	266,68	23,41	225,13	11,48	175,96	18,65
22,21	149,37	6,31	138,76	15,35	212,75	27,57	176,34	15,33	161,50	13,16	131,44	15,50	117,64	18,59
29,07	123,06	12,81	121,32	16,46	180,32	14,66	151,59	15,47	140,10	12,30	117,28	12,65	99,16	13,06
35,93	116,80	11,48	120,87	18,05	172,78	14,42	145,59	10,52	134,36	8,80	114,57	11,66	94,87	8,58
42,88	143,80	9,79	325,09	47,80	429,73	28,06	410,39	41,61	381,81	64,47	338,67	13,37	249,11	44,02
49,75	130,23	11,05	267,15	38,21	337,27	22,15	315,29	28,96	295,12	44,85	252,28	15,90	198,46	44,16
56,61	125,84	10,04	250,92	39,17	310,75	20,67	289,16	23,38	267,08	37,46	227,04	14,76	177,28	41,07
63,56	108,06	9,20	113,21	13,17	140,79	6,74	130,25	5,31	124,48	6,85	101,28	12,34	79,32	10,72
70,42	95,06	9,67	100,25	15,92	127,59	10,24	113,69	4,10	101,55	3,79	90,30	17,26	68,65	9,75
77,28	97,81	13,42	96,61	13,78	118,53	10,09	103,73	5,74	93,18	3,51	81,25	11,35	62,62	10,04

Table 0.25 XF Cell Mito Stress Test SW948 Mitochondrial Respiration with 0.5 uM FCCP and a 15K cell density after BA singular treatments

Time (minutes)	SW948 0 mM		SW948 1.0 mM BA		SW948 1.5 mM BA		SW948 2.0 mM BA		SW948 3.0 mM BA		SW948 4.0 mM BA		SW948 5.0 mM BA	
	Mean	Std Dev	Mean	Std Dev	Mean	Std Dev	Mean	Std Dev	Mean	Std Dev	Mean	Std Dev	Mean	Std Dev
1,56	943,89	140,67	255,78	33,40	374,02	96,33	358,10	16,94	325,99	0,00	450,71	99,02	248,55	18,19
8,41	927,98	68,37	295,06	18,92	444,90	123,68	407,08	2,30	341,04	0,00	455,44	88,11	268,40	19,04
15,26	885,06	43,79	289,18	17,06	439,66	123,96	399,19	3,34	336,37	0,00	462,78	60,92	260,89	21,09
22,21	554,12	0,79	162,75	8,78	262,20	84,15	247,56	0,96	194,50	0,00	359,24	3,67	192,35	9,54
29,07	405,35	50,95	117,53	1,53	190,62	51,30	186,51	2,01	165,25	0,00	277,17	35,51	155,16	17,97
35,93	362,95	52,43	107,99	7,14	175,25	50,28	185,63	19,08	156,22	0,00	236,33	34,12	148,59	20,04
42,88	858,16	21,07	402,97	122,42	850,70	307,39	670,83	124,44	496,42	0,00	507,54	103,51	294,71	43,18
49,75	791,58	26,74	348,26	11,35	611,38	194,09	561,55	33,95	450,78	0,00	481,90	127,97	253,97	33,88
56,61	733,25	55,42	327,34	5,09	547,16	178,95	506,02	6,60	365,96	0,00	472,69	83,07	230,55	22,69
63,56	319,06	30,77	104,71	12,37	220,33	79,05	195,00	11,42	168,53	0,00	286,50	50,10	148,00	30,96
70,42	260,71	27,32	92,57	4,54	163,89	49,14	159,62	4,05	135,29	0,00	193,87	54,89	125,02	21,24
77,28	233,78	11,53	83,77	6,35	147,03	44,96	146,80	3,60	128,81	0,00	161,44	32,58	112,56	18,89

Table 0.26 XF Cell Mito Stress Test Caco-2 Mitochondrial Respiration with 0.25 uM FCCP and a 5K cell density after BA singular treatments.

Time (minutes)	0 mM		1,0 mM BA		1,5 mM BA		2,0 mM BA		3,0 mM BA		4,0 mM BA		5,0 mM BA	
	Mean	Std Dev	Mean	Std Dev	Mean	Std Dev	Mean	Std Dev	Mean	Std Dev	Mean	Std Dev	Mean	Std Dev
1,55	85,48	14,86	131,86	48,29	102,02	28,15	93,17	8,82	41,63	14,14	61,37	2,56	132,53	15,34
8,42	93,95	9,80	146,69	51,81	105,46	24,94	105,27	11,34	40,36	14,70	65,22	4,01	138,16	15,64
15,29	90,70	6,78	143,69	47,97	98,04	25,38	101,48	12,42	38,29	13,14	63,13	4,94	132,69	14,82
22,24	51,44	4,38	85,21	30,25	54,99	8,96	57,20	6,62	22,83	5,98	42,08	9,89	66,30	8,58
29,11	41,86	2,61	68,42	22,77	46,39	7,96	49,17	5,24	20,08	6,42	34,08	5,99	59,35	7,87
35,97	40,17	2,97	63,43	20,02	44,07	7,94	46,87	5,05	21,18	6,19	32,83	6,19	57,05	7,57
42,91	55,21	5,28	80,52	27,68	57,19	12,50	59,14	3,20	22,42	7,02	40,42	5,68	76,88	9,08
49,78	47,79	8,00	72,30	26,01	50,30	10,01	53,30	4,22	21,09	6,25	35,79	5,36	68,06	9,24
56,64	46,44	6,82	67,54	22,61	49,25	10,74	51,26	4,69	21,45	6,21	33,13	4,36	64,41	8,54
63,59	29,99	2,36	49,88	17,80	33,44	5,89	34,99	1,96	13,22	4,29	23,86	5,29	40,14	3,13
70,46	24,92	3,19	40,96	14,79	27,65	4,98	30,03	3,55	11,12	3,33	19,91	3,85	34,64	3,06
77,33	23,94	2,61	39,20	14,69	27,02	4,07	28,63	3,94	11,25	3,50	19,59	3,78	33,25	2,96

Table 0.27 XF Cell Mito Stress Test HCT116 Mitochondrial Respiration with 0,5 uM FCCP and a 15K cell density after PA singular treatments.

Time (minutes)	HCT116 0 mM		HCT116 5 mM PA		HCT116 10 mM PA		HCT116 15 mM PA		HCT116 25 mM PA		HCT116 35 mM PA		HCT116 50 mM PA	
	Mean	Std Dev	Mean	Std Dev	Mean	Std Dev	Mean	Std Dev	Mean	Std Dev	Mean	Std Dev	Mean	Std Dev
1,56	293,66	59,72	258,79	35,19	207,47	33,79	112,28	15,91	195,08	50,51	57,64	20,27	26,83	1,68
8,41	274,73	6,35	271,26	12,73	213,90	26,18	113,67	14,04	186,49	37,38	54,17	19,20	25,76	10,70
15,26	220,96	10,89	242,67	17,42	216,15	34,97	112,79	11,19	174,17	37,44	48,26	17,43	22,66	11,41
22,21	149,37	6,31	152,88	29,49	129,97	6,42	73,88	9,59	125,98	29,12	39,64	20,51	14,63	9,94
29,07	123,06	12,81	126,32	24,94	110,84	3,63	66,96	5,90	109,76	26,31	47,35	38,42	12,05	7,79
35,93	116,80	11,48	116,72	22,19	111,00	2,71	67,77	7,31	105,32	23,29	31,60	17,15	11,32	10,09
42,88	143,80	9,79	217,24	58,91	263,32	8,37	140,17	21,80	131,66	23,50	35,19	19,71	13,56	14,04
49,75	130,23	11,05	176,45	44,52	207,68	13,40	107,80	19,85	103,34	27,58	25,57	13,17	13,08	10,72
56,61	125,84	10,04	164,54	39,74	194,48	13,64	107,70	17,05	98,36	24,71	19,90	9,67	9,51	10,79
63,56	108,06	9,20	111,22	14,72	105,42	1,09	53,01	9,85	72,40	31,75	20,18	13,29	9,34	11,12
70,42	95,06	9,67	89,41	16,19	78,67	4,56	52,41	6,49	63,58	12,91	16,53	7,79	9,16	10,02
77,28	97,81	13,42	84,35	15,51	74,17	1,44	50,57	5,24	63,76	16,80	13,18	8,25	7,39	11,04

Table 0.28 XF Cell Mito Stress Test SW948 Mitochondrial Respiration with 0,5 uM FCCP and a 15K cell density after PA singular treatments.

Time (minutes)	SW948 0 mM		SW948 5 mM PA		SW948 10 mM PA		SW948 15 mM PA		SW948 25 mM PA		SW948 35 mM PA		SW948 50 mM PA	
	Mean	Std Dev	Mean	Std Dev	Mean	Std Dev	Mean	Std Dev	Mean	Std Dev	Mean	Std Dev	Mean	Std Dev
1,56	943,89	140,67	372,17	74,52	260,15	31,16	226,28	50,75	164,27	48,91	87,01	8,48	80,91	48,41
8,41	927,98	68,37	382,81	69,09	275,09	56,05	259,01	61,41	192,63	59,66	92,90	2,07	67,66	39,04
15,26	885,06	43,79	380,97	98,50	259,24	67,87	251,04	56,44	190,35	59,67	88,54	1,56	61,61	38,46
22,21	554,12	0,79	228,46	25,12	169,89	41,45	161,70	40,43	135,46	45,75	58,69	4,81	39,06	22,04
29,07	405,35	50,95	167,73	16,43	127,09	30,06	118,86	24,92	97,70	30,79	50,45	4,77	29,68	11,69
35,93	362,95	52,43	154,75	16,26	117,49	29,20	110,05	23,83	90,56	28,80	48,06	6,27	29,77	12,19
42,88	858,16	21,07	315,84	69,13	221,47	62,67	279,48	74,74	226,97	90,52	81,22	12,74	52,49	35,93
49,75	791,58	26,74	274,63	60,14	192,00	56,95	228,02	58,91	186,31	66,33	68,37	0,85	44,30	29,73
56,61	733,25	55,42	257,00	52,08	185,35	59,85	210,66	52,05	170,95	59,63	65,22	2,24	46,31	29,80
63,56	319,06	30,77	128,73	14,40	103,28	27,80	103,07	20,84	87,58	31,08	39,70	2,06	21,40	10,49
70,42	260,71	27,32	107,42	17,17	83,64	18,50	83,55	18,13	70,36	22,95	37,09	0,35	19,47	8,70
77,28	233,78	11,53	99,72	17,59	78,25	18,16	78,65	18,24	65,70	22,01	33,11	0,32	19,38	3,92

Table 0.29 XF Cell Mito Stress Test Caco-2 Mitochondrial Respiration with 0.25 uM FCCP and a 5K cell density after PA singular treatments.

Time (minutes)	0 mM		5,0 mM PA		10 mM PA		15 mM PA		25 mM PA		35 mM PA		50 mM PA	
	Mean	Std Dev	Mean	Std Dev	Mean	Std Dev	Mean	Std Dev	Mean	Std Dev	Mean	Std Dev	Mean	Std Dev
1,55	85,48	14,86	65,70	11,93	32,41	2,38	41,04	10,35	80,87	20,97	64,37	15,24	13,18	5,06
8,42	93,95	9,80	73,90	11,32	33,14	4,40	43,18	10,33	78,75	21,36	62,96	14,65	12,14	4,31
15,29	90,70	6,78	70,29	11,08	31,34	4,59	41,75	11,34	72,78	21,62	58,79	14,53	10,89	3,94
22,24	51,44	4,38	38,76	4,42	18,17	3,09	28,03	5,23	43,82	12,31	40,09	14,04	6,92	2,53
29,11	41,86	2,61	32,57	4,37	15,41	1,21	22,49	5,48	43,18	15,08	33,84	10,23	5,82	2,44
35,97	40,17	2,97	31,76	3,63	15,87	1,03	22,63	6,76	37,06	7,50	32,29	8,65	6,15	2,65
42,91	55,21	5,28	40,92	5,83	16,99	1,35	22,95	7,72	48,07	19,69	32,88	11,78	4,90	2,41
49,78	47,79	8,00	36,04	4,67	15,70	2,37	21,92	8,80	38,44	12,75	29,38	9,74	4,96	1,61
56,64	46,44	6,82	34,28	4,47	15,19	1,70	20,56	7,11	35,80	11,42	27,89	7,13	4,45	1,47
63,59	29,99	2,36	22,04	2,00	11,03	1,81	15,50	4,02	23,27	7,58	17,07	4,56	2,09	1,39
70,46	24,92	3,19	18,97	2,06	9,35	2,02	13,60	3,28	19,76	5,20	14,51	2,13	2,36	1,26
77,33	23,94	2,61	18,37	1,86	9,14	1,60	12,66	2,26	19,57	4,46	14,66	3,40	1,61	1,69

Table 0.30 XF Cell Mito Stress Test HCT116 Mitochondrial Parameters with 0,5 uM FCCP and a 15K cell density after BA and PA singular treatments.

	Basal Respiration		Proton Leak		Spare Respiratory Capacity		ATP-Production Coupled Respiration	
Group	**Value**	**Std Dev**	**Value**	**Std Dev**	**Value**	**Std Dev**	**Value**	**Std Dev**
BA								
0 mM	125,90	17,62	21,74	4,27	0,00	0,00	104,17	16,72
1.0 mM	152,79	21,92	24,26	7,69	75,70	23,09	128,53	15,28
1.5 mM	232,05	2,18	52,95	3,80	68,51	21,54	161,64	28,03
2.0 mM	212,05	0,14	35,91	10,85	78,84	37,35	145,03	43,72
3.0 mM	173,50	19,90	36,30	9,24	94,60	45,91	114,39	32,74
4.0 mM	143,88	0,13	32,14	2,05	105,30	14,33	99,81	18,61
5.0 mM	124,39	20,09	37,12	8,51	77,28	19,31	87,27	12,85
PA								
0 mM	125,90	17,62	21,74	4,27	0,00	0,00	104,17	16,72
5 mM	158,32	32,93	40,30	14,52	2,55	2,21	172,28	85,01
10 mM	125,01	39,07	32,16	7,95	31,45	33,10	92,85	34,80
15 mM	62,22	6,06	16,38	1,24	27,38	14,84	45,84	5,31
25 mM	110,59	25,13	41,74	15,49	0,00	0,00	68,85	18,92
35 mM	35,07	9,18	18,42	9,39	0,00	0,00	16,65	4,38
50 mM	15,27	0,36	3,93	0,96	0,00	0,00	11,34	1,32

Table 0.31 XF Cell Mito Stress Test SW948 Mitochondrial Parameters Parameters with 0,5 uM FCCP and a 15K cell density after BA and PA singular treatments.

	Basal Respiration		Proton Leak		Spare Respiratory Capacity		ATP-Production Coupled Respiration	
Group	**Value**	**Std Dev**	**Value**	**Std Dev**	**Value**	**Std Dev**	**Value**	**Std Dev**
BA								
0 mM	555,57	170,32	90,24	14,15	18,46	18,22	443,00	153,00
1.0 mM	205,42	10,71	37,69	23,34	210,09	193,78	251,57	122,10
1.5 mM	289,73	56,09	29,03	4,01	466,84	161,75	260,70	52,49
2.0 mM	311,05	101,60	46,34	17,00	332,96	139,44	264,71	89,29
3.0 mM	370,57	230,54	46,24	13,88	278,80	353,47	216,22	241,94
4.0 mM	301,34	93,50	74,89	1,54	44,76	42,59	226,45	95,04
5.0 mM	148,33	32,07	36,03	8,33	38,64	40,76	112,29	27,02
PA								
0 mM	555,57	170,32	90,24	14,15	18,46	18,22	443,00	153,00
5 mM	235,34	21,29	55,03	8,42	0,00	0,00	226,23	85,12
10 mM	180,99	49,84	39,24	11,10	0,00	0,00	141,75	38,74
15 mM	172,39	38,20	31,41	5,59	28,44	18,30	140,99	32,61
25 mM	124,65	37,76	24,86	6,80	37,30	32,35	99,79	31,11
35 mM	55,44	1,24	24,91	17,76	30,73	50,84	89,07	84,21
50 mM	42,24	34,54	10,30	7,77	0,00	0,00	31,93	26,77

Table 0.32 XF Cell Mito Stress Test Caco-2 Mitochondrial Parameters with 0.25 uM FCCP and a 5K cell density after BA and PA singular treatments

	Basal Respiration		Proton Leak		Spare Respiratory Capacity		ATP-Production Coupled Respiration	
BA								
Group	**Value**	**Std Dev**	**Value**	**Std Dev**	**Value**	**Std Dev**	**Value**	**Std Dev**
0 mM	66,75	4,19	16,22	1,67	0,00	0,00	50,53	4,41
1.0 mM	127,26	53,02	33,80	19,64	0,00	0,00	93,46	34,92
1.5 mM	71,02	21,32	17,05	3,87	0,00	0,00	53,97	17,46
2.0 mM	72,48	15,96	17,73	3,07	0,00	0,00	54,75	12,99
3.0 mM	27,17	9,96	8,96	3,23	0,00	0,00	18,21	6,74
4.0 mM	54,73	12,88	16,17	3,98	0,00	0,00	38,55	9,27
5.0 mM	99,44	11,99	23,79	4,60	0,00	0,00	75,65	7,69
PA								
0 mM	66,75	4,19	16,22	1,67	0,00	0,00	50,53	4,41
5 mM	51,91	9,27	13,40	1,82	0,00	0,00	38,52	7,58
10 mM	22,21	3,01	6,27	1,13	0,00	0,00	15,94	3,76
15 mM	29,09	9,32	9,83	3,22	0,00	0,00	19,27	6,68
25 mM	53,21	17,18	17,50	3,22	0,00	0,00	35,72	14,55
35 mM	44,28	12,71	17,80	6,98	0,00	0,00	26,49	5,96
50 mM	9,29	4,62	4,21	2,18	0,00	0,00	5,08	2,69

Appendix F

Table 0.33 HCT116 10K cell density, 0,5 mM glucose combinatorial BA + PA 48H data

PA+BA concentration (mM)	Absorbance value (450 nm)	Normalized to 0 mM control	Replicate mean	SD
5+1	1,400	99 %	89 %	10 %
	1,353	95 %		
	1,360	96 %		
	1,439	85 %		
	1,456	86 %		
	1,265	73 %		
5+1,5	1,173	82 %	80 %	8 %
	1,258	88 %		
	1,300	91 %		
	1,266	74 %		
	1,293	75 %		
	1,221	71 %		
5+2	1,178	82 %	77 %	7 %
	1,193	83 %		
	1,188	83 %		
	1,274	74 %		
	1,164	67 %		
	1,226	71 %		
5+3	1,108	77 %	68 %	8 %
	1,058	73 %		
	1,082	75 %		
	1,153	66 %		
	0,981	55 %		
	1,115	64 %		
5+4	0,978	67 %	65 %	6 %

	1,026	70 %		
	1,032	71 %		
	1,100	63 %		
	1,119	64 %		
	0,982	55 %		
5+5	0,969	66 %	61 %	7 %
	0,981	67 %		
	0,989	67 %		
	1,006	57 %		
	0,911	51 %		
	0,982	55 %		
10+1	1,057	73 %	68 %	10 %
	1,111	77 %		
	1,120	77 %		
	1,212	70 %		
	0,940	53 %		
	1,038	59 %		
10+1,5	1,034	71 %	64 %	10 %
	1,042	71 %		
	1,106	76 %		
	0,945	53 %		
	0,982	55 %		
	0,980	55 %		
10+2	0,930	63 %	63 %	7 %
	1,021	70 %		
	1,042	71 %		
	1,062	60 %		
	1,005	57 %		
	0,966	54 %		
10+3	0,930	63 %	56 %	9 %
	0,953	65 %		
	0,969	66 %		
	0,874	48 %		

	0,906	51 %		
	0,834	46 %		
10+4	0,861	58 %	59 %	3 %
	0,839	56 %		
	0,954	65 %		
	1,023	58 %		
	1,027	58 %		
	1,006	57 %		
10+5	0,947	64 %	56 %	7 %
	0,921	62 %		
	0,880	59 %		
	0,934	52 %		
	0,838	46 %		
	0,898	50 %		
15+1	0,845	56 %	58 %	6 %
	0,876	59 %		
	0,998	68 %		
	1,073	61 %		
	0,942	53 %		
	0,913	51 %		
15+1,5	0,968	66 %	59 %	9 %
	0,983	67 %		
	1,003	68 %		
	0,865	48 %		
	0,963	54 %		
	0,903	50 %		
15+2	0,816	54 %	57 %	6 %
	0,872	58 %		
	0,983	67 %		
	1,035	59 %		
	0,935	52 %		
	0,928	52 %		
15+3	0,929	63 %	54 %	9 %

	0,895	60 %		
	0,873	59 %		
	0,932	52 %		
	0,932	52 %		
	0,722	39 %		
15+4	0,828	55 %	62 %	5 %
	0,901	61 %		
	0,952	65 %		
	1,041	59 %		
	1,075	61 %		
	1,186	68 %		
15+5	0,916	62 %	56 %	3 %
	0,841	56 %		
	0,787	52 %		
	0,963	54 %		
	0,968	54 %		
	1,012	57 %		
25+1	2,324	0,672	74 %	9 %
	2,352	0,681		
	2,203	0,635		
	2,845	0,834		
	2,863	0,840		
	2,713	0,794		
25+1,5	2,152	0,620	72 %	11 %
	2,227	0,643		
	2,150	0,619		
	2,871	0,842		
	2,794	0,818		
	2,716	0,795		
25+2	2,120	0,610	73 %	8 %
	2,353	0,681		
	2,354	0,681		
	2,681	0,784		

	2,738	0,801		
	2,710	0,793		
25+3	2,156	0,621	68 %	13 %
	2,078	0,597		
	1,721	0,489		
	2,763	0,809		
	2,741	0,802		
	2,572	0,751		
25+4	1,845	0,526	68 %	9 %
	2,327	0,673		
	2,220	0,641		
	2,582	0,754		
	2,556	0,746		
	2,543	0,742		
25+5	2,029	0,582	66 %	13 %
	2,102	0,605		
	1,644	0,465		
	2,685	0,785		
	2,567	0,749		
	2,596	0,758		
35+1	1,574	0,444	63 %	12 %
	1,826	0,521		
	2,109	0,607		
	2,515	0,733		
	2,566	0,749		
	2,431	0,708		
35+1,5	1,783	0,507	61 %	17 %
	1,479	0,415		
	1,578	0,445		
	2,612	0,763		
	2,568	0,749		
	2,614	0,763		
35+2	1,517	0,426	61 %	14 %

	1,760	0,500		
	1,907	0,545		
	2,635	0,770		
	2,573	0,751		
	2,240	0,649		
35+3	1,704	0,483	60 %	14 %
	1,654	0,468		
	1,680	0,476		
	2,456	0,715		
	2,571	0,750		
	2,458	0,716		
35+4	1,588	0,448	61 %	14 %
	1,698	0,482		
	1,862	0,532		
	2,543	0,742		
	2,575	0,752		
	2,431	0,708		
35+5	1,571	0,443	56 %	13 %
	1,541	0,434		
	1,631	0,461		
	2,345	0,681		
	2,352	0,683		
	2,354	0,684		
50+1	1,443	0,404	52 %	12 %
	1,450	0,406		
	1,435	0,401		
	2,208	0,639		
	2,215	0,642		
	2,107	0,609		
50+1,5	1,198	0,329	44 %	11 %
	1,155	0,316		
	1,331	0,370		
	1,895	0,544		

	1,967	0,566		
	1,735	0,495		
50+2	1,177	0,323	46 %	14 %
	1,201	0,330		
	1,246	0,344		
	2,042	0,589		
	2,020	0,582		
	1,985	0,571		
50+3	1,150	0,315	46 %	15 %
	1,090	0,296		
	1,360	0,379		
	2,043	0,589		
	2,026	0,584		
	2,083	0,601		
50+4	1,000	0,269	44 %	14 %
	1,191	0,327		
	1,243	0,343		
	1,895	0,544		
	1,934	0,556		
	2,037	0,587		
50+5	1,267	0,350	44 %	15 %
	1,006	0,271		
	1,152	0,315		
	2,144	0,620		
	1,994	0,574		
	1,803	0,516		

Table 0.34 HCT116 10K cell density, 5,0 mM glucose combinatorial BA + PA 48H data

PA+BA concentration (mM)	Absorbance value (450 nm)	Normalized to 0 mM control	Replicate mean	SD
5+1	3,291	0,967	91 %	4 %
	3,199	0,939		

	3,093	0,907		
	3,061	0,900		
	3,101	0,912		
	2,931	0,860		
5+1,5	3,200	0,939	91 %	7 %
	3,337	0,981		
	3,322	0,976		
	2,935	0,862		
	3,002	0,882		
	2,767	0,810		
5+2	2,894	0,846	88 %	3 %
	3,181	0,933		
	3,033	0,888		
	2,982	0,876		
	2,970	0,872		
	2,914	0,855		
5+3	3,353	0,986	86 %	12 %
	3,110	0,912		
	3,279	0,963		
	2,758	0,807		
	2,685	0,785		
	2,334	0,678		
5+4	2,833	0,827	74 %	10 %
	2,752	0,803		
	2,757	0,804		
	2,577	0,752		
	2,368	0,688		
	1,985	0,571		
5+5	2,741	0,799	68 %	12 %
	2,661	0,775		
	2,703	0,788		
	1,882	0,540		
	1,962	0,564		

	2,047	0,590		
10+1	2,926	0,856	80 %	8 %
	3,082	0,903		
	2,833	0,827		
	2,649	0,774		
	2,427	0,706		
	2,468	0,719		
10+1,5	3,014	0,883	78 %	11 %
	3,004	0,880		
	3,004	0,880		
	2,236	0,648		
	2,476	0,721		
	2,298	0,667		
10+2	2,884	0,843	80 %	7 %
	2,886	0,844		
	3,028	0,887		
	2,531	0,738		
	2,519	0,734		
	2,582	0,754		
10+3	2,762	0,806	76 %	9 %
	2,968	0,869		
	2,845	0,831		
	2,241	0,650		
	2,301	0,668		
	2,468	0,719		
10+4	2,881	0,842	74 %	11 %
	2,800	0,817		
	2,884	0,843		
	2,295	0,666		
	1,969	0,566		
	2,517	0,734		
10+5	2,630	0,766	74 %	8 %
	2,865	0,837		

	2,707	0,789		
	2,455	0,715		
	2,596	0,758		
	2,080	0,600		
15+1	2,836	0,828	71 %	17 %
	2,963	0,867		
	2,875	0,840		
	2,376	0,691		
	1,728	0,493		
	1,832	0,525		
15+1,5	2,850	0,833	71 %	14 %
	3,022	0,885		
	2,745	0,801		
	2,066	0,596		
	1,962	0,564		
	2,113	0,610		
15+2	2,800	0,817	72 %	14 %
	2,921	0,854		
	2,834	0,828		
	2,306	0,669		
	1,899	0,545		
	2,015	0,581		
15+3	2,738	0,798	68 %	15 %
	2,761	0,805		
	2,783	0,812		
	1,911	0,549		
	1,677	0,477		
	2,105	0,608		
15+4	2,772	0,809	65 %	19 %
	2,704	0,788		
	2,820	0,823		
	2,166	0,627		
	1,409	0,395		

	1,582	0,448		
15+5	2,890	0,845	62 %	21 %
	2,674	0,779		
	2,724	0,794		
	1,440	0,405		
	1,274	0,354		
	1,850	0,530		
25+1	2,324	0,672	74 %	9 %
	2,352	0,681		
	2,203	0,635		
	2,845	0,834		
	2,863	0,840		
	2,713	0,794		
25+1,5	2,152	0,620	72 %	11 %
	2,227	0,643		
	2,150	0,619		
	2,871	0,842		
	2,794	0,818		
	2,716	0,795		
25+2	2,120	0,610	73 %	8 %
	2,353	0,681		
	2,354	0,681		
	2,681	0,784		
	2,738	0,801		
	2,710	0,793		
25+3	2,156	0,621	68 %	13 %
	2,078	0,597		
	1,721	0,489		
	2,763	0,809		
	2,741	0,802		
	2,572	0,751		
25+4	1,845	0,526	68 %	9 %
	2,327	0,673		

	2,220	0,641		
	2,582	0,754		
	2,556	0,746		
	2,543	0,742		
25+5	2,029	0,582	66 %	13 %
	2,102	0,605		
	1,644	0,465		
	2,685	0,785		
	2,567	0,749		
	2,596	0,758		
35+1	1,574	0,444	63 %	12 %
	1,826	0,521		
	2,109	0,607		
	2,515	0,733		
	2,566	0,749		
	2,431	0,708		
35+1,5	1,783	0,507	61 %	17 %
	1,479	0,415		
	1,578	0,445		
	2,612	0,763		
	2,568	0,749		
	2,614	0,763		
35+2	1,517	0,426	61 %	14 %
	1,760	0,500		
	1,907	0,545		
	2,635	0,770		
	2,573	0,751		
	2,240	0,649		
35+3	1,704	0,483	60 %	14 %
	1,654	0,468		
	1,680	0,476		
	2,456	0,715		
	2,571	0,750		

	2,458	0,716		
35+4	1,588	0,448	61 %	14 %
	1,698	0,482		
	1,862	0,532		
	2,543	0,742		
	2,575	0,752		
	2,431	0,708		
35+5	1,571	0,443	56 %	13 %
	1,541	0,434		
	1,631	0,461		
	2,345	0,681		
	2,352	0,683		
	2,354	0,684		
50+1	1,443	0,404	52 %	12 %
	1,450	0,406		
	1,435	0,401		
	2,208	0,639		
	2,215	0,642		
	2,107	0,609		
50+1,5	1,198	0,329	44 %	11 %
	1,155	0,316		
	1,331	0,370		
	1,895	0,544		
	1,967	0,566		
	1,735	0,495		
50+2	1,177	0,323	46 %	14 %
	1,201	0,330		
	1,246	0,344		
	2,042	0,589		
	2,020	0,582		
	1,985	0,571		
50+3	1,150	0,315	46 %	15 %
	1,090	0,296		

	1,360	0,379		
	2,043	0,589		
	2,026	0,584		
	2,083	0,601		
50+4	1,000	0,269	44 %	14 %
	1,191	0,327		
	1,243	0,343		
	1,895	0,544		
	1,934	0,556		
	2,037	0,587		
50+5	1,267	0,350	44 %	15 %
	1,006	0,271		
	1,152	0,315		
	2,144	0,620		
	1,994	0,574		
	1,803	0,516		

Table 0.35 Caco-2 5K cell density, 0,5 mM glucose combinatorial BA + PA 48H

PA+BA concentration (mM)	Absorbance value (450 nm)	Normalized to 0 mM control	Replicate mean	SD
5+1	0,692	74 %	66 %	7 %
	0,674	72 %		
	0,656	70 %		
	0,469	59 %		
	0,489	63 %		
	0,459	57 %		
5+1,5	0,663	71 %	66 %	6 %
	0,643	68 %		
	0,683	73 %		
	0,480	61 %		
	0,473	60 %		
	0,482	62 %		

5+2	0,638	67 %	72 %	5 %
	0,690	74 %		
	0,748	82 %		
	0,506	66 %		
	0,532	71 %		
	0,536	72 %		
5+3	0,743	81 %	65 %	13 %
	0,694	75 %		
	0,680	73 %		
	0,443	54 %		
	0,443	54 %		
	0,438	53 %		
5+4	0,640	68 %	68 %	9 %
	0,688	74 %		
	0,751	82 %		
	0,454	56 %		
	0,470	59 %		
	0,506	66 %		
5+5	0,699	75 %	57 %	16 %
	0,626	66 %		
	0,652	69 %		
	0,418	49 %		
	0,383	42 %		
	0,356	37 %		
10+1	0,655	70 %	69 %	7 %
	0,668	71 %		
	0,745	81 %		
	0,497	65 %		
	0,516	68 %		
	0,474	60 %		
10+1,5	0,738	80 %	62 %	12 %
	0,616	65 %		
	0,664	71 %		

	0,467	59 %		
	0,408	47 %		
	0,424	50 %		
10+2	0,628	66 %	70 %	6 %
	0,672	72 %		
	0,738	80 %		
	0,497	65 %		
	0,521	69 %		
	0,499	65 %		
10+3	0,906	102 %	71 %	25 %
	0,798	88 %		
	0,809	89 %		
	0,457	57 %		
	0,401	46 %		
	0,392	44 %		
10+4	0,633	67 %	69 %	2 %
	0,667	71 %		
	0,647	69 %		
	0,530	71 %		
	0,515	68 %		
	0,502	66 %		
10+5	0,633	67 %	56 %	8 %
	0,576	60 %		
	0,538	55 %		
	0,472	60 %		
	0,419	49 %		
	0,398	45 %		
15+1	0,577	60 %	59 %	8 %
	0,639	68 %		
	0,639	68 %		
	0,473	60 %		
	0,450	55 %		
	0,398	45 %		

15+1,5	0,597	62 %	49 %	15 %
	0,637	67 %		
	0,556	57 %		
	0,353	37 %		
	0,353	37 %		
	0,340	34 %		
15+2	0,595	62 %	58 %	7 %
	0,607	63 %		
	0,618	65 %		
	0,456	57 %		
	0,411	48 %		
	0,425	51 %		
15+3	0,606	63 %	49 %	11 %
	0,570	59 %		
	0,532	54 %		
	0,372	40 %		
	0,357	37 %		
	0,359	38 %		
15+4	0,525	53 %	48 %	9 %
	0,558	57 %		
	0,546	56 %		
	0,424	50 %		
	0,366	39 %		
	0,344	35 %		
15+5	0,522	53 %	39 %	13 %
	0,512	51 %		
	0,487	48 %		
	0,322	31 %		
	0,290	24 %		
	0,298	26 %		
25+1	0,543	55 %	43 %	14 %
	0,543	55 %		
	0,547	56 %		

	0,327	32 %		
	0,318	30 %		
	0,308	28 %		
25+1,5	0,551	56 %	40 %	16 %
	0,516	52 %		
	0,540	55 %		
	0,296	26 %		
	0,307	28 %		
	0,286	24 %		
25+2	0,523	53 %	43 %	14 %
	0,552	56 %		
	0,559	57 %		
	0,351	36 %		
	0,307	28 %		
	0,310	28 %		
25+3	0,559	57 %	40 %	21 %
	0,602	63 %		
	0,566	58 %		
	0,281	23 %		
	0,255	18 %		
	0,277	22 %		
25+4	0,483	48 %	39 %	15 %
	0,491	49 %		
	0,563	58 %		
	0,332	33 %		
	0,312	29 %		
	0,255	18 %		
25+5	0,560	57 %	35 %	21 %
	0,544	55 %		
	0,499	50 %		
	0,264	19 %		
	0,228	12 %		
	0,244	15 %		

35+1	0,467	46 %	32 %	23 %
	0,526	53 %		
	0,573	59 %		
	0,263	19 %		
	0,248	16 %		
	0,172	1 %		
35+1,5	0,465	45 %	25 %	25 %
	0,525	53 %		
	0,472	46 %		
	0,186	4 %		
	0,172	1 %		
	0,166	0 %		
35+2	0,455	44 %	32 %	17 %
	0,446	43 %		
	0,522	53 %		
	0,291	25 %		
	0,286	24 %		
	0,195	6 %		
35+3	0,534	54 %	29 %	22 %
	0,506	51 %		
	0,440	42 %		
	0,235	14 %		
	0,206	8 %		
	0,190	5 %		
35+4	0,441	42 %	26 %	19 %
	0,411	38 %		
	0,474	46 %		
	0,257	18 %		
	0,236	14 %		
	0,157	-1 %		
35+5	0,476	47 %	21 %	23 %
	0,439	42 %		
	0,413	39 %		

	0,166	0 %		
	0,179	3 %		
	0,152	-2 %		
50+1	0,397	37 %	17 %	19 %
	0,359	32 %		
	0,373	34 %		
	0,173	2 %		
	0,174	2 %		
	0,139	-5 %		
50+1,5	0,360	32 %	13 %	20 %
	0,370	33 %		
	0,324	27 %		
	0,152	-2 %		
	0,135	-6 %		
	0,130	-7 %		
50+2	0,334	29 %	11 %	16 %
	0,303	25 %		
	0,278	21 %		
	0,156	-2 %		
	0,143	-4 %		
	0,143	-4 %		
50+3	0,307	25 %	9 %	17 %
	0,309	25 %		
	0,298	24 %		
	0,133	-6 %		
	0,132	-6 %		
	0,134	-6 %		
50+4	-		61 %	17 %
	0,516	52 %		
	0,438	42 %		
	0,560	77 %		
	0,586	82 %		
	0,498	65 %		

50+5	0,470	46 %	22 %	25 %
	0,448	43 %		
	0,466	45 %		
	0,157	-1 %		
	0,152	-2 %		
	0,174	2 %		

Table 0.36 Caco-2 5K cell density, 5,0 mM glucose combinatorial BA + PA 48H data

PA+BA concentration (mM)	Absorbance value (450 nm)	Normalized to 0 mM control	Replicate mean	SD
5+1	1,386	73 %	98 %	28 %
	1,346	70 %		
	1,426	75 %		
	1,767	132 %		
	1,700	126 %		
	1,493	110 %		
5+1,5	1,415	74 %	89 %	19 %
	1,350	71 %		
	1,379	72 %		
	1,492	110 %		
	1,340	97 %		
	1,478	109 %		
5+2	1,285	67 %	93 %	30 %
	1,329	69 %		
	1,350	71 %		
	1,916	144 %		
	1,392	102 %		
	1,412	103 %		
5+3	1,256	65 %	75 %	15 %
	1,298	68 %		
	1,098	56 %		
	1,318	96 %		

	1,209	87 %		
	1,124	80 %		
5+4	1,181	61 %	78 %	24 %
	1,161	60 %		
	1,199	62 %		
	1,424	104 %		
	1,528	113 %		
	1,008	71 %		
5+5	1,196	62 %	68 %	14 %
	1,163	60 %		
	1,016	51 %		
	1,252	90 %		
	1,018	72 %		
	1,067	76 %		
10+1	1,186	61 %	66 %	29 %
	0,834	41 %		
	0,719	34 %		
	1,358	99 %		
	1,399	102 %		
	0,840	58 %		
10+1,5	1,310	68 %	59 %	24 %
	1,009	51 %		
	0,718	34 %		
	1,414	103 %		
	0,671	44 %		
	0,799	54 %		
10+2	1,072	55 %	72 %	29 %
	0,975	49 %		
	0,724	35 %		
	1,306	95 %		
	1,296	94 %		
	1,404	103 %		
10+3	0,443	18 %	58 %	28 %

	0,890	44 %		
	0,766	37 %		
	1,150	82 %		
	1,166	84 %		
	1,156	83 %		
10+4	0,954	48 %	69 %	19 %
	0,977	49 %		
	1,118	57 %		
	1,198	86 %		
	1,167	84 %		
	1,208	87 %		
10+5	1,144	59 %	70 %	15 %
	1,078	55 %		
	1,088	56 %		
	1,148	82 %		
	1,218	88 %		
	1,118	80 %		
15+1	1,136	58 %	75 %	20 %
	1,080	55 %		
	1,116	57 %		
	1,278	93 %		
	1,307	95 %		
	1,262	91 %		
15+1,5	1,193	62 %	74 %	18 %
	1,108	57 %		
	1,105	57 %		
	1,162	83 %		
	1,298	94 %		
	1,271	92 %		
15+2	1,135	58 %	72 %	16 %
	1,101	56 %		
	1,091	56 %		
	1,226	88 %		

	1,207	87 %		
	1,176	84 %		
15+3	1,047	53 %	67 %	13 %
	1,089	56 %		
	1,109	57 %		
	1,123	80 %		
	1,141	82 %		
	1,035	73 %		
15+4	0,914	46 %	64 %	18 %
	0,920	46 %		
	0,983	50 %		
	1,149	82 %		
	1,147	82 %		
	1,073	76 %		
15+5	0,905	45 %	55 %	11 %
	0,934	47 %		
	0,890	44 %		
	0,956	67 %		
	0,992	70 %		
	0,848	58 %		
25+1	0,609	28 %	67 %	45 %
	0,576	26 %		
	0,511	22 %		
	1,481	109 %		
	1,506	111 %		
	1,420	104 %		
25+1,5	0,529	23 %	57 %	37 %
	0,526	23 %		
	0,583	27 %		
	1,392	102 %		
	1,215	88 %		
	1,147	82 %		
25+2	0,786	38 %	67 %	35 %

	0,702	33 %		
	0,702	33 %		
	1,345	98 %		
	1,348	98 %		
	1,363	99 %		
25+3	0,700	33 %	63 %	34 %
	0,647	30 %		
	0,720	34 %		
	1,336	97 %		
	1,250	90 %		
	1,303	95 %		
25+4	0,711	34 %	63 %	34 %
	0,737	35 %		
	0,609	28 %		
	1,373	100 %		
	1,229	89 %		
	-			
25+5	0,447	19 %	51 %	34 %
	0,456	19 %		
	0,493	21 %		
	1,187	85 %		
	1,183	85 %		
	1,064	75 %		
35+1	0,620	29 %	60 %	35 %
	0,625	29 %		
	0,558	25 %		
	1,355	99 %		
	1,260	91 %		
	1,182	85 %		
35+1,5	0,486	21 %	50 %	32 %
	0,483	21 %		
	0,501	22 %		
	1,095	78 %		

	1,200	86 %		
	1,030	73 %		
35+2	0,562	25 %	56 %	37 %
	0,548	25 %		
	0,448	19 %		
	1,376	100 %		
	1,108	79 %		
	1,201	86 %		
35+3	0,463	20 %	47 %	29 %
	0,469	20 %		
	0,508	22 %		
	1,104	79 %		
	1,089	77 %		
	0,923	64 %		
35+4	0,526	23 %	48 %	33 %
	0,439	18 %		
	0,349	13 %		
	1,194	86 %		
	1,020	72 %		
	1,053	75 %		
35+5	0,371	14 %	41 %	28 %
	0,398	16 %		
	0,402	16 %		
	0,974	68 %		
	0,938	65 %		
	0,937	65 %		
50+1	0,385	15 %	33 %	21 %
	0,378	15 %		
	0,320	11 %		
	0,781	53 %		
	0,680	45 %		
	0,844	58 %		
50+1,5	0,311	11 %	33 %	26 %

	0,250	7 %		
	0,309	11 %		
	0,823	56 %		
	0,883	61 %		
	0,773	52 %		
50+2	0,432	18 %	36 %	23 %
	0,370	14 %		
	0,335	12 %		
	0,791	54 %		
	0,894	62 %		
	0,824	56 %		
50+3	0,368	14 %	33 %	23 %
	0,286	9 %		
	0,364	14 %		
	0,742	50 %		
	0,782	53 %		
	0,850	58 %		
50+4	0,365	14 %	31 %	24 %
	0,268	8 %		
	0,233	6 %		
	0,759	51 %		
	0,828	57 %		
	0,739	49 %		
50+5	0,331	12 %	34 %	23 %
	0,381	15 %		
	0,353	13 %		
	0,723	48 %		
	0,888	61 %		
	0,800	54 %		

Appendix G

Table 0.37 HCT116 spheroid diameter day 4 after initial seeding in increasing cell densities.

HCT116 day 4	**Parallel 1 um**	**Parallel 2 um**	**Mean**	**SD**
5000	433,41	478,44	455,93	31,84
10000	535,8	529,22	532,51	4,65
15000	630,52	630,52	630,52	0,00
20000	681,1	681,1	681,10	0,00
30000	681,1	607,93	644,52	51,74
50000	647,31	630,52	638,92	11,87

Table 0.38 HCT116 spheroid diameter day 8 after initial seeding in increasing cell densities.

HCT116 day 8	**Parallel 1 um**	**Parallel 2 um**	**Parallel 3 um**	**Parallel 4 um**	**Parallel 5 um**	**Parallel 6 um**	**Mean**	**SD**
5000	490,81	489,25	467,92	457,35	496,15		480,30	16,75
10000	543,67	533,08	564,68	543,63	548,98	529,48	543,92	12,51
15000	561,14	543,63	522,49	559,43			546,67	17,95
20000	550,56	541,68	526,94	527,88			536,77	11,40
30000	574,79	540,61	515,2	574,55	576,28	561,93	557,23	24,64
50000	555,78	576,51	745,21	590,98	547,1	529,28	590,81	78,70

Table 0.39 SW948 spheroid diameter day 4 after initial seeding in increasing cell densities.

SW948 day 4	**Parallel 1 um**	**Parallel 2 um**	**Mean**	**SD**
5000	529,1	613,53	571,32	59,70
10000	658,59	630,52	644,56	19,85
15000	619,16	619,16	619,16	0,00
20000	591,26		591,26	-
30000	681,29	669,82	675,56	8,11
50000	771,16	771,22	771,19	0,04

Table 0.40 SW948 spheroid diameter day 8 after initial seeding in increasing cell densities.

SW948 day 8	Parallel 1 um	Parallel 2 um	Parallel 3 um	Parallel 4 um	Parallel 5 um	Parallel 6 um	Mean	SD
5000	689,94	662,99	663,04	657,61	706,01		675,92	21,04
10000	730,38	659,59	651,24	703,62	692,92	736,83	695,76	35,34
15000	714,77	750,55	660,98	686,63	700,76	781,25	715,82	43,76
20000	737,37	776,82	699,02	620,36	653,02	685,52	695,35	56,44
30000	640,85						640,85	-
50000	742,6	653,94	1081,21	943,94	1142,28	712,85	879,47	205,56

Table 0.41 Caco-2 spheroid diameter day 4 after initial seeding in increasing cell densities.

Caco-2 day 4	Parallel 1 um	Parallel 2 um	Parallel 3 um	Parallel 4 um	Mean	SD
5000	893,78	814,99	819,91	848,77	844,36	36,16
10000	1023,1	1029,83	1022,31	1054,03	1032,32	14,86
15000	1000,5	957,44	1012,84	1029,1	999,97	30,68
20000	1101,93	1011,76	1211,01	999,65	1081,09	97,90
30000	869,19	853	981,08	837,08	885,09	65,32
50000	942,89	991,72	1062,61	1097,35	1023,64	69,50

Table 0.42 Caco-2 spheroid diameter day 8 after initial seeding in increasing cell densities.

Caco-2 day 8	Parallel 1 um	Parallel 2 um	Parallel 3 um	Parallel 4 um	Mean	SD
5000	1713,51	1755,39	1791,12	1664,46	1731,12	54,60
10000	1950,61	1894,28	1651,83	1854,9	1837,91	130,12
15000	1838,1	1851,16	1816,35	1784,57	1822,55	29,10
20000	1928,27	1910,67	1782,88	1892,76	1878,65	65,47
30000	1925,36	1883,18	1918,21	1928,27	1913,76	20,82
50000	2262,15	2270,26	2282,93	2266,67	2270,50	8,92

Appendix H

Table 0.43 HCT116 spheroids 10K seeding density excitation/emission wavelengths of 485/530 nm for Calcein AM staining after various treatments of 5+10 mM of BA+PA and 5-FU.

Treatment	Fluorescence	Normalized to negative control	Replicate mean	SD
BA/PA	8,50E+06	81 %	89 %	12 %
	7,86E+06	75 %		
	1,07E+07	103 %		
	1,07E+07	102 %		
	8,52E+06	81 %		
	9,66E+06	92 %		
0,25 ug/mL 5-FU	8,28E+06	79 %	82 %	7 %
	1,13E+07			
	7,75E+06	74 %		
	8,22E+06	78 %		
	9,63E+06	92 %		
	8,89E+06	85 %		
16,0 ug/mL 5-FU	1,08E+07		85 %	9 %
	8,52E+06	81 %		
	7,79E+06	74 %		
	1,00E+07	96 %		
	1,07E+07			
	9,32E+06	89 %		
BA/PA + 0,25 5-FU	8,44E+06	81 %	82 %	6 %
	7,93E+06	76 %		
	1,22E+07			
	9,30E+06	89 %		
	8,01E+06	77 %		
	9,06E+06	87 %		
BA/PA + 0,5 5-FU	9,03E+06	86 %	84 %	9 %
	8,60E+06	82 %		
	1,01E+07	96 %		

	9,10E+06	87 %		
	7,49E+06	72 %		
	8,76E+06	84 %		
BA/PA + 1,0 5-FU	8,07E+06	77 %	81 %	7 %
	7,98E+06	76 %		
	7,96E+06	76 %		
	1,00E+07	96 %		
	8,43E+06	81 %		
	8,58E+06	82 %		
BA/PA + 4,0 5-FU	8,09E+06	77 %	81 %	9 %
	7,85E+06	75 %		
	1,56E+07			
	7,87E+06	75 %		
	8,73E+06	83 %		
	9,73E+06	93 %		
BA/PA + 16,0 5-FU	1,46E+07		84 %	6 %
	9,13E+06	87 %		
	9,06E+06	87 %		
	8,21E+06	78 %		
	7,89E+06	75 %		
	9,46E+06	90 %		

Table 0.44 HCT116 spheroids 10K seeding density excitation/emission wavelengths of 535/610 nm for PI staining after various treatments of 5+10 mM of BA+PA and 5-FU.

Treatment	Fluorescence	Normalized to negative control	Replicate mean	SD
BA/PA	2,89E+06	93 %	96 %	6 %
	2,95E+06	95 %		
	3,23E+06	104 %		
	3,16E+06	102 %		
	2,87E+06	93 %		
	2,75E+06	89 %		
0,25 ug/mL 5-FU	3,11E+06	100 %	100 %	2 %

	3,15E+06	102 %		
	2,99E+06	97 %		
	3,07E+06	99 %		
	3,04E+06	98 %		
	3,19E+06	103 %		
16,0 ug/mL 5-FU	3,33E+06	108 %	100 %	4 %
	3,08E+06	99 %		
	3,01E+06	97 %		
	3,10E+06	100 %		
	3,01E+06	97 %		
	3,08E+06	99 %		
BA/PA + 0,25 5-FU	3,19E+06	103 %	104 %	3 %
	3,08E+06	99 %		
	3,31E+06	107 %		
	3,25E+06	105 %		
	3,13E+06	101 %		
	3,29E+06	106 %		
BA/PA + 0,5 5-FU	3,24E+06	105 %	101 %	3 %
	3,12E+06	101 %		
	3,11E+06	100 %		
	3,19E+06	103 %		
	2,96E+06	96 %		
	3,19E+06	103 %		
BA/PA + 1,0 5-FU	3,18E+06	103 %	101 %	3 %
	3,05E+06	99 %		
	3,00E+06	97 %		
	3,18E+06	103 %		
	3,12E+06	101 %		
	3,25E+06	105 %		
BA/PA + 4,0 5-FU	3,18E+06	103 %	103 %	2 %
	3,15E+06	102 %		
	3,27E+06	106 %		
	3,05E+06	99 %		

	3,16E+06	102 %		
	3,24E+06	105 %		
BA/PA + 16,0 5-FU	3,42E+06	110 %	102 %	4 %
	3,16E+06	102 %		
	3,11E+06	101 %		
	3,13E+06	101 %		
	3,03E+06	98 %		
	3,13E+06	101 %		

Table 0.45 SW948 spheroids 5K seeding density excitation/emission wavelengths of 485/530 nm for Calcein AM staining after various treatments of 5+10 mM of BA+PA and 5-FU.

Treatment	Fluorescence	Normalized to negative control	Replicate mean	SD
BA/PA	6,17E+06	199 %	123 %	10 %
	3,37E+06	109 %		
	3,05E+06	98 %		
	3,78E+06	122 %		
	3,06E+06	99 %		
	3,43E+06	110 %		
0,25 ug/mL 5-FU	3,03E+06	98 %	99 %	3 %
	3,15E+06	102 %		
	2,95E+06	95 %		
	3,12E+06	101 %		
	3,06E+06	99 %		
	3,17E+06	102 %		
16,0 ug/mL 5-FU	3,11E+06	100 %	100 %	3 %
	3,06E+06	99 %		
	2,98E+06	96 %		
	3,13E+06	101 %		
	3,15E+06	101 %		
	3,19E+06	103 %		
BA/PA + 0,25 5-FU	3,08E+06	99 %	105 %	6 %

	3,16E+06	102 %		
	3,31E+06	107 %		
	3,58E+06	115 %		
	3,10E+06	100 %		
	3,34E+06	107 %		
BA/PA + 0,5 5-FU	3,13E+06	101 %	104 %	3 %
	3,18E+06	102 %		
	3,23E+06	104 %		
	3,15E+06	102 %		
	3,42E+06	110 %		
	3,24E+06	104 %		
BA/PA + 1,0 5-FU	3,09E+06	99 %	100 %	2 %
	3,11E+06	100 %		
	3,03E+06	97 %		
	3,03E+06	98 %		
	3,15E+06	102 %		
	3,14E+06	101 %		
BA/PA + 4,0 5-FU	3,17E+06	102 %	102 %	4 %
	3,08E+06	99 %		
	3,35E+06	108 %		
	3,14E+06	101 %		
	3,08E+06	99 %		
	3,24E+06	104 %		
BA/PA + 16,0 5-FU	3,02E+06	97 %	98 %	3 %
	2,99E+06	96 %		
	2,97E+06	96 %		
	3,03E+06	98 %		
	2,95E+06	95 %		
	3,22E+06	104 %		

Table 0.46 SW948 spheroids 5K seeding density excitation/emission wavelengths of 535/610 nm for PI staining after various treatments of 5+10 mM of BA+PA and 5-FU.

Treatment	Fluorescence	Normalized to negative control	Replicate mean	SD
BA/PA	3,44E+06	94 %	96 %	3 %
	3,45E+06	95 %		
	3,71E+06	102 %		
	3,46E+06	95 %		
	3,52E+06	96 %		
	3,41E+06	94 %		
0,25 ug/mL 5-FU	4,01E+06	110 %	100 %	6 %
	3,47E+06	95 %		
	3,64E+06	100 %		
	3,80E+06	104 %		
	3,56E+06	97 %		
	3,49E+06	96 %		
16,0 ug/mL 5-FU	4,24E+06	116 %	100 %	9 %
	3,24E+06	89 %		
	3,69E+06	101 %		
	3,70E+06	101 %		
	3,43E+06	94 %		
	3,65E+06	100 %		
BA/PA + 0,25 5-FU	3,60E+06	99 %	98 %	3 %
	3,77E+06	103 %		
	3,50E+06	96 %		
	3,60E+06	99 %		
	3,50E+06	96 %		
	3,49E+06	96 %		
BA/PA + 0,5 5-FU	3,49E+06	96 %	94 %	9 %
	3,52E+06	96 %		
	3,38E+06	93 %		
	3,45E+06	95 %		
	3,88E+06	106 %		

	2,87E+06	79 %		
BA/PA + 1,0 5-FU	3,50E+06	96 %	89 %	5 %
	3,34E+06	91 %		
	3,37E+06	92 %		
	3,23E+06	88 %		
	3,06E+06	84 %		
	3,03E+06	83 %		
BA/PA + 4,0 5-FU	3,40E+06	93 %	93 %	2 %
	3,41E+06	93 %		
	3,48E+06	95 %		
	3,42E+06	94 %		
	3,38E+06	93 %		
	3,26E+06	89 %		
BA/PA + 16,0 5-FU	3,47E+06	95 %	94 %	2 %
	3,43E+06	94 %		
	3,46E+06	95 %		
	3,34E+06	92 %		
	3,50E+06	96 %		
	3,37E+06	92 %		

Table 0.47 Caco-2 spheroids 5K seeding density excitation/emission wavelengths of 485/530 nm for Calcein AM staining after various treatments of 5+10 mM of BA+PA and 5-FU.

Treatment	Fluorescence	Normalized to negative control	Replicate mean	SD
BA/PA	1,13E+07	82 %	89 %	12 %
	1,24E+07	90 %		
	1,49E+07	108 %		
	1,31E+07	95 %		
	1,17E+07	85 %		
	1,05E+07	76 %		
0,25 ug/mL 5-FU	1,57E+07	114 %	90 %	15 %
	1,03E+07	75 %		
	1,16E+07	84 %		

	1,43E+07	103 %		
	1,16E+07	84 %		
	1,08E+07	78 %		
16,0 ug/mL 5-FU	1,79E+07	130 %	87 %	5 %
	9,77E+06	71 %		
	1,10E+07	80 %		
	1,16E+07	84 %		
	1,06E+07	77 %		
	1,14E+07	82 %		
BA/PA + 0,25 5-FU	1,37E+07	99 %	97 %	13 %
	1,63E+07	118 %		
	1,24E+07	90 %		
	1,40E+07	101 %		
	1,16E+07	84 %		
	1,20E+07	87 %		
BA/PA + 0,5 5-FU	1,04E+07	75 %	91 %	17 %
	1,48E+07	107 %		
	1,04E+07	76 %		
	1,22E+07	88 %		
	2,29E+07			
	1,53E+07	111 %		
BA/PA + 1,0 5-FU	1,14E+07	83 %	71 %	8 %
	1,07E+07	77 %		
	9,89E+06	72 %		
	9,95E+06	72 %		
	8,75E+06	63 %		
	8,42E+06	61 %		
BA/PA + 4,0 5-FU	1,16E+07	84 %	83 %	8 %
	1,19E+07	86 %		
	1,27E+07	92 %		
	1,16E+07	84 %		
	1,11E+07	80 %		
	9,76E+06	71 %		

BA/PA + 16,0 5-FU	1,08E+07	79 %	79 %	3 %
	1,05E+07	76 %		
	1,10E+07	80 %		
	1,05E+07	76 %		
	1,18E+07	85 %		
	1,06E+07	77 %		

Table: Caco-2 spheroids 5K seeding density excitation/emission wavelengths of 535/610 nm for PI staining after various treatments of 5+10 mM of BA+PA and 5-FU.

Treatment	Fluorescence	Normalized to negative control	Replicate mean	SD
BA/PA	3,44E+06	94 %	96 %	3 %
	3,45E+06	95 %		
	3,71E+06	102 %		
	3,46E+06	95 %		
	3,52E+06	96 %		
	3,41E+06	94 %		
0,25 ug/mL 5-FU	4,01E+06	110 %	100 %	6 %
	3,47E+06	95 %		
	3,64E+06	100 %		
	3,80E+06	104 %		
	3,56E+06	97 %		
	3,49E+06	96 %		
16,0 ug/mL 5-FU	4,24E+06	116 %	100 %	6 %
	3,24E+06	89 %		
	3,69E+06	101 %		
	3,70E+06	101 %		
	3,43E+06	94 %		
	3,65E+06	100 %		
BA/PA + 0,25 5-FU	3,60E+06	99 %	98 %	3 %
	3,77E+06	103 %		
	3,50E+06	96 %		

	3,60E+06	99 %		
	3,50E+06	96 %		
	3,49E+06	96 %		
BA/PA + 0,5 5-FU	3,49E+06	96 %	92 %	8 %
	3,52E+06	96 %		
	3,38E+06	93 %		
	3,45E+06	95 %		
	3,88E+06			
	2,87E+06	79 %		
BA/PA + 1,0 5-FU	3,50E+06	96 %	89 %	5 %
	3,34E+06	91 %		
	3,37E+06	92 %		
	3,23E+06	88 %		
	3,06E+06	84 %		
	3,03E+06	83 %		
BA/PA + 4,0 5-FU	3,40E+06	93 %	93 %	2 %
	3,41E+06	93 %		
	3,48E+06	95 %		
	3,42E+06	94 %		
	3,38E+06	93 %		
	3,26E+06	89 %		
BA/PA + 16,0 5-FU	3,47E+06	95 %	94 %	2 %
	3,43E+06	94 %		
	3,46E+06	95 %		
	3,34E+06	92 %		
	3,50E+06	96 %		
	3,37E+06	92 %		